Improvement of Springback Prediction in Sheet Metal Forming

I.A. Burchitz

This research was carried out under the project number MC1.02121 in the framework of the Strategic Research programme of the Netherlands Institute for Metals Research (www.m2i.nl). The financial support of the NIMR is greatly acknowledged.

Samenstelling van de promotiecommissie:

voorzitter en secretaris:	
Prof. dr. F. Eising	Universiteit Twente
promotor:	
Prof. dr. ir. J. Huétink	Universiteit Twente
assistent promotor:	
Dr. ir. V.T. Meinders	Universiteit Twente
leden:	
Prof. dr. ir. A. de Boer	Universiteit Twente
Prof. dr. ir. D.J. Schipper	Universiteit Twente
Prof. dr. P. Hora	ETH Zurich
Dr. R.M.J. van Damme	Universiteit Twente
Dr. ir. E.H. Atzema	Corus Research, Development & Technology

ISBN 978-90-365-2656-2

1st Printing April 2008

Keywords: springback, adaptive quadrature, shell element, sheet metal forming.

This thesis was prepared with LaTeX by the author and printed by PrintPartners Ipskamp, Enschede, from an electronic document.

IMPROVEMENT OF SPRINGBACK PREDICTION IN SHEET METAL FORMING

PROEFSCHRIFT

ter verkrijging van
de graad van doctor aan de Universiteit Twente,
op gezag van de rector magnificus,
prof. dr. W.H.M. Zijm,
volgens besluit van het College voor Promoties
in het openbaar te verdedigen
op donderdag 22 mei 2008 om 13.15 uur.

door

Igor Alexandrovich Burchitz

geboren op 21 november 1976
te Baranovichi (Belarus)

Dit proefschrift is goedgekeurd door de promotor:

Prof. dr. ir. J. Huétink

en de assistent promotor:

Dr. ir. V.T. Meinders

SUMMARY

Finite element simulation of sheet metal forming is a well-established tool which is used in industrial practice to evaluate geometrical defects caused by elastic springback. Springback can be defined as an elastically-driven change of shape of the deformed part upon removal of external loads. This phenomenon results in a deviation of the real product geometry from that defined in the design phase and can cause significant problems during assembly. To keep the product development time and manufacturing costs low, finite element analysis aims to provide reliable information necessary for the modification of tool and product geometry. Therefore, the accuracy of information obtained in a numerical simulation of springback is essential for the product designers and die makers.

This thesis deals with the improvement of numerical prediction of the springback phenomenon in sheet metal forming. Modelling guidelines and advanced numerical algorithms are presented that better satisfy industrial requirements for an accurate simulation of springback.

Various aspects of a finite element analysis must be carefully considered to prepare an adequate numerical model. An experimental and numerical study was carried out to reach a better understanding of the sensitivity of springback to various physical and numerical parameters. It was demonstrated that a large modelling error can be encountered if an inappropriate material model, contact description, element type and method of unloading is used in the numerical analysis. It was additionally emphasised that the accuracy of springback prediction can be significantly affected by purely numerical factors, such as mass scaling and iterative equation solvers. Artificial adaptations of the model or a low accuracy when solving the global system of equations may lead to an unrealistic change of the part's shape upon unloading.

A finite element solution is influenced by the number of elements used in the numerical model. In simulations of sheet metal forming, using very coarse meshes to describe the blank and tools can reduce the total computation time, but it can also reduce the accuracy of the stress state predicted at the end of the deformation. Recommendations for an appropriate discretisation of the blank and tools have been developed and validated in this thesis. It was demonstrated that the suggested mesh densities minimise the negative effects caused by a poor discretisation and lead to a more

accurate springback prediction.

A simple stretch bending model was used to demonstrate the limitations of the tradition numerical rules used for the through-thickness integration in shell elements. If a sheet material deforms elasto-plastically, these rules require a large number of through-thickness integration points to ensure an accurate springback prediction. To overcome this problem, an adaptive scheme was developed to integrate through the thickness of the shell elements. This scheme uses a limited number of points which can be relocated during the simulation to provide a more accurate prediction of stress resultants at the end of forming. The adaptive scheme relies on several algorithms that: locate the interfaces which separate the elastic and plastic regions of the material; redistribute the integration points such that a point coincides with the elastic-plastic transition; update state variables of the relocated points and perform the actual integration.

The developed adaptive scheme was extended to make it suitable for simulations of realistic deep drawing problems. An advanced algorithm that locates elastic-plastic interfaces was developed. The algorithm is independent of the yield function used in the numerical analysis and can determine the through-thickness location of the elastic-plastic transitions that appear when a material is cyclically bent under tension. Based on this algorithm, a generally applicable adaptive integration scheme was formulated and implemented in the implicit finite element code DiekA. Simulations of several numerical examples were used to evaluate the performance of the advanced adaptive scheme in various deformation regimes. It was demonstrated that the adaptive scheme can guarantee the same level of accuracy of a traditional scheme with a significantly lower number of integration points, hereby decreasing the computation time. Besides, it was shown that the accuracy of adaptive integration does not depend on material properties nor geometrical parameters of a problem.

SAMENVATTING

Eindige-elementensimulaties van plaatvervormingsprocessen zijn een gevestigd gereedschap en worden tegenwoordig gebruikt in industrile problemen voor het evalueren van geometrische afwijkingen door elastische terugvering. Terugvering kan worden gedefinieerd als een elastisch gedreven vormverandering van het onderdeel na het wegnemen van externe belastingen. Dit verschijnsel resulteert in een afwijking van de daadwerkelijke geometrie van het product ten opzichte van de gewenste geometrie. De assemblage van onderdelen kan aanzienlijke problemen geven. Eindige-elementen analyses moeten betrouwbare informatie leveren voor het wijzigen van gereedschap- en productgeometrie, om de kosten en tijd van het productontwikkelingsproces laag te houden. Nauwkeurige informatie over terugvering, verkregen met eindige-elementen simulaties, is daarom essentieel voor productontwerpers en matrijsontwerpers.

Dit proefschrift behelst het verbeteren van de numerieke voorspelling van het terugveringsverschijnsel in plaatvervormingsprocessen. Ontwerpregels en geavanceerde numerieke algoritmen worden gepresenteerd die beter voorzien in de industrile behoefte voor een nauwkeurige simulatie van terugvering.

De verschillende aspecten van de eindige-elementen analyse moeten zorgvuldig worden overwogen voor het opzetten van een numeriek model. Een experimenteel en numeriek onderzoek is uitgevoerd om een beter inzicht te verkrijgen in de gevoeligheid voor terugvering met betrekking tot verscheidene fysische en numerieke parameters. Aangetoond is dat met het numerieke model grote modelleerfouten kunnen optreden als een ongeschikt materiaal model, contact beschrijving, element type en methode voor het wegnemen van de belasting wordt gebruikt in de analyse. Verder wordt aangetoond dat de nauwkeurigheid van de voorspelling van de terugvering aanzienlijk kan worden beïnvloed door puur numerieke factoren, bijvoorbeeld massa compensatie of iteratieve vergelijkingsoplossers. Kunstmatige aanpassingen aan het model, of een lage behaalde nauwkeurigheid bij het oplossen van de globale systeemvergelijkingen, kan resulteren in een onrealistische verandering van de productgeometrie na het wegnemen van de belastingen.

Een eindige-elementen simulatie is afhankelijk van het aantal elementen in het numerieke model. In simulaties van plaatvervormingsprocessen kan het gebruiken van een grof elementengrid voor de beschrijving van plaat en gereedschappen de

rekentijd verkorten, maar zal de nauwkeurigheid van de voorspelde spanningstoestand aan het einde van het vervormingsproces afnemen. Aanbevelingen voor een adequate discretisatie van de plaat en de gereedschappen zijn ontwikkeld en gevalideerd in dit proefschrift. Aangetoond is dat de aanbevolen element dichtheden de negatieve effecten van slechte discretisatie minimaliseren en daarmee leiden tot een nauwkeurigere voorspelling van de terugvering.

Een simpel rek- buigingsmodel is gebruikt om de beperkingen van traditionele 'door-de-dikte' integratieschema's van schaal elementen aan te tonen. Als een plaat materiaal elastisch-plastisch vervormt, dan gebruiken deze integratieschema's een groot aantal integratiepunten voor een accurate voorspelling van de terugvering. Om dit probleem te vermijden is een adaptief integratieschema ontwikkeld voor schaal elementen. Dit schema gebruikt een beperkt aantal integratiepunten, welke kunnen worden herplaatst gedurende de simulatie, om een betere voorspelling van de resterende spanningen na het vormgevingsproces te krijgen. Het adaptieve schema bestaat uit verscheidene algoritmen: het lokaliseren van de interface tussen de elastische en plastische regionen van het materiaal; opnieuw distribueren van de integratiepunten zodat een punt samenvalt met een elastisch-plastisch overgang; het aanpassen van de toestandsvariabelen van de opnieuw gedistribueerde punten en uitvoering van de daadwerkelijke integratie.

Het ontwikkelde adaptieve schema is uitgebreid om het toepasbaar te maken voor gebruik in simulaties van realistische dieptrek problemen. Een geavanceerd algoritme voor de lokalisering van de elastisch-plastische overgang is ontwikkeld. Het algoritme is onafhankelijk van het gebruikte vloeioppervlak en het kan de elastisch-plastische overgangen over de dikte bepalen wanneer het materiaal cyclisch wordt gebogen onder trekspanning. Op basis van dit algoritme is een adaptief integratieschema geformuleerd en gemplementeerd in het impliciete eindige-elementen programma DiekA. Simulaties van verscheidene numerieke voorbeelden zijn gebruikt om de prestaties van het geavanceerde adaptieve schema te evalueren in meerdere deformatieregimes. Het is aangetoond dat doordat minder integratiepunten nodig zijn, het adaptieve schema de rekentijd aanzienlijk terugbrengt. De nauwkeurigheid wordt niet benvloed door verandering van de simulatieparameters.

CONTENTS

CHAPTER

ONE

INTRODUCTION

1.1 Geometrical defects in sheet metal forming

A large variety of metallic parts of automobiles, aircrafts, building products and domestic appliances are produced by deformation processing. This comprises manufacturing methods that are used to create the primary shape of products by plastically deforming the material. Well-known examples are forging, rolling, extrusion, sheet metal forming and hydroforming [1, 2]. Sheet metal forming is a special class of deformation processes in which blanks, with the thickness being much smaller than the other dimensions, are formed into the desired shape. Sheet metal forming involves bending, flanging, stretching, punching, deep drawing and some other processes.

The deep drawing process allows the production of large quantities of sheet metal parts of various complexity. An exploded view of a typical set-up for the deep drawing process is illustrated in Figure 1.1. During the process a piece of sheet metal is clamped between the die and the blankholder. A force is applied to the blankholder to prevent wrinkling of the sheet and to control the material flow during the deformation. When the punch is pushed into the die cavity the sheet deforms plastically and thereby it takes the specific shape of the tools. An example of such a deep drawing part is given in Figure 1.2(a).

The quality of the final product shape is determined by the tools design, process parameters, shape and material of the blank. It is important to carefully consider all these factors prior to manufacturing, otherwise a defective product could result. Typical defects which are observed in sheet metal forming practice are wrinkling, necking and subsequent fracture, drawing grooves and orange peel [2, 3]. In addition to these defects, there is also always geometrical distortion caused by elastic springback. Right after forming, the shape of the deformed product closely conforms to the geometry of tools. However, as soon as the tools are retracted, an elastically-driven

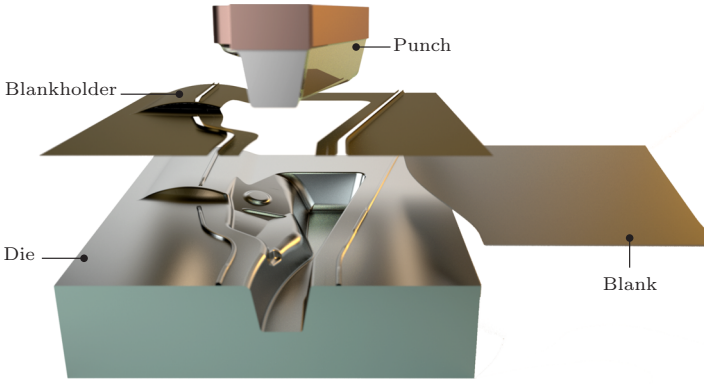

Figure 1.1: Exploded view of the set-up for deep drawing of an automotive part.

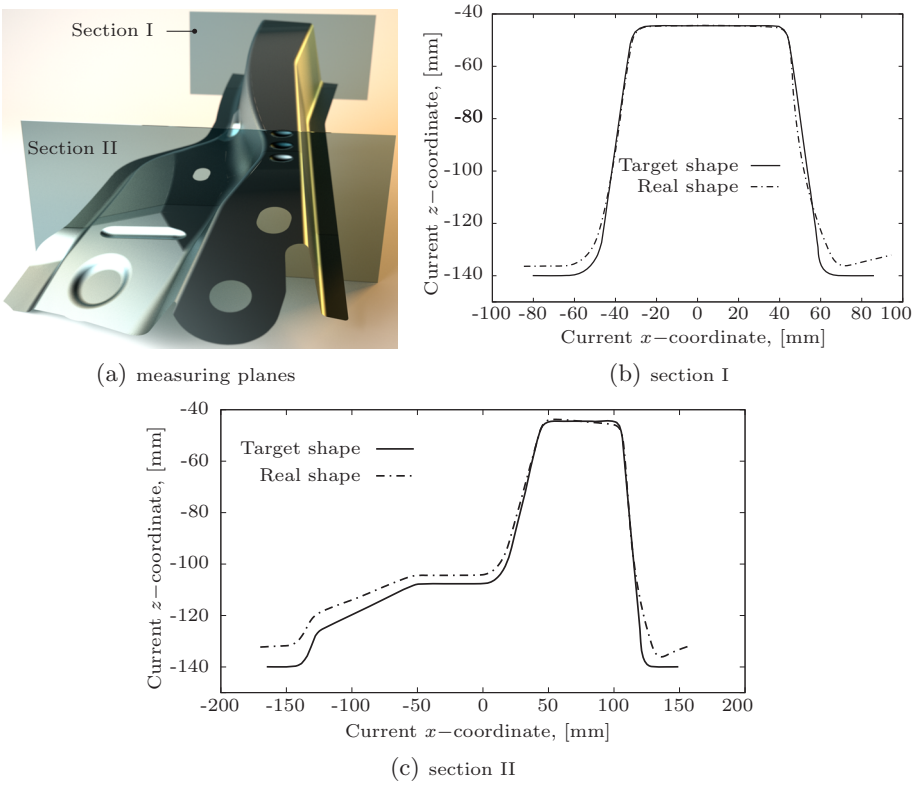

(a) measuring planes

(b) section I

(c) section II

Figure 1.2: Automotive underbody cross member. Shape deviation due to springback.

change of the product shape takes place. The significance of this is illustrated in Figures 1.2(b) and 1.2(c) where the geometry of the automotive part in two

cross-sections is shown. Profiles, measured using optical scanning equipment [4], are compared to the CAD data. As can be seen, springback causes a considerable deviation of the product geometry from the design specification and will be the major cause of assembly problems. Nowadays springback raises even higher concerns in the automotive industry due to the current trends of using sheets made of aluminium alloys and high strength steels. Due to their mechanical properties products made of these materials exhibit higher geometrical distortions upon unloading.

The industry relies on two groups of techniques to control the springback, namely mechanics-based reduction and geometry-based compensation [5]. Methods from the first group are based on the understanding of the mechanics of sheet metal forming. For example, blankholder force control is a commonly used technique. This is based on choosing the appropriate blankholder force trajectory which reduces the amount of springback by increasing the tension in the material [6–9]. Another method to reduce the springback is to form a product in multiple steps using several sets of tools or only one set with some additional mechanisms. Typical methods that are based on this type of operations are redrawing or forming with reconfigurable tooling [10].

The second group - the geometry-based compensation - can guarantee the shape accuracy of the formed product by performing the appropriate modifications of the tools [11]. The basis for these modifications are the measurements of the part after real forming or the results of computer simulations. Various methods for measuring shape deviations are available in the industry, e.g. checking fixture-based method or on-die springback measurements [5]. These techniques provide reliable data for the springback compensation but can be very time-consuming and cost-prohibitive, especially when applied to complex parts made of high strength steels or aluminium alloys. These drawbacks can be overcome by using computer simulations in the tool design phase, provided that the numerical analysis ensures accurate springback prediction.

1.2 Numerical simulations in the design process

To manufacture a sheet metal part with the desired shape and performance, an extensive knowledge about the influence of various parameters is needed. In order to

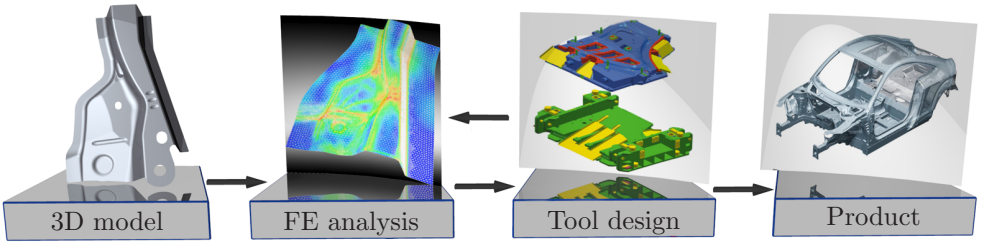

Figure 1.3: Design process schematic.

establish this knowledge base, experimental try-outs and numerical simulations are used. Computer simulation, based on the finite element (FE) method, is a powerful tool that gives the possibility to observe effects of changing any process parameter prior to the actual tool manufacturing [12, 13].

To illustrate the actual role of computer simulations, a typical process chain for the manufacture of an automotive part is considered. To reduce the production costs, minimise the development time and improve the product quality, FE simulations are performed at different stages of the process chain [14–16]. During the conceptual development, simulations are used to evaluate feasibility of manufacturing of the designed part and to define required modifications of the concept. More elaborate and accurate simulations are performed during the tool design and manufacturing phase to determine the number of stamping steps and the optimal process parameters. These calculations are also used for the springback prediction and compensation to define the actual tool geometry. Finally, numerical analysis is also employed during the tool tryout and the actual production, in order to eliminate any remaining forming defects [12].

Despite significant developments in the field of FE simulation of sheet metal forming processes, currently the accuracy of springback prediction does not yet satisfy industrial needs [16–19]. There remains a need to use expensive and time-consuming experimental try-outs to determine the proper tool geometry and all other parameters which can lead to the desired product shape. The low accuracy of springback prediction is attributed to the lack of understanding of this phenomenon and to the use of oversimplified models that describe, for example, the material behaviour or contact conditions during the deformation. Therefore, research in this field is necessary that can improve the usability of numerical simulations in industrial sheet metal forming. Accurate prediction and control of springback will allow tool designers to numerically evaluate the possibility of obtaining the specified product shape and to perform necessary modifications based on this information only (Figure 1.3). A reliable numerical procedure can eliminate the need for experimental try-outs, and hence drastically reduce the lead time and manufacturing costs.

1.3 Objective and outline of this thesis

The main objective of the research presented in this thesis is to develop and improve numerical algorithms and modelling guidelines that will allow the industry to meet its requirements in the accuracy of springback prediction in sheet metal forming.

The general outline of the thesis is as follows. Chapter 2 summarises major findings in the literature and describes some results of numerical and experimental work conducted to obtain a better understanding of the springback phenomenon. Important subjects of FE modelling and their influence on the accuracy of springback prediction are discussed. To show basic dependencies between the amount of springback and material properties or process parameters, a simple analytical model for stretch bending is developed. Also, guidelines for decreasing the modelling error in an FE analysis of springback are defined.

The discretisation error is the main subject of Chapter 3. FE simulations with shell elements are used to show the negative influence of poor blank and tool discretisation on the accuracy of springback prediction. Guidelines for choosing an appropriate element size while meshing the blank and tools are given.

Additional methods for decreasing the error due to the spatial discretisation are discussed in Chapter 4. In this chapter, reasons behind the error of springback prediction resulting from using standard through-thickness integration schemes for shell elements are investigated. An efficient strategy for adaptive through-thickness integration is presented and its potential is shown using academic test problems. In Chapter 5 the scheme is further extended with an algorithm that can trace the location of stress profile kinks in realistic loading conditions. Several academic tests and a benchmark problem are used to evaluate the performance of a generally applicable adaptive scheme and to demonstrate the advantages of adaptive integration in FE analysis of springback in sheet metal forming.

Conclusions and recommendations of this thesis are summarised in Chapter 6.

CHAPTER

TWO

SPRINGBACK IN SHEET METAL FORMING

Springback can be defined as an elastically-driven change of shape of a deformed product which takes place during removal of external loads. It is a complex physical phenomenon which is mainly governed by the stress state obtained at the end of a deformation. Depending on the product geometry and deformation regime, there are several types of springback in sheet metal forming: bending, membrane, twisting and combined bending and membrane[5]. Pure bending springback can be observed after bending a material in plane strain. Membrane springback takes place during the unloading of a material from in-plane tension or compression. The twisting type of springback can be observed while forming components with large differences in sectional dimensions, such as for example shallow panels [20]. This type of springback is the result of uneven elastic recovery in different directions. The combined bending and membrane springback is the type which is most commonly observed in industrial practice. The product geometry is usually so complex that the material is bent out-of-plane and simultaneously stretched or compressed in-plane.

Accurate modelling of springback in sheet metal forming requires that this phenomenon is well understood. Simple experimental procedures can be used to study the sensitivity of springback to various process parameters, for example flanging [21] or unconstrained cylindrical bending [22]. More complex tests have been developed to obtain a better understanding of material behaviour in realistic deformation regimes [23, 24]. Recent experimental investigations have shown that the springback phenomenon in sheet metals also involves small scale plasticity effects and is thus not fully elastic [25, 26].

Several methods are available for the prediction of springback. Analytical solutions that describe the change of product geometry after simple forming operations were developed, see for example in [27–29]. Although not generally applicable, these models are powerful tools that can be used to quickly visualise dependencies between some material and process parameters and the amount of springback. Springback analysis of complex industrial products is usually performed using the finite element (FE)

method. When using FE models it is important to remember that the accuracy of springback prediction is determined by factors that are responsible for the quality of simulation of the forming step. In past decades, various assumptions were introduced to make a simulation of forming more efficient. In some cases, these assumptions may be contrary to reality and applicability of most of them to the simulation of springback should be reanalysed [17, 30–32].

A short overview of the experimental procedures that are used to study the springback phenomenon in sheet metals is given in Section 2.1. A simple analytical model that describes bending of a beam under tension and allows calculating stress resultants and the change of shape during unloading is given in Section 2.2. This model is used to show the influence of some physical and numerical parameters on the amount of springback. Various modelling aspects that have a significant effect on the accuracy of springback prediction are discussed in Section 2.3. Guidelines for the accurate prediction of springback in sheet metal forming using FE analysis conclude this chapter.

2.1 Experimental procedures to characterise springback

In recent years, various experimental techniques have been developed to study and characterise springback in sheet metals. The most popular and commonly used procedures are cylindrical bending [22], U-bending [33, 34], V-bending [34–36] (see Figure 2.1) and flanging [21, 37]. These methods are attractive because the level of springback is large and can easily be measured. Sensitivity of springback to basic parameters, such as the tool radius to sheet thickness (R/t) ratio, mechanical properties of sheet material and contact parameters is usually studied. The major drawback of these experiments is that they cannot imitate realistic process conditions during sheet metal forming.

Stretch bending tests are used to study the importance of tension in minimising and controlling springback [38]. A typical test scheme is shown in Figure 2.2. A metallic strip is fixed between the tools and is deformed by displacing the semi-cylindrical

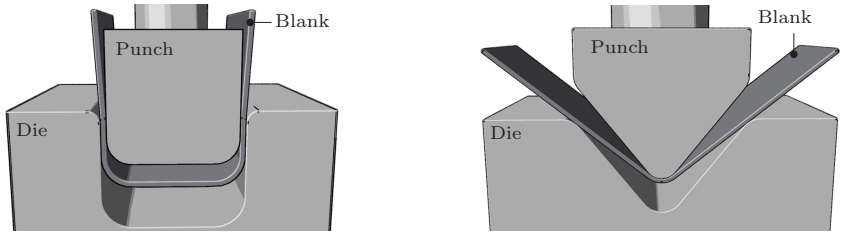

(a) U-bending (b) V-bending

Figure 2.1: Commonly used experimental techniques for studying the springback in sheet metals.

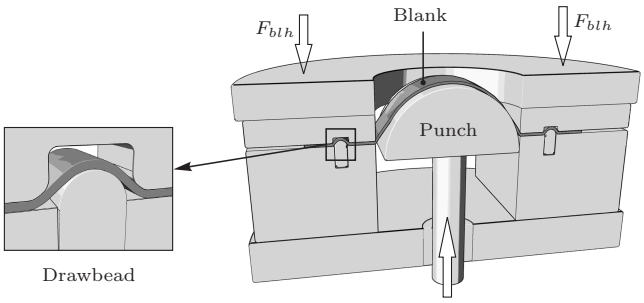

Figure 2.2: Stretch bending test (Kuwabara et al. [38]).

punch through a certain distance. As shown in this figure, drawbeads are employed to restrain the material flow. A drawbead can be considered as the local control mechanism that sufficiently restrains the material flow at relatively low blankholder force [3]. The restraining force is created by cyclic bending and unbending the material when it travels through the drawbead. This type of test can be used to show the effect of in-plane tension on the amount of springback.

A simple bending-reverse bending experimental method was proposed by Gau and Kinzel [39, 40]. As illustrated in Figure 2.3, the experimental procedure consists of several steps: bending, turning the sheet specimen and bending in the opposite direction, turning the specimen again and bending it in the original direction, and so on. Angle after springback is determined by the coordinate measuring machine and the dependence of this angle on the deformation history can then easily be observed.

The draw bending test (see Figure 2.4), presented as a benchmark problem at the NUMISHEET 1993 conference, is often used to assess springback in sheet metals under more realistic forming conditions. During forming, the blank material experiences stretching, bending and unbending deformations when it passes the tool radius. This deformation path creates a complex stress state which is responsible for the formation

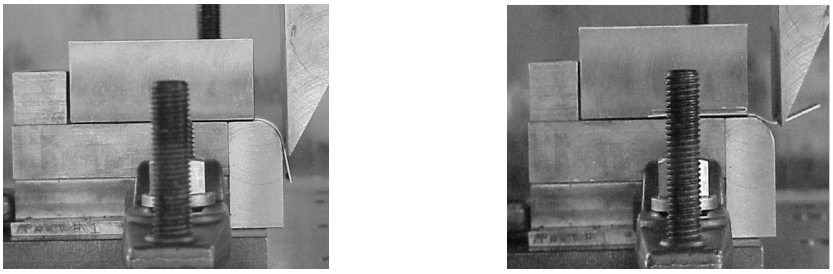

(a) bending (b) reverse bending

Figure 2.3: Some steps of deformation sequence of bending, reverse bending test (Gau and Kinzel [39]).

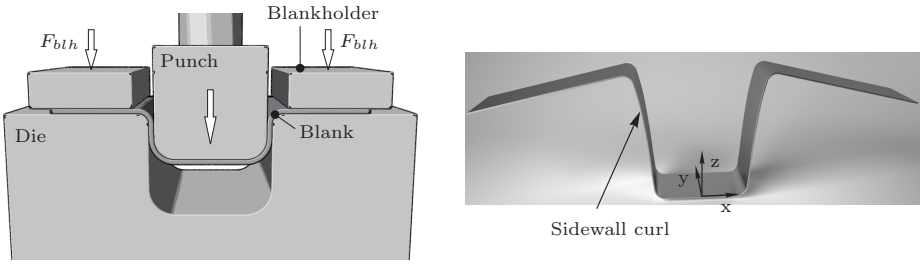

(a) set-up schematic (b) blank after springback, mild steel

Figure 2.4: Top-hat section test - NUMISHEET'93 benchmark.

of so-called sidewall curl (see Figure 2.4(b)). Various authors used this experimental set-up in their studies and it has been shown that the sidewall curl becomes more pronounced for small tool radii and smaller clearances between the tools [6, 28, 41, 42].

The major drawback of the draw bending test is the lack of control or direct measurement of sheet tension, which makes this experimental procedure less suitable for verifying the results of simulations [17, 24, 43, 44]. Carden et al. suggested an alternative experimental procedure that can be used to study springback in sheet metals in realistic forming conditions [24]. The draw/bend test is schematically shown in Figure 2.5. The experimental set-up consists of upper and lower actuators oriented at 90° to one another. Placed at the intersection of their action lines there is a cylinder which represents the tooling radius. The upper actuator provides a constant restraining force, while the lower actuator is used to displace the blank at a constant speed. When drawn over the tool radius, the blank undergoes tensile loading, bending

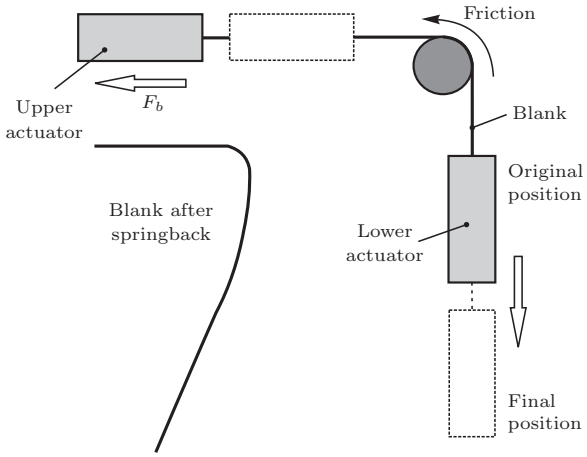

Figure 2.5: Draw/bend test (Carden et al. [24]).

and unbending. The test is considered as a well-characterised example of a forming operation that emulates real process conditions and has the advantage of simplicity [17]. This test was also used to show experimentally the time-dependent springback of aluminium alloys [24, 45].

The amount of springback during unloading depends on the Young's modulus of the material. In analysis of sheet metal forming it is common practice to assume that the elastic modulus remains constant. However, experimental investigations revealed that elastic constants of a material may change during the plastic deformation. Decrease of the elastic constants with increasing plastic strain was shown experimentally for the first time by Lems [46]. Tensile tests were used to study the change of Young's modulus of gold, copper and silver. The fact that workhardening of steels and aluminium alloys can cause an appreciable decrease of the elastic modulus was experimentally proved by several authors [25, 47–51]. In the experiments, tensile-compression tests were used and the Young's modulus was measured either from the stress-strain relation obtained by employing a precision extensometer or dynamically, based on the specimen's natural frequencies. It was shown that both for steels and aluminium alloys the Young's modulus can decrease with plastic straining by up to 20% of its initial value. Additionally, it was also shown experimentally that the elastic modulus recovers to its initial value with time [46, 47]. Movable dislocations and their pile-up due to the plastic deformations are considered to be the major cause of the decrease of Young's modulus. During the plastic deformation, released dislocations move along slip surfaces and easily pile up when stopped by solutes, grain boundaries or some other obstacles. These movable pile-up dislocations can move backward when the shearing stress is released during unloading, leading to a small amount of non-elastic deformations. Therefore, as shown in Figure 2.6, the reduction of the elastic modulus can be seen as an extra nonlinear component of the total springback strain which is strongly dependent upon the deformation path and the crystallographic texture evolution [25, 26, 45, 52].

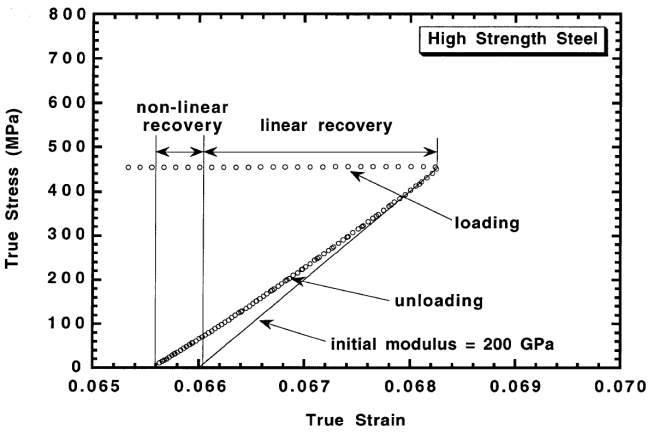

Figure 2.6: Nonlinear effects during unloading (Cleveland and Gosh [25]).

2.2 Analytical prediction of springback in stretch bending

In sheet metal forming, analytical solutions for springback were first derived for simple two-dimensional cases, such as plane strain bending, stretch bending, drawing and plane strain cyclic bending [28, 53–55]. Later, methods for the theoretical prediction of springback after realistic forming operations were developed, e.g. flanging [21, 37, 56], V-bending [27, 57], double-curvature forming [29, 58–60] and U-bending [61]. Special attention was given to the accurate analytical prediction of the sidewall curl caused by bending and unbending deformation at the die shoulder.

In this section the mechanics of plane strain bending in combination with tension of an elastic-plastic sheet material is considered. An analytical model for arbitrary isotropic hardening is developed, which can be used to predict tensile forces, bending moments and springback.

2.2.1 Plane strain bending

Bending a sheet material along a straight line is considered. It is assumed that a plane strain condition exists in the plane perpendicular to the bending line and that cross-sections remain plane and normal to the mid-surface after the deformation (Kirchhoff hypothesis). A two-dimensional representation of the considered problem is shown in Figure 2.7. During bending, a radial direction ρ and a circumferential

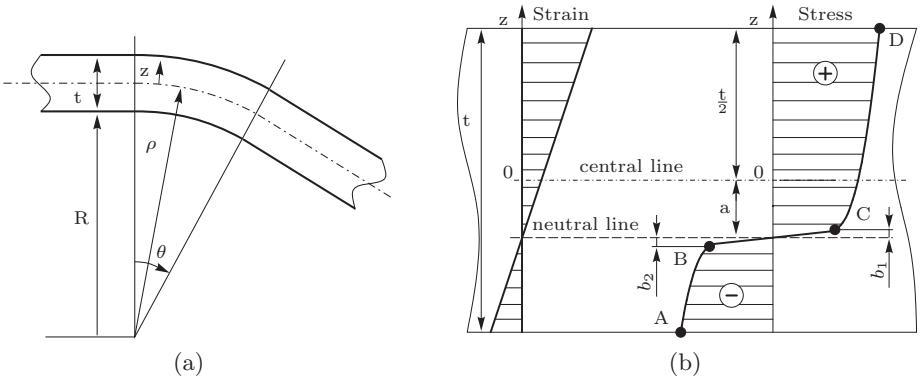

Figure 2.7: Plane strain bending: a) definition of parameters; b) typical strain and stress profiles which occur during the deformation.

direction θ can be distinguished. Because of the Kirchhoff hypothesis these directions are the principal strain directions. For planar isotropic materials, it also means that these directions are the principal stress directions. Note that the mid-surface is not necessarily the neutral surface. If a tensile force is present during bending, the neutral line shifts towards the centre of curvature. Figure 2.7(b) shows stress and strain

distributions in a cross-section of the material after bending to a radius under tension. These quantities are defined below.

2.2.2 Strains and stresses

A line segment of initial length l_0, situated at a distance z above the mid-surface, after bending to an angle θ with a radius of curvature ρ will deform to a length l. The radius of curvature is defined as $\rho = R + t/2$ where t is the material thickness. The segment's length l can be expressed as a function of the length of the fibre at the mid-plane $l_\mathrm{m} = \rho\theta$, the radius of curvature and the distance z:

$$l = (\rho + z)\,\theta = l_\mathrm{m}\left(1 + \frac{z}{\rho}\right) \tag{2.1}$$

The circumferential true strain is given by:

$$\varepsilon_\theta = \ln(l/l_0) = \ln\left[\frac{l_\mathrm{m}}{l_0}\left(1 + \frac{z}{\rho}\right)\right] \tag{2.2}$$

This can be split in the true strain in the mid-plane:

$$\varepsilon_\mathrm{m} = \ln(l_\mathrm{m}/l_0) \tag{2.3}$$

and an additional bending true strain:

$$\varepsilon_\mathrm{b} = \ln\left(1 + \frac{z}{\rho}\right) \tag{2.4}$$

In the case of large R, the difference between the true strain and the engineering strain is negligible, however, the engineering strain is easier to handle. The membrane and bending engineering strains can be written as follows:

$$\varepsilon_\mathrm{m} = \Delta l_\mathrm{m}/l_0 \tag{2.5}$$

$$\varepsilon_\mathrm{b} = \frac{z}{\rho} \tag{2.6}$$

From the assumption of linear distribution of strains through the sheet thickness, the membrane strain has a value equal to:

$$\varepsilon_\mathrm{m} = \frac{a}{\rho} \tag{2.7}$$

where variable a defines the position of the neutral line. The total engineering circumferential strain becomes:

$$\varepsilon_\theta = \frac{z + a}{\rho} \tag{2.8}$$

The material behaviour in this model is restricted to isotropic. In a plane strain situation, in the case of the von Mises yield condition the main principal stress can be found from [53]:

$$\sigma_\theta = \frac{2}{\sqrt{3}}\sigma_\mathrm{f} = S \tag{2.9}$$

where σ_f is the uniaxial flow stress and S is the plane strain flow stress.

2.2.3 Constitutive relations

In general, a material will show elastic-plastic strain-hardening behaviour. In the elastic range the stress in the circumferential direction is found from Hooke's law for plane strain:

$$\sigma_\theta = \frac{E}{1-\nu^2}\,\varepsilon_\theta = E'\varepsilon_\theta \tag{2.10}$$

where E is the Young's modulus and ν is Poisson's ratio. The plastic strain-hardening behaviour is approximated by a power law (Nadai hardening):

$$\sigma_\theta = C'\left(\varepsilon_0 + \varepsilon_\theta^p\right)^n \tag{2.11}$$

with C' and n hardening parameters and ε_0 being a pre-strain which can be calculated from the following condition:

$$\sigma_{\mathrm{f}(0)} = C\varepsilon_0^n \tag{2.12}$$

where $\sigma_{\mathrm{f}(0)}$ is the initial uniaxial yield stress and C is the material strength coefficient in the uniaxial case. The relation between the plane strain and uniaxial value of this parameter can be approximated by:

$$C' \approx C\left(\frac{2}{\sqrt{3}}\right)^{n+1} \tag{2.13}$$

2.2.4 Loading - stress resultants

Equations that define stress resultants acting on the strip during the deformation are derived next. Let b_1 and b_2 be variables that determine the position of yield points in regions where the material is in tension or compression (see Figure 2.7(b)). These variables are defined relative to the neutral line which is situated at $z = -a$. The coordinates of the yield points are:

$$\begin{aligned} z_1 &= -a + b_1 \\ z_2 &= -a - b_2 \end{aligned} \tag{2.14}$$

Combining Equations (2.14) and (2.8) gives the yield strains in the tension and compression regions:

tension region

$$\varepsilon_\theta^y = \frac{z_1 + a}{\rho} = \frac{b_1}{\rho} \tag{2.15}$$

compression region

$$\varepsilon_\theta^y = \frac{z_2 + a}{\rho} = -\frac{b_2}{\rho} \tag{2.16}$$

The variables b_1 and b_2 define the boundaries of the elastic region and can be found by using Hooke's law:

$$b_1 = b_2 = \rho\varepsilon_\theta^y = \frac{\rho}{E'}S_0 \tag{2.17}$$

where E' is defined by Equation (2.10) and S_0 is the initial plane strain flow stress, Equation (2.9).

The total circumferential strain in the region of plastic deformations can be defined as the sum of two parts - the constant strain at yield and the strain due to the material workhardening:

$$\varepsilon_\theta = \varepsilon_\theta^y + \varepsilon_\theta^{wh} \tag{2.18}$$

Rewriting the above equation, the strain due to the material workhardening can be derived:

tension region

$$\varepsilon_\theta^{wh} = \varepsilon_\theta - \varepsilon_\theta^y = \frac{z+a}{\rho} - \frac{S_0}{E'} \tag{2.19}$$

compression region

$$\varepsilon_\theta^{wh} = \varepsilon_\theta - \varepsilon_\theta^y = \frac{z+a}{\rho} + \frac{S_0}{E'} \tag{2.20}$$

The circumferential stress in the plastic deformation region is determined by Equation (2.11). In order to calculate the stress, the plastic strain must be known. However, since the power law represents a non-linear hardening behaviour, the plastic strain is not known beforehand. Therefore an approximation is made by equating the plastic strain to the strain due to workhardening. The plastic strain $\varepsilon_\theta^p = \varepsilon_\theta - \varepsilon_\theta^e$ is smaller than the strain due to workhardening $\varepsilon_\theta^{wh} = \varepsilon_\theta - \varepsilon_\theta^y$ and, thus the circumferential stress is overestimated. Note that this overestimation rapidly decreases for small strains or a low C' value. As a result, the circumferential stress in the plastic part of the material can be written as:

tension region

$$\sigma_\theta^p = C'\Big(\varepsilon_0 + \frac{z+a}{\rho} - \frac{S_0}{E'}\Big)^n \tag{2.21}$$

compression region

$$\sigma_\theta^p = -C'\Big(\varepsilon_0 + \Big|\frac{z+a}{\rho} + \frac{S_0}{E'}\Big|\Big)^n \tag{2.22}$$

The plastic strain is negative in the compression region, therefore its absolute value is used in the power law to calculate the circumferential stress. The forces and bending moments acting on the sheet per unit length can then be found from:

$$T = \int_{-t/2}^{t/2} \sigma_\theta \, dz \tag{2.23}$$

$$M = \int_{-t/2}^{t/2} \sigma_\theta \, z \, dz \tag{2.24}$$

The tensile force can be split into three components:

$$T = T^e + T_T^p + T_C^p \tag{2.25}$$

In this equation T^e is the force caused by the elastic stresses, T_T^p and T_C^p are the tensile and the compressive forces caused by the plastic stresses. The contribution of the elastic and the plastic stresses to the total tension will be:

$$T^e = \int_{z_2}^{z_1} E' \frac{z+a}{\rho}\, dz \tag{2.26}$$

$$T_T^p = \int_{z_1}^{t/2} C' \Big(\varepsilon_0 + \frac{z+a}{\rho} - \frac{S_0}{E'}\Big)^n\, dz \tag{2.27}$$

$$T_C^p = -\int_{-t/2}^{z_2} C' \Big(\varepsilon_0 + \Big|\frac{z+a}{\rho} + \frac{S_0}{E'}\Big|\Big)^n\, dz \tag{2.28}$$

The total moment per unit width acting about the mid-plane can be described as a sum of three components:

$$M = M^e + M_T^p + M_C^p \tag{2.29}$$

where M^e is the elastic part, M_T^p and M_C^p are the plastic parts of the total bending moment in the region of tension and compression. These components can be found as follows:

$$M^e = \int_{z_2}^{z_1} E' \frac{z+a}{\rho}\, z\, dz \tag{2.30}$$

$$M_T^p = \int_{z_1}^{t/2} C' \Big(\varepsilon_0 + \frac{z+a}{\rho} - \frac{S_0}{E'}\Big)^n\, z\, dz \tag{2.31}$$

$$M_C^p = -\int_{-t/2}^{z_2} C' \Big(\varepsilon_0 + \Big|\frac{z+a}{\rho} + \frac{S_0}{E'}\Big|\Big)^n\, z\, dz \tag{2.32}$$

The full derivation of the equations of stress resultants can be found in Appendix B.

2.2.5 Unloading - springback

After bending the sheet to the radius R a moment M remains. If external loads are removed, this bending moment is released and the sheet will spring back to a different shape to reach a new equilibrium. The magnitude of the stresses will decrease and the amount of shape change (i.e. change in curvature) can be related to the applied bending moment. The change in internal stresses due to elastic unloading reads:

$$\begin{aligned} \Delta\sigma_\theta &= E' \Delta\varepsilon_\theta, \quad \text{with} \\ \Delta\varepsilon_\theta &= \frac{z}{\rho} - \frac{z}{\rho'} = \Delta\Big(\frac{1}{\rho}\Big)\, z \end{aligned} \tag{2.33}$$

where ρ' is the radius of curvature after unloading. The change in internal stresses causes a change in bending moment, ΔM:

$$\Delta M = \int_{-t/2}^{t/2} \Delta\sigma_\theta\, z\, dz = \int_{-t/2}^{t/2} E' \Delta\Big(\frac{1}{\rho}\Big)\, z^2\, dz \quad \Rightarrow$$

$$\Delta M = \frac{E' t^3}{12} \Delta\left(\frac{1}{\rho}\right) = \frac{t^3}{12} \frac{\Delta\sigma_\theta}{z} \tag{2.34}$$

The removal of external loads results in $\Delta M = -M$. Thus the change in curvature is related to the applied bending moment via:

$$\frac{E' t^3}{12} \Delta\left(\frac{1}{\rho}\right) = -M$$

$$\Delta\left(\frac{1}{\rho}\right) = -\frac{12M}{E' t^3} \tag{2.35}$$

The change in curvature leads to a change in bending angle. It can be determined from the arc length l of the bend which remains constant after bending and during unloading, hence:

$$l = \theta\rho \Rightarrow \theta = l\frac{1}{\rho} \tag{2.36}$$

An expression for the change in angle $\Delta\theta$ can be obtained by differentiation of the above equation to the curvature:

$$\frac{d\theta}{d\left(\frac{1}{\rho}\right)} = l = \rho\,\theta \Rightarrow d\theta = d\left(\frac{1}{\rho}\right)\rho\,\theta \tag{2.37}$$

$\Delta\theta$ can then be calculated from:

$$\Delta\theta = \Delta\left(\frac{1}{\rho}\right)\rho\,\theta = -\frac{12M}{E' t^3}\,\rho\,\theta \tag{2.38}$$

The latter equation defines basic relations between material and process parameters and the amount of springback. For example, it can be seen that the springback is proportional to the bending angle θ and to the ρ/t ratio. Additionally, since the bending moment M is defined as a function of the initial uniaxial yield stress $\sigma_{f(0)}$, the springback is proportional to the $\sigma_{f(0)}/E$ ratio. Equation (2.38) shows that application of aluminium alloys and high strength steels in manufacturing of sheet metal parts leads to larger shape deviations due to the increased springback. For aluminium sheets the springback is higher due to a smaller Young's modulus. Application of high strength steels increases the elastic springback because of the higher initial yield stress and thinner sheets which are typically used in production.

2.2.6 Influence of in-plane tension on springback

Influence of tension on the amount of springback is shown by considering a particular example. An aluminium sheet is bent to a given radius and stretched. The sheet thickness is 1.0mm and the radius of bending is 5.0 mm. The material Young's modulus is 70.6 GPa, Poisson's ratio is 0.341, initial yield stress in uniaxial tension is 125.02 MPa and the hardening parameters are C=561.34 MPa and n=0.321. As the tension increases, the bending moment M is calculated until the neutral line coincides with the lower surface of the sheet. The relation between the bending moment and

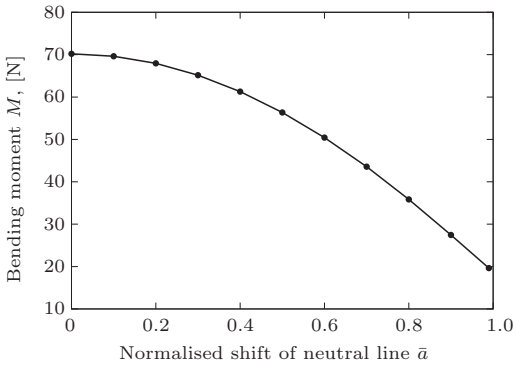

Figure 2.8: Effect of tension on the bending moment in elastic-plastic sheet.

the normalised shift of the neutral line, $\bar{a} = 2a/t$, is shown in Figure 2.8. It can be seen that for the case of no tension, $\bar{a} = 0$, the bending moment has its highest value. Applying tension during the deformation decreases the bending moment and, as defined in Equation (2.38), reduces the amount of springback. For a material with an arbitrary hardening the moment is not reduced to zero when $\bar{a}$ reaches the maximum value. Even if the neutral line is situated outside the sheet thickness, a non-zero bending moment exists and a small change of shape upon unloading is expected.

This example demonstrates the principle behind the commonly used method for springback reduction. In an industrial sheet metal forming operation, stretching the sheet during the deformation ensures decreased geometrical error due to the bending type of springback.

2.3 Numerical modelling

Adequate FE modelling of the springback phenomenon is discussed in this section. The following aspects of FE analysis of sheet metal forming are carefully examined: material modelling, contact conditions, element type, unloading method, time integration scheme and equivalent drawbeads. This section is based on findings in the literature and some results of an experimental and numerical study which was performed to evaluate the sensitivity of springback to various parameters. Three components of varied complexity, known to be sensitive to springback, were used in this study. Figure 2.9 shows the first characteristic component - the unconstrained cylindrical bending - defined as the benchmark problem at the NUMISHEET 2002 conference [22]. The second characteristic component is the scaled-down car roof provided by Corus RD&T, see Figure 2.10. The third component is the NUMISHEET 1993 benchmark problem shown in Figure 2.4(a). A detailed description of geometric and process parameters of these test is given in Appendix A.

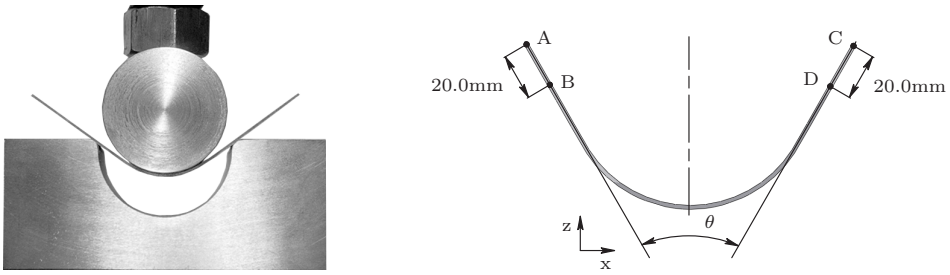

Figure 2.9: Unconstrained cylindrical bending - NUMISHEET'02 benchmark: a) shape at intermediate step during forming; b) definition of angle θ used to quantify springback.

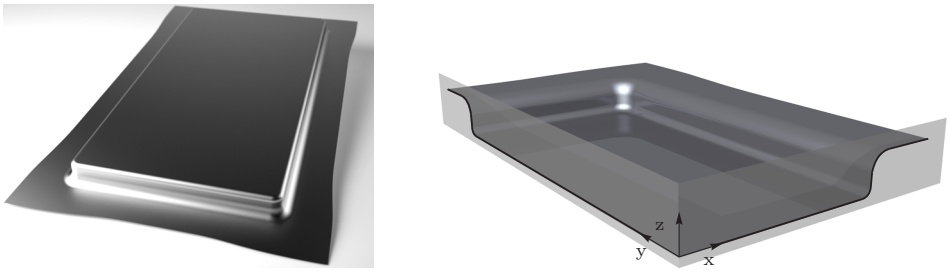

Figure 2.10: Scaled-down car roof: a) shape of the part; b) a quarter of the part, definition of measuring planes.

2.3.1 Material behaviour

The choice of an appropriate material model is one of the crucial steps in preparing a numerical set-up for analysis of sheet metal forming. Generally, material modelling can be divided into two parts: a part that describes the stress state of the initial yielding of the material (yield function) and a part that describes how the yield function develops with plastic deformation (hardening law).

Yield function

The yield function used in a numerical analysis is one of the factors which has a significant influence on the internal stress state at the end of a deformation. Numerous studies that compared the performance of different yield criteria emphasised the importance of choosing an appropriate yield function for accurate springback prediction [30, 62–69]. A yield function can be defined as the surface which encloses the elastic region in a multi-axial stress space. Usually, in the analysis of sheet metal forming all out-of-plane components of the stress vector are assumed to be equal to zero and a yield criterion is formulated in the plane stress space.

Simple yield criteria such as Tresca or von Mises are only applicable in the analysis of academic problems. Their parameters are defined using the uniaxial tensile test and these functions are only suitable for describing yielding of isotropic materials. Generally, metals behave anisotropically since their mechanical properties depend upon the chosen direction within the specimen. Planar anisotropy of sheet metals develops during the rolling process and it is the result of different features of the material microstructure [70].

To accurately calculate the internal stress state at the end of a deformation, a yield function must be used which is able to capture the important anisotropy effects [62–64, 71]. A simple, widely used yield criterion which can represent the behaviour of some planar anisotropic materials is the quadratic Hill'48 function. Its parameters are determined using three uniaxial tensile tests. The major drawback of the Hill'48 function is that it gives an inaccurate description of yielding of materials with low R-values, e.g. aluminium alloys [62, 64, 70]. To demonstrate this, the Hill'48 yield locus for aluminium alloy AA5182 is plotted in the normalised principal stress space (see Figure 2.11). In this figure σ_y is the average of the uniaxial yield stresses measured in the 0°, 45° and 90° directions with respect to the rolling direction. Solid dots represent the experimental stress points obtained from four different tests [23]. As can be seen, the Hill'48 criterion predicts a much lower equi-biaxial yield stress. Ultimately this means that in the numerical analysis, when using the Hill'48 function, yielding of the material in the equi-biaxial stress state will be initiated at much lower level of strains. Therefore the accuracy of the stress state and subsequent change of shape upon unloading will be questionable. To overcome this problem, more advanced yield

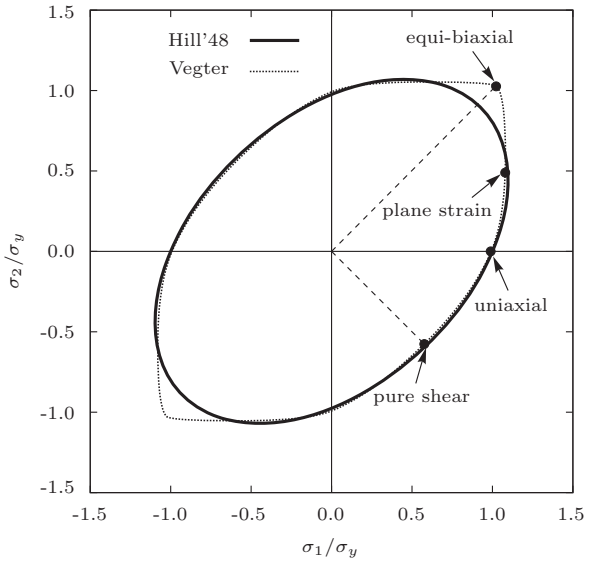

Figure 2.11: Initial shape of the yield locus of AA5182 alloy represented by different yield functions.

criteria proposed by Hill [72], Hosford [73], Barlat [64, 74] and Vegter [75, 76] can be used. These yield functions take into account data from various multiaxial tests. For example the Vegter criterion is defined in the plane stress situation using the experimental data obtained from the shear, uniaxial, plane strain and equi-biaxial tests. As shown in Figure 2.11, since this function uses the experimental stress points directly it gives a more accurate description of initial yielding of the aluminium alloy.

Extra parameters introduced in formulations of all these functions enhance their ability to fit the experimental data. Only by using a sufficient number of parameters, is it possible to reach a high accuracy in describing directional dependency of the yield stress and R-value, caused by the material anisotropy [62, 64, 65, 71]. Despite obvious drawbacks related to the FE implementation and a more complex experimental procedure for identification of parameters, the advanced yield functions can provide a better prediction of the stress state and resulting springback upon unloading.

Hardening model

The accuracy of springback prediction strongly depends on the hardening law used in the numerical analysis. The hardening law describes evolution of the initial yield surface which may change its size, position and even shape due to plastic deformation. A uniform increase of the yield surface can be modelled with isotropic hardening. In this case, the centre of the surface is fixed and its shape remains unaltered. A shift of the yield surface with no change in shape and size can be modelled using kinematic hardening. These are the simplest models that can only partially describe the evolution of the initial yield surface.

A change of shape of the yield surface is caused by evolution of the crystallographic texture during the deformation and resulting change of material anisotropy. This so-called deformation-induced anisotropy can be described using phenomenological models [77] or polycrystal models that are able to predict the rotation of individual grains. However, complete modelling of the deformation-induced anisotropy can be very time consuming and computationally expensive [64, 78]. Therefore, in sheet metal forming, in order to simplify the analysis it is often assumed that the change of anisotropic properties during forming is small and negligible when compared to the initial material anisotropy [64].

The simple hardening models cannot accurately describe the behaviour of the material under strain path changes. In general, in sheet metal forming a material point may follow a non-constant strain path during the deformation. Effects of the strain path changes on the stress-strain relation are illustrated in Figures 2.12 and 2.13. They represent the results of reverse and orthogonal tests performed on the biaxial testing machine with interstitial free steel DC06 [79]. In the reverse test the material is subjected to a simple shear deformation of opposite sign. As shown in Figure 2.12, the material exhibits typical stages of the Bauschinger effect: early re-yielding, smooth elastic-plastic transition and workhardening stagnation which appears after the material resumes hardening when loaded in the reverse direction [80]. Some materials may also exhibit permanent softening during reverse loading. It is

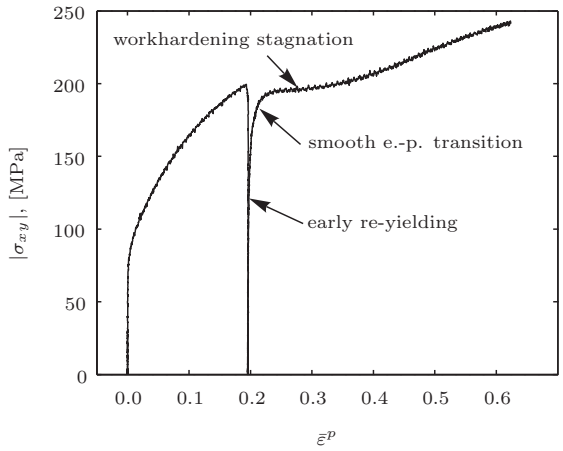

Figure 2.12: Stress-strain relation for DC06 steel during reverse loading.

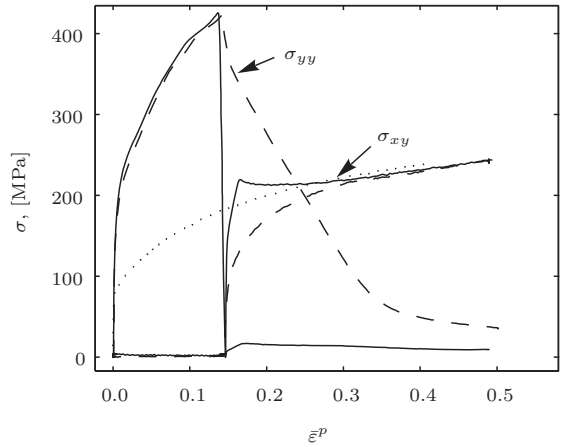

Figure 2.13: Stress-strain responses of the material during orthogonal loading. Sudden and gradual strain path changes are indicated by solid and dashed curves correspondingly. The dotted curve represents the monotonic simple shear test.

characterised by a stress offset observed in the region where the reverse workhardening rate is lower or almost equal to that during the forward deformation [51, 80].

In the orthogonal tests the specimen is first loaded in the tensile direction and after that in the shear direction. As shown in Figure 2.13, if the strain path change is done

gradually the shear stress also converges gradually to the value obtained in simple shear test. On the other hand, an abrupt change of the strain path causes the shear stress to increase rapidly to a higher value before dropping to the level of the simple shear test. Presence of the overshoot during a sudden change of the strain path is related to the dislocation structure and its evolution during the deformation [79].

To ensure an accurate prediction of the springback phenomenon in sheet metal forming it is necessary to use hardening models which are able to describe the effects of strain path changes [17, 39, 71, 80]. A lot of attention in the scientific literature has been given to phenomenological hardening models that can describe the most important phenomena which occur during reverse loading. The first anisotropic hardening models, e.g. the multi-surface model proposed by Mroz [81], the two-surface model of Krieg [82] and the nonlinear kinematic hardening model of Frederick and Armstrong [83], had some limitations and could not fully describe the Bauschinger effect in metals [84, 85]. Subsequent developments were more successful. For example, based on the framework of isotropic/kinematic hardening and Mroz's multi-surface model, Gau and Kinzel [40] proposed a hardening model that takes into account the Bauschinger effect and is able to accurately predict springback when the sheet material undergoes a complicated deformation path. The basic concept of the Frederick and Armstrong model was extended by various authors. The main focus was given to improving the modelling, incorporating additional experimentally observed phenomena and accommodating more complex loading cases [71, 83, 84, 86–88]. Modifications of the two-surface hardening model developed by Krieg were proposed by Huétink et al. [89] and Yoshida et al. [51, 80, 90]. The Yoshida-Uemori model describes all features of the Bauschinger effect, including workhardening stagnation, and it is also able to accurately describe the strain-range dependency of cyclic hardening [90]. The latter phenomenon is related to the experimentally observed dependency of cyclic stress amplitudes on cyclic strain ranges.

The phenomenological models discussed above are not capable of describing the effects of orthogonal loading. Expanding these models to describe for example the stress overshoot is not practical since it would lead to even more complex formulations with extra material parameters which must be identified [78]. Dislocation based anisotropic hardening models are more suitable for describing the phenomena observed during strain path changes. A physically based model proposed by Teodosiu can be used on a macroscale with some of the mentioned yield functions [91, 92]. To define the model, 13 material parameters are needed, which must to be determined from multiple tests. This hardening model is able to describe the Bauschinger effect, workhardening stagnation, permanent softening and the stress overshoot.

In general, the major drawbacks of physically based models are the large number of material parameters and considerable computational costs that are required to obtain a reliable description of material hardening. However, these models, when used in combination with advanced yield functions, can ensure a more accurate description of the material behaviour during the deformation and can provide a better prediction of the final state variables at the end of forming.

2.3.2 Contact description

Another important factor that influences the results of a springback simulation is the description of contact between the blank and the tools. In an analysis of sheet metal forming the contact conditions are usually described based on the following considerations [93]:

- the material cannot penetrate the tool and if there is contact, the gap between the material and the tool is zero;
- in case of no contact, there are no contact forces between the blank and tool.

In order to obtain the accurate stress state at the end of forming it is important to avoid artificial penetrations or incorrect contact forces during the simulation. The Lagrange multiplier method and the penalty method are the main methods used to incorporate the contact conditions into a finite element formulation. An extensive description of both methods can be found in [12, 93, 94]. According to the Lagrange multiplier method the non-penetration contact conditions are enforced exactly, but at the cost of extra degrees of freedom. In the case of the penalty method, the non-penetration conditions are weakly enforced and the penalty is viewed as a contact stiffness. The major advantage of the method is that no extra degrees of freedom are required. There is always a small amount of penetration and for no penetration an infinite contact stiffness is needed. However, high values of the contact stiffness are not recommended since it has a destabilising effect on the convergence behaviour of the simulation.

Both methods are equally frequently employed in simulations of sheet metal forming [95, 96]. When using the penalty method, the contact stiffness value must be carefully chosen since it may have a considerable effect on the amount of springback [30]. To demonstrate this influence, several simulations of component 1 (see Figure 2.9) are performed in the FE code DiekA. The angle θ, calculated after forming and springback for various values of the contact stiffness, is presented in Table 2.1. Results show that by varying this contact parameter, a difference of 2.0° in the forming angle can be obtained. Using low values of the contact stiffness increases the penetration depth and modifies the actual geometric parameters of the problem. This explains the difference in forming angle and subsequently in the angle after springback.

Table 2.1: Component 1: influence of contact stiffness on the angle θ after forming and springback.

Contact stiffness, [MPa/mm]	Angle θ, [°] after forming	springback
100	22.68°	56.91°
200	21.95°	56.42°
300	21.63°	56.13°
400	21.45°	55.98°
500	21.33°	55.88°
2500	20.73°	55.45°
5000	20.60°	55.33°

An appropriate description of friction is also important for the accurate prediction of the final stress state at the end of forming. The commonly used Coulomb model assumes a constant coefficient of friction, whereas this does not entirely correspond to reality [12]. The coefficient of friction depends on the local contact conditions, which differ for each sheet/tool contact. For an accurate springback prediction it is beneficial to use a more advanced friction model, e.g. the Stribeck model, in which the friction coefficient depends on the pressure and viscosity of a lubricant between the contacting surfaces, the tool's velocity and the surface roughness.

Here, the sensitivity of springback to a variation of friction coefficient is investigated based on the numerical analysis of component 2 (see Figure 2.10) in the FE code DiekA. A set of simulations is performed in which the coefficient of friction is varied from 0 to 0.2. The shape of the part after unloading in both symmetry planes is shown in Figure 2.14. The punch geometry at the end of the forming stroke is also added to this plot. The amount of springback is very sensitive to the chosen coefficient of friction. When looking at the bottom of the part, along the $x-$symmetry axis, it is possible to see that the springback decreases with increasing the coefficient of friction. This can be explained by recalling the theory presented in Section 2.2. Higher friction introduces more in-plane strain in the product, which reduces the resulting bending moment and decreases the amount of springback. However, the product shape along the $y-$symmetry axis shows the opposite trend. The springback increases with increasing the coefficient of friction. Due to the geometry of the part, high membrane stresses develop during forming along the $y-$symmetry axis. Since the combined bending and membrane springback occurs during the unloading, the relaxation of the membrane stresses has a considerable influence on the change of shape of the part along this axis. A higher friction coefficient yields higher membrane stresses, which increases the amount of membrane springback and the potential for warping. These results additionally demonstrate that overstretching the parts during forming, by for example applying a higher coefficient of friction or using higher blankholder forces, may not necessarily be the best method for controlling springback in sheet metals.

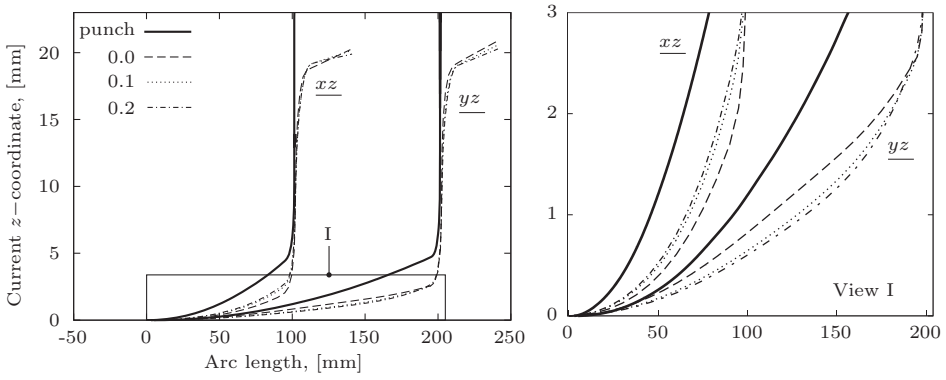

Figure 2.14: Component 2: influence of coefficient of friction on the change of shape. Blank geometry in $xz-$ and $yz-$symmetry planes after springback.

2.3.3 Element type

The selection of an appropriate element type is also very important for accurate modelling using FE analysis. Depending on the problem and the geometry of the sheet metal part, different types of elements can be used to discretise the blank, i.e. 2D plane strain, shell, solid or solid-shell. Due to computational efficiency, shell elements are commonly used in simulations of sheet metal forming. They are based on different plate bending theories which are applicable to situations when the material thickness is considerably smaller compared to other dimensions. The theories assume that while bending a plate, a plane stress state occurs and that the plate geometry is represented by the mid-plane. Since only the mid-plane of the plate is discretised by elements the amount of independent degrees of freedom can be reduced significantly.

In some cases, to speed up the analysis time, a fully three-dimensional (3D) problem is represented by a model which uses 2D plane strain elements. Although these models can be accurate enough for the analysis of forming, the accuracy of springback prediction may be questionable. To visualise this, the performance of a quadrilateral plane strain element (CPE4I, [97]) and a shell element (S4R, [97]) was compared using simulations of the characteristic component 1 in FE program Abaqus/Standard. Two different scenarios were considered, i.e. with and without friction. Values of the angle θ calculated after forming and springback are listed in Table 2.2. First, it must be pointed out that for both models the angle after springback in the simulations without friction is considerably less compared to the analysis with friction. This is related to a difference in the deformation history. Figure 2.15 shows an intermediate step during forming with and without friction. In the simulation with $\mu = 0$, due to the absence of friction forces, the contact between the punch and blank is lost when a certain displacement is reached. This does not happen in the analysis with friction and the contact is always present until the end of forming.

When looking at the results predicted by the plane strain and shell models in the case with friction, it is possible to see that the absolute difference between the angles after springback is minor. The situation changes when the friction is excluded from the simulations. The absolute difference in this angle becomes 4.4°. In the absence of friction an anticlastic curvature can easily develop in the central part of the blank since it is not restricted by the punch. Its appearance increases the actual section modulus for the principal bending and, as shown in Table 2.2, reduces the amount of springback. In the analysis with friction, the anticlastic bending effects are restricted by the tool, since the contact between the punch and sheet is preserved during the simulation. The results show that a plane strain model neglects the lateral bending effects and this may lead to a considerable drop in the accuracy of springback analysis.

Table 2.2: Component 1: influence of the element type on springback.

Element type	$\mu = 0$		$\mu = 0.1348$	
	forming	**springback**	**forming**	**springback**
Plane strain	20.94°	47.69°	20.90°	53.55°
Shell	20.89°	43.30°	20.92°	53.27°

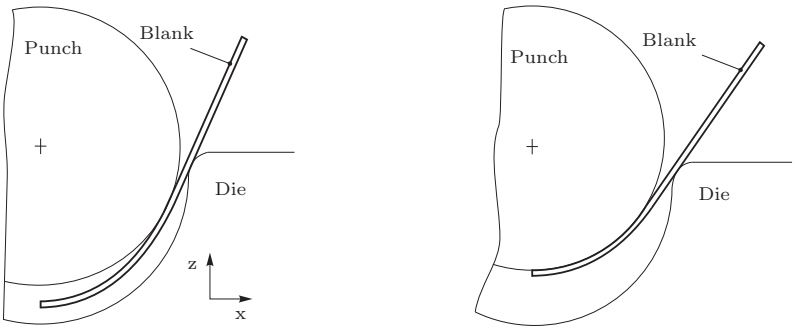

(a) $\mu = 0$ (b) $\mu = 0.1348$

Figure 2.15: Component 1: intermediate stage during forming.

It is important to remember that the traditional shell element formulations are based on the assumptions that the plane stress state prevails and in-plane strains are linearly distributed across the thickness. It is arguable if these assumptions are fulfilled in the entire computational domain [44, 98–101]. For example, a shell theory is not applicable in situations when the tool radius is comparable to the sheet thickness. Li et al. in [44] carried out a numerical study using the draw/bend test, described in Figure 2.5. It was concluded that, if the ratio R/t is less than 5, a fully 3D stress state exists and solid elements are required in the simulation of springback. These elements can accurately calculate the stress gradients in the thickness direction, as well as evolution of the sheet thickness, during a simulation [44, 101].

However, using solid elements for simulation of industrial sheet metal forming problems is inefficient. It is known that at least two layers of solid elements need to be used to accommodate the stress gradients that occur in the thickness direction. Moreover, the ratio between the element dimensions in the plane and through the sheet thickness must be small enough to avoid deterioration of the stiffness matrix [100]. Therefore, the major drawback of solid elements is the enormous CPU time and memory consumption required to complete the simulation [12, 102].

To eliminate these problems, one can use m-refinement in which solid elements are employed in the regions of the blank which may experience a fully 3D stress state, and shell elements in the remaining part of the blank [103]. A more practical recent solution is to use solid-shell element formulations that account for the normal stress in the thickness direction and show excellent performance in springback analysis, see for example [104, 105].

2.3.4 Unloading method

Generally, every simulation of springback phenomenon in sheet metal forming comprises two major steps: loading (actual forming of a product) and unloading (springback). Two different methods can be used to simulate the unloading step. Instantaneous tool release is the method which is commonly used in industrial practice

due to its computational efficiency. When using this method a change of the blank shape during the unloading is calculated in one increment. All contact forces are suddenly removed, transformed into the residual forces which are then reduced to zero. The material response is calculated under the assumption of fully elastic deformations in the complete model [30, 106, 107]. Sometimes this increment is subdivided into a number of subincrements in order to avoid numerical instabilities. Alternatively, a gradual tool release can be used during the unloading. This method can be viewed as inverse forming, during which loads are reversed and the tools are gradually retracted. Although this method is more realistic due to the contact forces being present during the unloading step [17, 30, 54, 108, 109], it is less popular because it is computationally costly. The influence of the unloading method on the accuracy of springback prediction was studied using components 1 and 2. Two sets of simulations of component 1 were performed in which the instantaneous and gradual tool release methods was used. In the first set, the friction coefficient was set to zero and in the second set the friction was included in the analysis. All other simulation parameters were left unchanged and the numerical study was performed in the FE program Abaqus/Standard. Results of all four simulations are summarised in Table 2.3 where angle θ after springback is presented. As can be seen, there is no difference between the two unloading methods in the frictionless situation. However, if friction is included, the springback angle can vary up to 2° depending on whether the tools are released instantaneously or gradually. The reason behind this discrepancy lies in the

Table 2.3: Component 1: influence of tool release method on springback.

Tool release method	$\mu = 0$	$\mu = 0.1348$
Instantaneous	43.30°	53.27°
Gradual	43.35°	55.26°

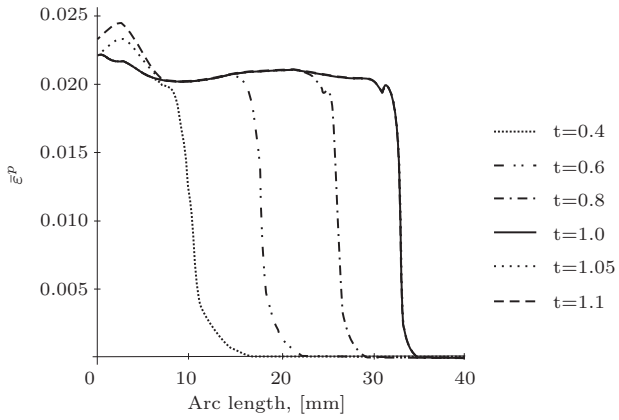

Figure 2.16: Evolution of the equivalent plastic strain along the top of the sheet during forming and unloading.

presence of tangential friction forces, that act between the blank and the tools. Soon after the gradual unloading procedure is initiated, the friction between the punch and blank causes tangential forces directed towards the blank centre. Since this region of the blank was in compression during the forming step, adding the compressive forces will promote further plastic straining upon unloading. The equivalent plastic strain along the top of the sheet is plotted in Figure 2.16 as a function of the current arc length. Since the blank is symmetric, only the strain distribution in its right part is reported. The curves in this plot are given for several stages during forming (until t=1.0 sec.) and several stages during springback (until t=1.1 sec.). This figure shows that the plastic strain near the punch centre starts to increase as the unloading is initiated. This variation of internal variables during the physical unloading causes a variation of angle θ after springback. No change of the plastic strain was observed in the case of instantaneous tool release. Effects of the latter physical phenomenon are completely neglected which leads to purely elastic unloading and underestimation of the amount of springback.

Numerical analysis of component 2 showed that using the instantaneous tool release method during unloading may cause additional problems. The results of two

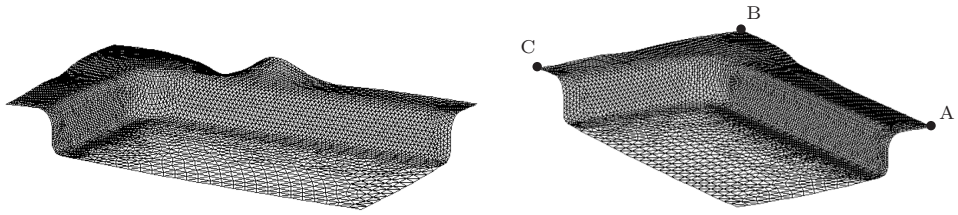

(a) instantaneous tool release (b) gradual tool release

Figure 2.17: Component 2: influence of unloading method on springback.

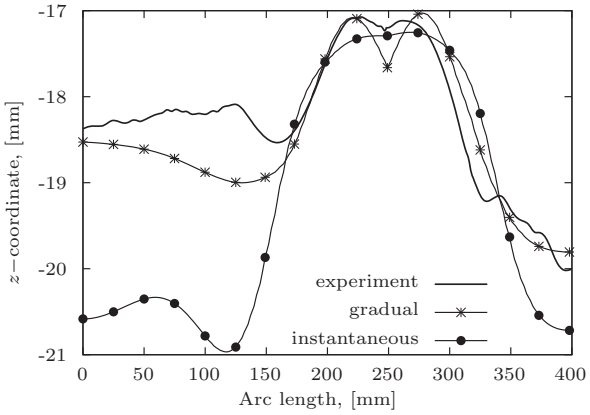

Figure 2.18: Component 2: shape of the blank along the free edge after springback.

simulations of stamping of the scaled-down car roof performed in the implicit FE code DiekA are shown in Figure 2.17. During forming, high compressive stresses develop in some parts of the flange and thus it tends to buckle when the external loads are removed. As shown in Figure 2.17(a), the instantaneous tool release method is not a good option for this type of problem. A realistic shape of the blank after springback can only be obtained if artificial stabilisation techniques are used. On the contrary, when using a gradual tool release, the buckling instabilities are controlled by the moving blankholder, and thus the expected product shape can be obtained (see Figure 2.17(b)). The results of both simulations are compared to the experimental measurements. The shape of the part after springback along the free edge ABC is depicted in Figure 2.18. It can be seen that the flange shape predicted by the simulation with the gradual tool release is more realistic and is in better agreement with the experimental shape.

2.3.5 Time integration scheme

Dynamic explicit and static implicit algorithms are the main solution procedures for the simulation of sheet metal forming. Since metal forming processes are relatively slow, they are often considered to be quasi-static which means that inertia effects are neglected. In this case, to simulate the process a static implicit finite element solution procedure is used. The state variables that satisfy the equilibrium during every incremental step are found iteratively, using for example the Newton-Raphson method. In this way equilibrium conditions are checked at every time increment, leading to more reliable results. The major drawbacks of implicit methods are difficulties in finding the converged solution within a time increment and the rapid increase in computation time when a direct solver is used [110, 111].

These drawbacks can be eliminated by using dynamic explicit methods. In an explicit method, the inertia effects are considered and the update of state variables at any time step may be done without solving a system of equations. As a result, this FE procedure does not suffer from convergence problems. Additionally, compared to the implicit methods, memory requirements are minimised and in some cases the final solution can be obtained faster. The main disadvantage of explicit methods is the necessity of using very small time steps during the solution process [112]. To overcome this problem, mass scaling or increased process speed are often used.

Both time integration algorithms can be applied in simulations of the springback phenomenon in sheet metal forming. Accurate results have been reported after using only an explicit analysis for both forming and unloading steps [96, 110, 113] or only implicit analysis [30, 44, 106]. The following remarks could be helpful for choosing the time integration algorithm:

- due to the artificial adaptations of the model (mass scaling or increased tool speed) the accuracy of the dynamic explicit scheme relies, to a larger extent than for implicit methods, on the expertise of the analyst [96, 111]. If the dynamic effects are not sufficiently suppressed, the blank may start to oscillate during unloading and its final shape may be difficult to find [108]. On the other

hand, excessive mass scaling may lead to an inaccurate stress state after forming and unrealistic product shapes after springback [106, 114];

- if the springback step is modelled with the instantaneous tool release method described in Section 2.3.4, it is not practical to use the dynamic explicit solution procedure. The static implicit method with its large time steps is much more computationally efficient in this situation [108, 115–117]. There are no changes in contact conditions and thus the implicit simulation is stable. Using the dynamic explicit procedure to simulate the springback step may require the same computation time needed for the simulation of the forming step [111];
- if the gradual unloading method is used during the springback step, changing contact conditions can have a detrimental effect on the convergence behaviour of the static implicit analysis. It may be required to use some numerical stabilisation techniques to decrease the total computation time;
- due to the unrealistically high computation time and memory requirements, it may not be possible to use the static implicit FE analysis in combination with a direct solver in simulations of large 3D models [111];
- automatic numerical stabilisation techniques are often employed to control the convergence behaviour of static implicit codes. For an accurate springback analysis, their use must be minimised since they can have a significant effect on the change of shape during unloading [30].

Several algorithms that combine the merits of both time integration schemes have been proposed. Van den Boogaard et al. [111] developed an efficient FE solution procedure for analysis of sheet metal forming. The method is based on the implicit scheme that guarantees accurate results due to the equilibrium check. Dynamic terms are introduced into the code, which has a stabilising effect on the convergence behaviour of a simulation. Additionally, including inertial effects helps to make an effective use of iterative solvers in the analysis. As a result, it becomes possible to use the implicit scheme in simulations of large 3D models.

Another interesting approach was originally proposed by Jung [118] and later extended by Noels [119]. Keeping in mind the advantages of implicit and explicit schemes, the optimum solution is to have both methods available in the same FE code and to be able to switch automatically between them within one simulation [119]. As soon as the convergence behaviour of the implicit solution deteriorates, the explicit scheme is employed. After passing the difficult point of simulation the solution strategy is switched back to the implicit algorithm.

2.3.6 Iterative solver

Results of a FE simulation of springback can be affected by the method used to solve the global system of equations. This is mainly true for the static implicit FE solution procedure. Explicit methods do not require the solution of any system of equations provided that the mass matrix is diagonal [112]. When using the static implicit FE

procedure the following equilibrium equation must be satisfied at every incremental step:

$$\{\mathbf{0}\} = \{\boldsymbol{r}_n\} = \{\boldsymbol{f}_n^{int}\} - \{\boldsymbol{f}_n^{ext}\} \tag{2.39}$$

where the subscript n denotes the incremental step number, $\{\boldsymbol{f}_n^{int}\}$ and $\{\boldsymbol{f}_n^{ext}\}$ are the internal and external force vectors respectively and $\{\boldsymbol{r}_n\}$ is the vector of the residual forces. The set of discrete equilibrium equations (2.39) is generally non-linear in the nodal displacements $\{\boldsymbol{d}_n\}$. Therefore, to find the vector of the nodal displacements at the current step, Equation (2.39) is usually solved using the iterative Newton-Raphson procedure. In the Newton method the iterative displacement increments $\{\Delta\boldsymbol{d}_k\}$ are found from:

$$[\boldsymbol{K}_k]\{\Delta\boldsymbol{d}_k\} = -\{\boldsymbol{r}_k\} \tag{2.40}$$

where k is the iteration number and $[\boldsymbol{K}]$ is the tangent stiffness matrix. The calculated iterative displacement increments are used to update the displacement vector of the current step:

$$\{\boldsymbol{d}_{k+1}\} = \{\boldsymbol{d}_k\} + \{\Delta\boldsymbol{d}_k\} \tag{2.41}$$

The iterative solution procedure is stopped if in iteration k the ratio of ℓ_2 norms is less than some predefined value ε:

$$\frac{\|\{\boldsymbol{r}_k\}\|_2}{\|\{\boldsymbol{f}_k^{int}\}\|_2} = \varepsilon_k \leq \varepsilon \tag{2.42}$$

Two groups of methods can be used to solve the linear system of equations (2.40), i.e. direct solvers and iterative solvers [120]. Most of the direct solvers are based on Gaussian elimination. These methods can find a very accurate solution of a linear system of equations. The major drawback of the modern direct solvers is the high memory requirement in large-scale FE simulations [111]. For large problems, iterative solvers are generally preferred, since they solve the global system of equations using less memory than a direct solver. An iterative method finds an approximate value of the iterative displacement increments $\{\Delta\widehat{\boldsymbol{d}}_k\}$ within a predefined accuracy:

$$[\boldsymbol{K}_k]\{\Delta\widehat{\boldsymbol{d}}_k\} = -\{\boldsymbol{r}_k\} + \{\boldsymbol{\epsilon}\} \tag{2.43}$$

Usually, an iterative solver will continue calculations until the ℓ_2 norm of the error vector $\{\boldsymbol{\epsilon}\}$ is less than some fraction δ_{it} of the residual norm:

$$\|\{\boldsymbol{\epsilon}\}\|_2 \leq \delta_{it}\|\{\boldsymbol{r}_k\}\|_2 \tag{2.44}$$

When the Newton-Raphson process converges to an accurate solution, the residual $\{\boldsymbol{r}_k\}$ becomes small and, as can be seen from Equation (2.44), the iterative solver will be requested to reach unnecessary high accuracy. Therefore in practice the parameter δ_{it} is calculated during the analysis, based on the global convergence [111]:

$$\delta_{it} = \eta\,\frac{\varepsilon}{\varepsilon_k} \tag{2.45}$$

The number of iterations needed for an iterative solver to reach a specified accuracy is not fixed. It depends on the used convergence criterion and the condition number

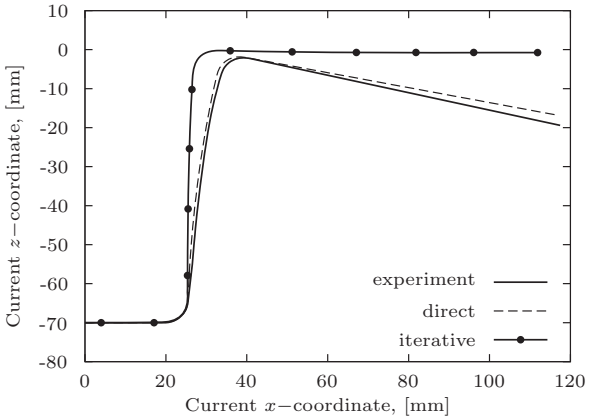

Figure 2.19: Component 3: influence of solver type on springback.

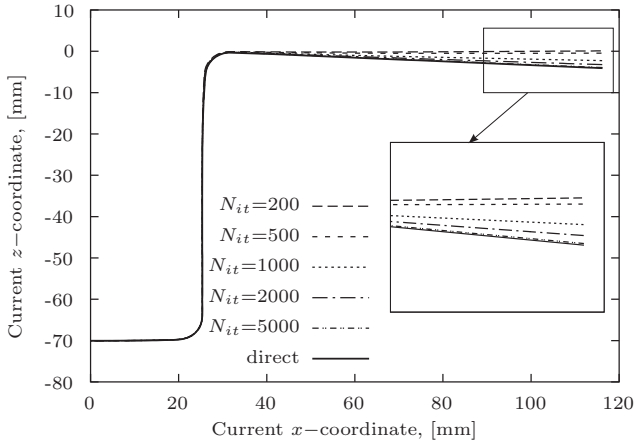

Figure 2.20: Variation of springback amount with the number of local iterations. Intermediate step of unloading.

of the tangent stiffness matrix [111, 121]. The accuracy of a springback simulation may be questionable if an iterative solver is not allowed to exceed a certain predefined number of local iterations, when this number is not high enough. To demonstrate this, simulations of component 3, depicted in Figure 2.4(a), were performed in the implicit FE code DiekA. First, two simulations were run using the direct solver PARDISO and the Conjugate Gradient iterative method with the number of local iterations limited to 200. Practically this means that the iterative solver will stop calculations if this number is exceeded. In this case, the last computed values of the iterative displacement increments $\{\Delta\widehat{\boldsymbol{d}}_k\}$ are considered to be the final answer. A detailed description of the solvers can be found in [120, 122]. In both simulations the tolerance

of the Newton-Raphson method is set to 2% ($\varepsilon = 0.02$). In the simulation with the iterative solver, the parameter η is chosen to be 0.1 - the value which is typically recommended in the literature [111].

Comparison of results right after forming shows no difference between both solvers. The situation changes drastically during the springback step. Figure 2.19 shows the shape of the part after springback in the $xz-$symmetry plane. Due to the symmetry, only a half of the part is shown. The average experimental data, presented at the NUMISHEET 1993 conference, are added to this plot. Despite the fact that the convergence criterion of the Newton-Raphson procedure is globally satisfied, the final shape of the part, obtained in the simulation with the iterative solver, is very unrealistic. Results of the simulation with the direct solver are in good agreement with the real shape, while the observed discrepancy is probably related to an inappropriate description of contact conditions during the numerical analysis. Several additional simulations were performed in which the iterative solver was allowed to use a higher number of the local iterations (N_{it}). Figure 2.20 shows the shape of the part in the same symmetry plane at an intermediate step of the gradual unloading procedure. As shown in this figure, by increasing the number of local iterations the accuracy of prediction of the change of shape during unloading can be improved. However, using more local iterations has a negative effect on the simulation time. To reach this point of the gradual unloading procedure the iterative solver with 5000 local iterations requires approximately 4 times more CPU time than the direct solver.

These results demonstrate that for the accurate simulation of springback a direct solver is preferable. If an iterative solution method must be employed due to the memory size limitations it is important that the solver be allowed to use a sufficiently high number of local iterations to reach the specified accuracy.

2.3.7 Equivalent drawbeads

The quality of a sheet metal part is defined by the material flow into the tool cavity. When forming shallow or arched parts, drawbeads are usually incorporated into the tools (as shown in Figure 2.2) to introduce an additional stretching and to assure that the material flows in a more uniform way. In a numerical analysis, however, modelling the exact drawbead geometry requires a large number of elements due to the small radii of the drawbead. Therefore, it is a common practice to use an equivalent drawbead model which replaces the real drawbeads and helps to avoid a drastic increase in the computation time [123]. An equivalent drawbead can be represented by a line on a tool surface. When a finite element passes this line it obtains an additional drawbead restraining force and a plastic strain, while a lift force is subtracted from the total blankholder force.

Simulations of stamping of the automotive underbody cross member, shown in Figure 2.21, revealed that for an accurate springback analysis it is better to avoid using an equivalent drawbead model. This conclusion came from evaluating the results presented at the NUMISHEET 2005 conference [4]. Figure 2.22 shows the experimentally obtained distribution of the true thickness strain in cross-section I-I

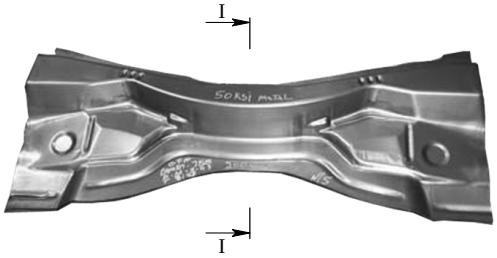

Figure 2.21: Automotive underbody cross member - NUMISHEET'05 benchmark #2 [4].

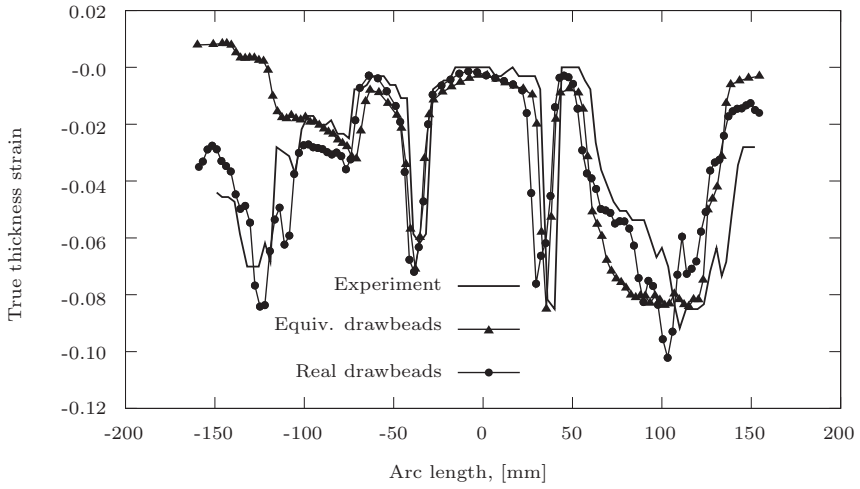

Figure 2.22: True thickness strain distribution after forming in section I-I for dual phase steel (DP965).

of the part. The simulation results of participant BM2.03 (using FE package DiekA and an equivalent drawbead model) are also presented in this plot. As can be seen, the simulation with the equivalent drawbeads predicted thickening of the material in the region from $-100mm$ to $-200mm$. A similar trend can be found in the results submitted by other benchmark participants, who made use of an equivalent drawbead model (see e.g. the results of BM2.20 in [4]). However, the experiments show thinning of the material in this region, which is also predicted by the benchmark participants who used real drawbeads in their analyses. Therefore, an extra simulation was performed in DiekA with the real drawbeads and all other parameters similar to the original ones. As shown in Figure 2.22, this simulation predicts a true thickness strain distribution which is in better correspondence with the experimental results. A reasonable explanation can be found in a difficulty of selection of parameters of an equivalent drawbead model. These parameters can be calculated using a plane strain set-up that simulates a situation in which material is pulled through a drawbead.

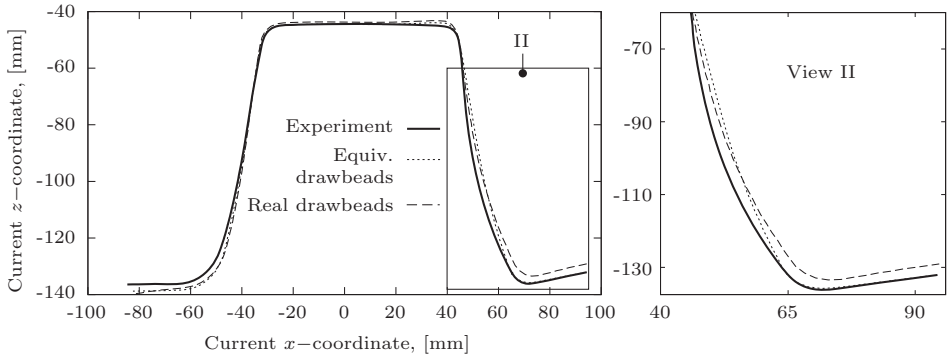

Figure 2.23: Springback profile in cross-section I-I, DP965.

Results of this simulation are influenced by the gap between the male and the female bead and a correct value of this gap is difficult to identify. Besides, it is arguable whether the gap stays constant during real forming. The plane strain assumption and the uncertainty about the gap value tends to result in the parameters of an equivalent drawbead model being under- or overestimated, which leads to a difference in process conditions and thus affects the final stress state.

Additionally, when using an equivalent drawbead model one has to keep in mind that the information about the complex stress state that occurs when a material passes several subsequent bending / unbending regions inside a drawbead is lost. This complex stress state in the sheet causes the formation of the side wall curl when the product is allowed to unload. Figure 2.23 shows the springback profile in the same cross-section of the automotive underbody cross member. The curvature in the product wall predicted by the simulation with the real drawbeads corresponds more to the experimental shape.

2.4 Recommendations for accurate modelling of springback

To guarantee an accurate prediction of the springback phenomenon in sheet metal forming using FE analysis, it is important to minimise modelling error. This can be achieved by taking the following into account:

- an accurate stress state at the end of a deformation can only be obtained if an appropriate material model is used. It is beneficial if the model is based on the initial yielding and hardening characteristics obtained from multiple tests. The model should be able to describe the material behaviour when it undergoes an arbitrary loading path. In addition to this, the material model should be able to describe the inelastic effects that may occur during unloading and which add to the total springback strain;

- the parameters of the contact description play an important role in the numerical analysis. If the penalty method is used, the contact stiffness value must be sufficiently high to accurately describe the geometry of tools. The coefficient of friction can have a large influence on the accuracy of springback prediction, The models capable of describing its variation during forming are preferable;

- while evaluating results of the numerical analysis it is important to remember that there are several types of springback in sheet metal forming. Using higher blankholder force or coefficient of friction reduces the bending springback but increases the amount of membrane springback. This may lead to larger distortions of the product shape during unloading;

- the appropriate type of elements must be used in the simulation. The approximation of a 3D problem with a 2D plane strain model is not an option since the anticlastic bending effects are completely neglected. Elements that account for stresses through the thickness of the material are required if the R/t ratio is less than 5;

- a gradual tool release method is recommended instead of an instantaneous release. Due to the presence of contact forces, the part may experience additional plastic straining during the unloading;

- dynamic explicit and static implicit schemes can be used in springback analysis. However, artificial adaptations of the model that are used to stabilise the convergence of an implicit scheme or to increase the time step of an explicit scheme must be applied with caution. For the implicit simulation of springback it is recommended to use a direct solver to find the solution of the global system of equations. In the case of memory size limitations, an iterative solver can be used in the analysis, provided that there is no limit on the amount of local iterations that must be performed to reach the specified accuracy;

- it is important to use real drawbeads in the springback analysis. If an equivalent drawbead model must be used, its parameters must be carefully defined.

CHAPTER

THREE

INFLUENCE OF DISCRETISATION ERROR ON SPRINGBACK PREDICTION

When FE analysis is applied to a mathematical model, the model is spatially discretised by dividing it into a mesh of finite elements. The spatial discretisation is an approximation of the problem geometry and, therefore, a potential source of errors. The discretisation error depends on the nature of element interpolating functions and some other details of the formulation of particular elements. Generally, it can be reduced by using more elements, since this increases the number of degrees of freedom in the model. A higher number of elements is usually needed to accurately describe a complex geometry or steep gradients in state variables. Typically, in sheet metal forming high stress gradients appear in places of abrupt changes of geometry, e.g. at a tool radius.

In simulations of the springback phenomenon, accurate results can only be obtained if the mesh density of the blank is chosen correctly. It is known from the literature that an accurate springback analysis requires more nodes which are in contact with the tool radius than is usually recommended in forming analysis [17, 30, 31, 44, 101, 124]. Li et al. in [17, 44], using the results of simulations of the draw-bend test shown in Figure 2.5, derived recommendations for the shell element size which can be used to reach an error of springback prediction of about 1%. Quadrilateral shell elements (S4R see in [97]), based on the Koiter-Sanders shell bending theory, were used in the study and it was concluded that in order to obtain this level of accuracy, one node per 5° of turning angle of the tool radius is required.

The appropriate tools' discretisation is equally important. If the tool surfaces are discretised rather of being defined analytically an insufficient number of elements describing the tool geometry may have several negative effects. Poor discretisation can simply modify the tool radius and can lead to a deviation of the product shape from that prescribed by the design. A small number of elements can create the situation where the tool's surface becomes rather sharp. This rough mesh may produce an

additional restraining force acting on the blank which can influence the amount of springback [125]. Finally, since the tools are discretised with a number of elements, the movement of the blank nodes over a tool radius is piece-wise straight. A very coarse mesh in this region can lead to a drastic variation of contact conditions which will deteriorate the convergence behaviour of a simulation [30].

In industrial sheet metal forming the geometry of the parts is usually very complex and includes multiple regions with small radii. The recommended number of 18-20 elements over a tool radius for the blank discretisation places high demands on the CPU time and memory requirements. For example, when using a direct solver in the numerical analysis, a uniform decrease in the shell element size results into a fourth order increase in computation time [111]. Furthermore, using more elements to describe the tools also leads to a significant increase of memory usage and simulation time. A certain percentage of a calculation is occupied by a contact search algorithm during which the blank nodes that are in contact with the tools are found. Increasing the number of tool elements will increase the contact search time.

This chapter describes results of a numerical study performed to develop the guidelines for the blank and tools' discretisation which can help to find a balance between the efficiency and the accuracy of springback prediction. Discrete Kirchhoff triangular shell elements are used in this study and the general description of this element type is given in Section 3.1. The guidelines for the blank discretisation are defined in Section 3.2 and tested using two sheet metal forming examples. Recommendations for the tool discretisation are defined and verified in Section 3.3.

3.1 Modelling a sheet in metal forming

Shell elements are commonly used in simulations of sheet metal forming since, compared to solid elements, they are more computationally efficient. Kirchhoff theory is one of the plate bending theories which is usually used to form the basis of formulation of thin shells. The theory prohibits a transverse shear deformation which means that any straight line normal to the mid-plane remains straight and normal during deformation. The main definitions of the theory are introduced in Appendix C; its complete description can be found in [121, 126].

In case of small deformations, the complete vector of strains for a shell element defined using the Kirchhoff theory can be written as:

$$\begin{Bmatrix} \varepsilon_{xx} \\ \varepsilon_{yy} \\ \varepsilon_{zz} \\ \gamma_{xy} \\ \gamma_{xz} \\ \gamma_{yz} \end{Bmatrix} = \begin{Bmatrix} u^{mp}_{,x} \\ v^{mp}_{,y} \\ f(\varepsilon_{xx}, \varepsilon_{yy}) \\ u^{mp}_{,y} + v^{mp}_{,x} \\ 0 \\ 0 \end{Bmatrix} - z \cdot \begin{Bmatrix} w^{mp}_{,xx} \\ w^{mp}_{,yy} \\ 0 \\ 2w^{mp}_{,xy} \\ 0 \\ 0 \end{Bmatrix} \tag{3.1}$$

Or in a more convenient form:

$$\{\boldsymbol{\varepsilon}\} = \{\boldsymbol{\eta}\} - z \cdot \{\boldsymbol{\kappa}\} \tag{3.2}$$

where $\{\boldsymbol{\eta}\}$ and $\{\boldsymbol{\kappa}\}$ define the membrane and bending parts of the deformation.

In practice, discrete Kirchhoff elements are used in which the transverse shear strains are not equal to zero throughout the element but only at specified locations - at nodes situated in the middle of an element side [127]. A typical discrete Kirchhoff triangular element has 18 degrees of freedom: 9 translational (three per node) and 9 rotational (three per node). The degrees of freedom of the element are shown in Figure 3.1. The stiffness matrix of this element can be derived by using a weak form of the shell equations for the balance of momentum [112, 121]. For a general elastic-plastic anisotropic material the stiffness matrix is a complex volume integral which can only be calculated by numerical integration.

Linear interpolation is used to find the in-plane displacement components u and v within the Kirchhoff plate. The lateral deflection along the element side w is described by a third order polynomial. As a result, as can be seen from Equation (3.1), the membrane part of the deformation $\{\boldsymbol{\eta}\}$ is constant and the bending part $\{\boldsymbol{\kappa}\}$ varies linearly in the element plane. During a deformation, when using the discrete Kirchhoff elements a linear variation of total strains in the mid-plane of the element is expected. The convergence rate of an element is determined by the order of its interpolating functions. This is based on the fundamental proposition of the finite element error analysis which states that for a sufficiently refined mesh, the error in a finite element solution can be bounded by the error in the shape function interpolation [121]. The sufficiently refined mesh is a mesh with which the true convergence rate is established. The convergence rate of an element in representing the rth derivative of a field quantity can be defined as $O(h^{p+1-r})$, where p is the degree of the highest complete polynomial in the element field quantity and h is the element length. For the discrete Kirchhoff shell element the rotations $\{\boldsymbol{\theta}\}$ are described by the complete quadratic polynomials [121]. Therefore, the convergence rate in the strain field is $O(h^2)$. This means that if the element size is halved, the error in the strain is reduced to approximately a quarter. Obviously, for higher order elements, which use higher order interpolating shape functions, the convergence rate will be higher.

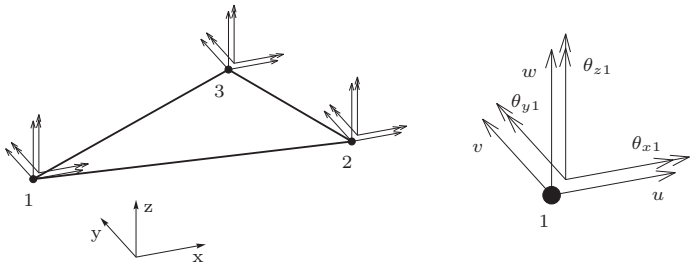

Figure 3.1: Discrete Kirchhoff triangular element with 18 degrees of freedom.

3.2 Blank discretisation

When a material is deformed in pure bending, there is a uniform distribution of stresses along its length in the plane of bending. Even a mesh which consists of 1 shell element can be sufficient for high accuracy. The situation changes when the material is bent over a tool radius and steep stress gradients appear in the blank. A coarse mesh used in the numerical analysis will not be able to accurately capture the localised high stresses. As a result, the accuracy of the stress state predicted by the finite element analysis and thus the accuracy of springback prediction will be questionable. To capture the localised stress gradients a sufficiently fine mesh must be used. Guidelines, defined below, can help in choosing the appropriate element size which can improve the prediction of springback by reducing the discretisation error. All simulations discussed in the text below are performed using the implicit finite element code DiekA.

3.2.1 Development of guidelines

The problem used to define guidelines at the level of blank discretisation with the discrete Kirchhoff triangular shell elements is shown in Figure 3.2. In this test a piece of sheet material is bent to a certain radius using a cylindrical die. The initial position of the strip and tool is shown in Figure 3.2(a). The material thickness is 0.8mm, its length is 16.0mm and the width is 5.0mm. The radius of the die is 10.0mm. Due to symmetry along AB and BC, only a quarter of the strip is used in the analysis. In addition to the boundary conditions of symmetry, all nodes along edge AD can only move in the $x-$direction. During forming the die is moved through a distance of 10.0mm in the positive $z-$direction (see Figure 3.2(b)).

Simulations of this test with uniform meshes of various density were performed. Characteristics of the meshes are provided in Table 3.1 where the number of elements along the line AB is given. The angle per element defines the degree of turning angle of the die radius between two adjacent nodes of the strip mesh. Discrete Kirchhoff triangular shell elements with 3 in-plane integration points and 7 points through the element thickness were used in this study. Simulations were performed with a dual phase steel (DP965) and its properties are presented in Table 3.2. The Hill'48 yield criterion with isotropic hardening was used to model the material

Table 3.1: Characteristics of meshes: guidelines development.

	Number of elements	Angle per element, [°]	Element length, [mm]
Mesh 1	5	18.0	3.1
Mesh 2	7	12.9	2.3
Mesh 3	8	11.3	2.0
Mesh 4	10	9.0	1.6
Mesh 5	13	6.9	1.2
Mesh 6	19	4.7	0.8
Mesh 7	40	2.4	0.4

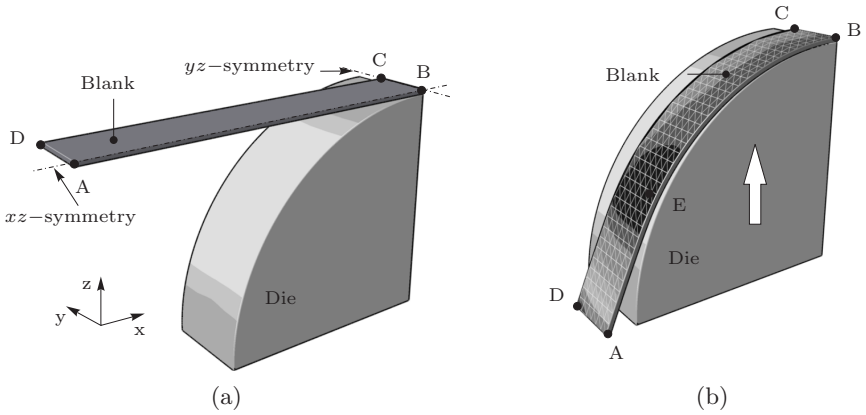

Figure 3.2: Diagram of the numerical set-up for single die bending: a) initial position and boundary conditions; b) shape of the strip after deformation.

behaviour. The stress-strain relation was represented using the Nadai hardening law: $\sigma = C(\varepsilon_0 + \varepsilon^p)^n$. The die was considered to be perfectly rigid and its surface was represented by analytical functions. The contact conditions between the strip and tools were described using the penalty method. To eliminate an influence of friction effects all simulations were performed with $\mu = 0$.

The accuracy of springback prediction is defined by the stress state obtained after forming. To quantify the accuracy of the stress state, the resulting bending moment is calculated in the region where the stress level is highest after the deformation. This region is depicted in Figure 3.2(b), which shows contours of tangential stresses σ_θ calculated for the lower layer of integration points. During each simulation, these stresses were recorded in a column of integration points of the element situated in the vicinity of point E. Values of the tangential stresses were used to calculate the resulting bending moment:

$$M_y = \frac{1}{2}\, t\, b \sum_{i=1}^{N_{ip}} w_i\, \sigma_\theta(\zeta_i)\, \zeta_i \tag{3.3}$$

where t is the material thickness; b is the strip width; N_{ip} is the number of through-

Table 3.2: Average material properties.

Material:	**DP965**	**DP600**	**AA5182**
Young's modulus, GPa	205	205	71
Poisson's ratio	0.3	0.3	0.33
YS, MPa	650.2	403.8	135.3
R_0, R_{45}, R_{90}	0.703, 0.742, 0.746	0.738, 0.897, 0.923	0.71, 0.58, 0.70
C-value, MPa	1484.8	1040.4	576.79
n-value	0.117	0.159	0.3593

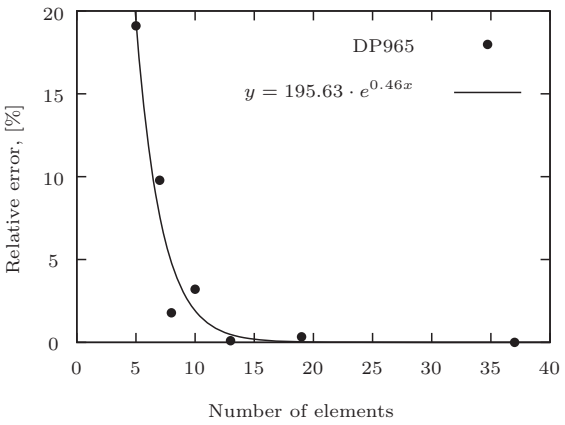

Figure 3.3: Variation of relative moment error depending on mesh density.

thickness integration points; w_i are weight factors; ζ_i are coordinates of the integration points and $\sigma_\theta(\zeta_i)$ are values of the tangential stresses in the sampling points. The bending moment obtained from a simulation with the finest mesh (mesh 7 in Table 3.1) was chosen to be the reference bending moment. A relative moment error was defined as the relative difference between the reference bending moment and the bending moment calculated in simulations with other mesh densities. Equation (2.35) shows that the bending moment M_y defines the change of shape during unloading in the plane of bending. Therefore, springback prediction error induced by the discretisation error is proportional to the relative moment error.

Results of the simulations are illustrated in Figure 3.3. The relative moment error is plotted versus the number of elements that are in contact with the die. In the range from 5 till 10 elements, a convergence rate of approximately $O(h^2)$ can be observed. Using more than 10 elements results in a relative error of less than 1%. The small oscillation of the results may be attributed to a slight mismatch in the position of the integration points in which the tangential stresses were recorded. Based on these results, it is concluded that about 10 elements over a tool radius are needed to create a mesh capable of describing in-plane stress distributions in the material. Summarising, the guideline for blank discretisation is to have a maximum turning angle of 9° per element to reduce the error in springback prediction to about 1%.

3.2.2 Validating the guidelines

The mesh density recommendation defined above are now applied in a springback analysis of the typical sheet metal forming products, namely the top-hat section test and the square cup drawing. The numerical analysis is performed in the implicit finite element code DiekA and the following characteristics remain unchanged in all simulations:

1) the materials defined in Table 3.2 are used. The Vegter yield criterion with isotropic hardening is used to model the aluminium alloy behaviour, whereas the behaviour of dual steels is described by the Hill'48 yield function with isotropic hardening. The stress-strain relation is represented using the Nadai hardening law;

2) blanks are discretised using discrete Kirchhoff triangular elements with 3 integration points in-plane and 7 integration points through the element thickness;

3) the tools are assumed to be perfectly rigid and are described by means of analytical surfaces. Contact conditions are described using the penalty method and the Coulomb friction model;

4) solution method: direct solver based on the Gauss elimination process.

Top-hat section

This problem resembles the U-shaped NUMISHEET'93 benchmark and its geometric parameters are shown in Figure 3.4(a). During forming, the material undergoes bending and subsequent unbending when travelling over the die shoulder. This results in a complex stress distribution through the thickness which causes formation of a curvature in the product wall during unloading, see Figure 3.4(c).

The amount of springback was quantified using the parameters θ_1, θ_2 and ρ, a definition of which can be found in [128]. Only a quarter of the blank was modelled in the analysis due to symmetry. Process parameters specified by the NUMISHEET'93 benchmark were used, i.e. the total blankholder force of 19.6kN and the friction coefficient of 0.162. Each simulation comprised two major steps: forming and springback. During the forming step the punch was moved in the negative $z-$direction with a total displacement of 85.0mm. The gradual tool release method, recommended

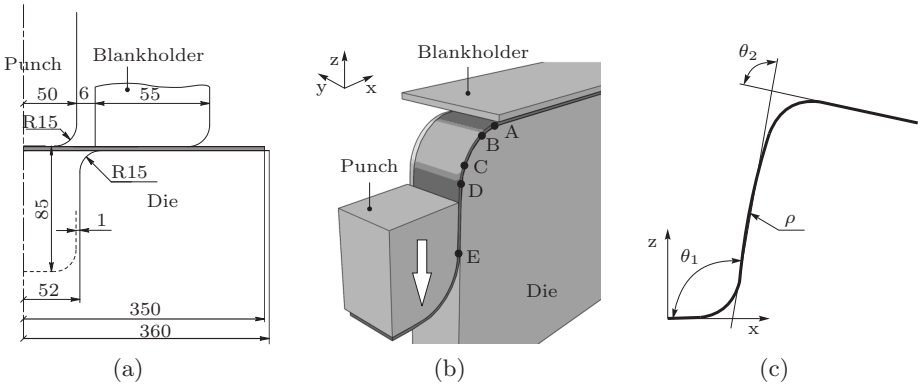

Figure 3.4: Top-hat section test: a) geometric parameters; b) deformation zones; c) parameters to quantify springback.

Table 3.3: Characteristics of meshes: guidelines validation.

Mesh name	Number of elements	Angle per element, [°]	Element length, [mm]
bm3	3	30.0	7.9
bm5	5	18.0	4.7
bm7	7	12.9	3.4
bm10	10	9.0	2.4
bm15	15	6.0	1.6
bm20	20	4.5	1.2
bm30	30	3.0	0.8

in Section 2.3.4, was employed to simulate the springback step. During the unloading the blankholder was moved up through a distance of 10.0mm and after that the die was moved 70.0mm down. The unloading procedure was finished with an instantaneous release of the tools. During this step, all contact forces were transformed into residual forces which were removed in three incremental steps. A set of simulations was performed in which the element size was varied. Characteristics of the uniform meshes used in the analysis are given in Table 3.3. In this table the number of elements in contact with the tool radius is indicated. Note that this number was used in the definition of the mesh name.

Results of simulations for the aluminium alloy (AA5182) are shown in Figure 3.5 where the blank shape after springback is plotted in the $xz-$symmetry plane. The amount of springback predicted in the simulations with very coarse meshes is significantly underestimated. Starting from 10 elements acros the tool radius (bm10), the discretisation error, although not completely eliminated, has a minor influence on the change of shape during unloading. Using more refined meshes leads to non-significant shape variations.

The simulations were compared to experimental observations from [69], to check the

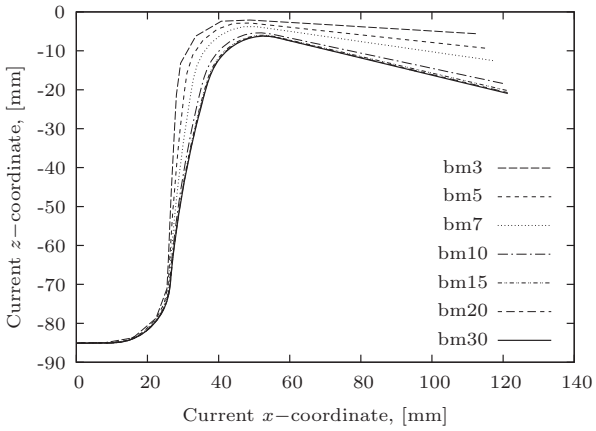

Figure 3.5: Final shape of the blank after springback.

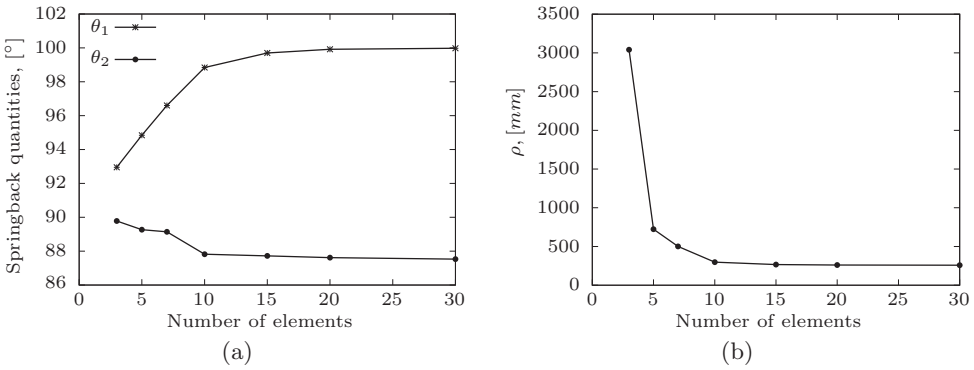

Figure 3.6: Influence of mesh sizes on springback: a) angles after unloading; b) radius in the blank wall.

validity of the numerical set-up. Experimental investigations of the test with a high strength steel showed that as the amount of springback increases, the curvature in the wall and the angle θ_1 increase, while angle θ_2 decreases. Its decrease can be explained by recalling the definition of this angle. Figure 3.4(c) shows that θ_2 is a function of the wall radius ρ. For an ideal case of no springback, the curvature in the wall is expected to be 0 (or $\rho = \infty$) and the angles θ_1 and θ_2 must be 90°. During the unloading, the wall radius decreases which causes a reduction in the angle θ_2. Evolution of the springback quantities θ_1, θ_2 and ρ with increasing mesh density is plotted in Figures 3.6(a) and 3.6(b). When looking at Figures 3.6(a) and 3.6(b) observations similar to the experimental observations can be made. The angle θ_1 and the wall curvature increase whereas the angle θ_2 decreases as more elements over the tool radius are used.

To find an explanation for the actual underestimation of springback when using the coarse meshes, some results of the simulations are considered. The punch force-displacement curves are shown in Figure 3.7. Results of the simulations with meshes bm15 and bm20 are not included since they coincide with the curve obtained from the simulation with the finest mesh. First, it is observed that the punch forces obtained in the analyses with coarse meshes (3, 5 and 7 elements over the tool radius) are higher. This can be explained by the fact that coarse meshes are less flexible since the number of degrees of freedom is not sufficient to represent all possible deformation modes. Second, the force-displacement curves of coarse meshes show oscillations which are caused by changing contact conditions in the regions of tools' radii. The variation of contact conditions is related to a finite number of nodes sliding over a tool radius and it becomes more pronounced with increasing element size.

Additional results of the simulations are discussed next. The thickness strain distribution in the $xz-$symmetry plane is plotted in Figure 3.8. The observed profile can be explained with the help of Figure 3.4(b). The sudden increase of the thickness strain at the distance of about 115.0mm can be explained by the blank entering the bending region of the die. In this region (from point A to B in figure 3.4(b)) the material is bent over the tool radius and the blank takes the die curvature. In

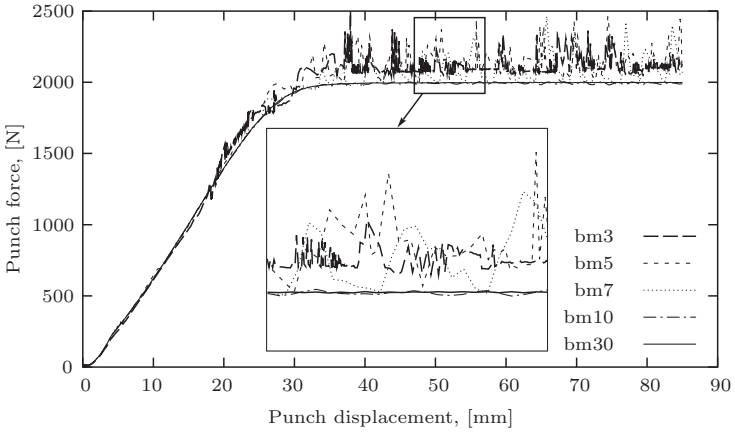

Figure 3.7: Force-displacement curves for various mesh densities.

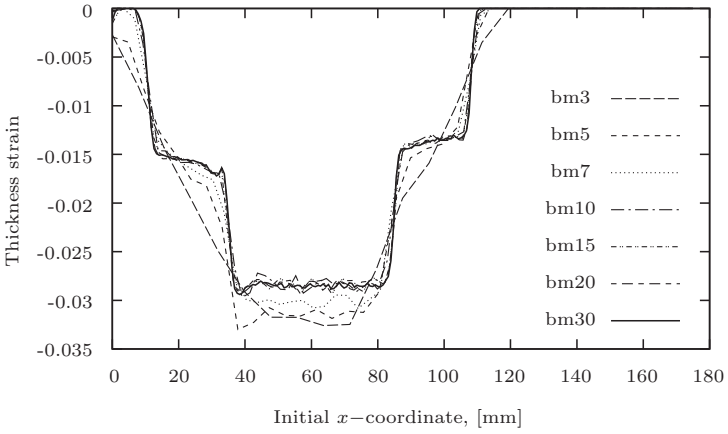

Figure 3.8: Thickness strain distribution in the $xz-$symmetry plane.

region $B - C$, the blank follows the constant die curvature and therefore the slight increase of the thickness strain till a distance of about 90.0mm is caused only by in-plane tension. Then the material is straightened in the unbending region $C - D$ which again results into an abrupt increase of the thickness strain. Having reached a certain level of hardening at the die radius the material experiences almost no additional deformation in the wall region $D - E$, which explains the constant level of the thickness strain from 80.0mm till 40.0mm. The plateau between 10.0 and 35.0mm is a result of bending and unbending deformation at the punch radius.

As shown in Figure 3.8, coarse meshes are not able to accurately capture the localised deformation which occurs in bending/unbending regions of tools radii. Furthermore, the higher value of the punch force results into more straining in the material, as can

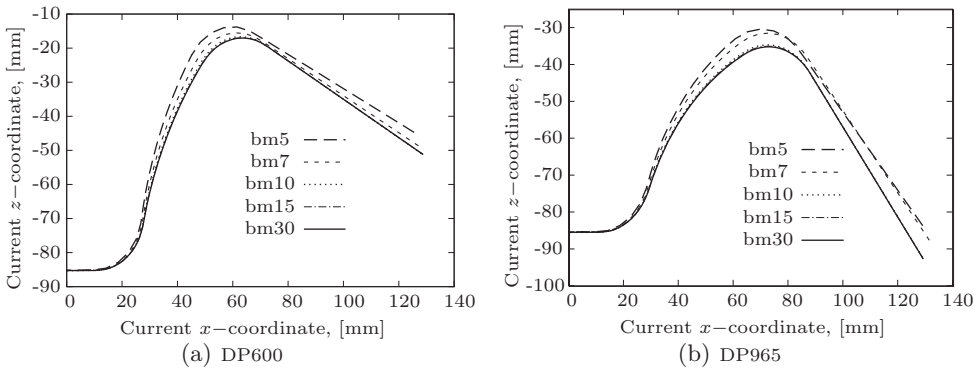

Figure 3.9: Results of simulations with different materials. Shape of the blank after springback.

be seen from the increased values of the thickness strain. This incorrect prediction of the material straining is the reason of the underestimation of the change of shape during unloading.

Additional simulations with two different materials DP600 and DP965 were performed using only the meshes bm5, bm10, bm15 and bm30. Blank shapes in the $xz-$symmetry plane obtained after the unloading procedure are plotted in Figure 3.9 for both materials. It can be seen that the shape predicted by the simulation with the mesh bm10 hardly differs from those obtained from the simulations with finer meshes. Note that the amount of springback increases for the dual phase steels. This can be explained by referring to Equation (2.38) which states that the amount of springback increases for materials with a higher $\sigma_{f(0)}/E$ ratio.

Square cup

The dimensions of the tools used in simulations of the square cup deep drawing are shown in Figure 3.10. Process parameters are summarised in Table 3.4. Only a quarter of the blank was used in the analysis due to symmetry. Simulations were performed with dual phase steel (DP600) and three different meshes, namely bm5, bm10 and bm15 (see Table 3.3). A realistic unloading procedure was imitated which included raising the punch through a distance of 10.0mm, lifting the blankholder through a distance of 2.0mm and sinking the die with a total displacement of 2.0mm and performing a subsequent instantaneous springback. Figure 3.11 shows the cross-sectional shape of the square cup after springback. The shape obtained from the

Table 3.4: Square cup deep drawing. Process parameters.

blank dimensions	150.0 × 150.0mm
material thickness	0.78mm
punch displacement	30.0mm
coefficient of friction	0.144
blankholder force	19.6kN

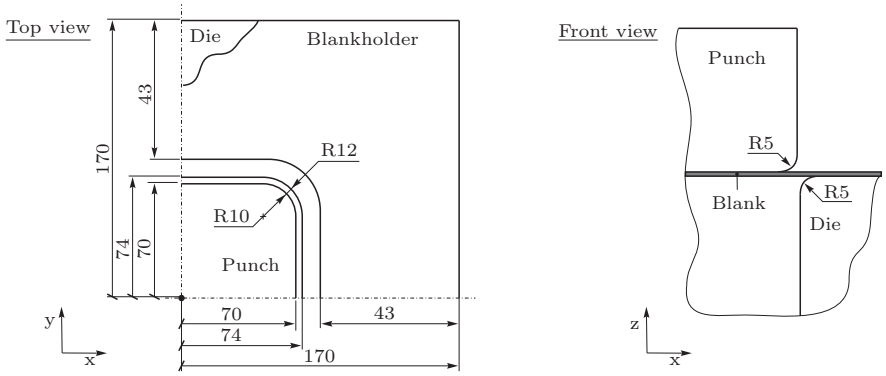

Figure 3.10: Square cup test. All dimensions are in millimeters.

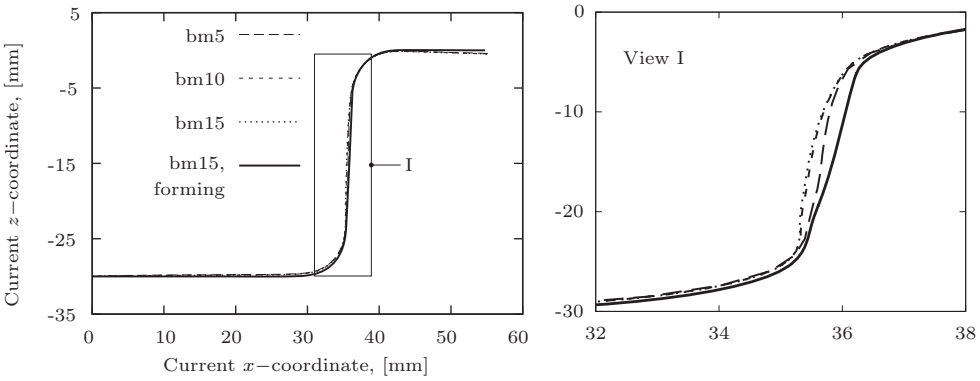

Figure 3.11: Shape of the blank after springback.

simulation with the finest mesh (15 elements over a tool radius) is considered as the reference. As can be seen, the analysis with the coarse mesh underestimates the curvature in the cup wall. In contrast, the mesh with 10 elements over a tool radius shows almost no deviations from the reference shape. In this problem, compared to the top-hat section test, shape deviations as a result of poor discretisation are less pronounced. This can be attributed to the decreased amount of springback during unloading. Section moduli of the square cup are much larger and, thus, its resistance to bending effects is higher.

Results of simulations of these tests show that the level of blank discretisation has a considerable influence on the accuracy of springback prediction. Discretisation of the blank is considered to be acceptable if 10 elements are in contact with the tool's radius. This mesh is sufficiently flexible and it gives accurate prediction of the change of shape during unloading.

3.3 Tool discretisation

In simulations of sheet metal forming it is common practice to assume that the tools are perfectly rigid. Consequently, only the outer surfaces are usually used to represent the tool geometry. Two different descriptions of the surfaces are possible: using analytical functions or a finite element mesh.

The analytical description offers the most accurate representation of the tool geometry. There is virtually no difference between the initial design and the geometry used in a numerical analysis. Simple analytical functions (for example planes, cylinders, spheres) or typical CAD surfaces can be used for this purpose. The analytical description offers another important advantage, it allows complete elimination of the tools' meshing step, which proves to be a very tedious and time-consuming task. In spite of the many difficulties relating to the data transfer between CAD software and finite element packages and the necessity of modifying contact search strategies, the analytical description of tools is increasingly used in simulations of sheet metal forming [129–132].

A mesh description of tools is the reliable and proven solution that is commonly used in practice. In this description, the tool surface is approximated by a mesh of undeformable finite elements. It is known that an insufficiently fine mesh used to describe the tool can lead to a deviation of the product shape obtained in the numerical analysis compared to that prescribed by the original design. A very coarse mesh can also deteriorate the convergence behaviour of a numerical solution. On the other hand, the number of elements forming the mesh cannot be too high since this may lead to a significant increase of the computation time needed by a contact search algorithm. In this section, guidelines are defined that prescribe the level of tool discretisation appropriate for an analysis of springback in sheet metal forming.

To avoid confusion, the elements that are used for blank and tool discretisation are called blank elements and tool elements correspondingly. To define the guidelines, simulations of the top-hat section test, shown in Figure 3.4(a), were performed. The aluminium alloy (AA5182) was used in the analysis and all parameters of the numerical set-up remain identical to those described in Section 3.2.2. Unless mentioned otherwise, the simulations were performed with the blank mesh bm15 (Table 3.3) to completely minimise the influence of blank discretisation. Tool meshes of various density were used in this study and their characteristics are presented in Table 3.5. The number of equilateral triangular elements along the curvature of a tool is given in this table.

Table 3.5: Characteristics of meshes used for tool discretisation.

Mesh name	Number of elements	Angle per element, [°]	Element length, [mm]
tm5	5	18.0	4.7
tm10	10	9.0	2.4
tm15	15	6.0	1.6
tm20	20	4.5	1.2
tm30	30	3.0	0.8

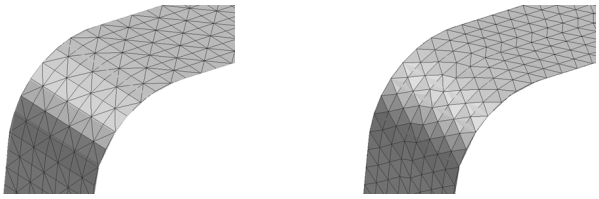

(a) Isomesh (b) Paved mesh

Figure 3.12: Tool description produced by various meshing methods.

It is known that when discretising the tools it is better to avoid using the type of mesh shown in Figure 3.12(a). Although simulation results are not influenced significantly, the convergence behaviour of the numerical analysis can be affected. Only the paved mesh, shown in Figure 3.12(b), is used in the subsequent analysis.

Force-displacement curves obtained in the simulations with various mesh densities are shown in Figure 3.13. If the number of tool elements is very low, the changes in the contact forces are severe, which results in a clearly visible force oscillation. The oscillation becomes smaller if the tools are described with an increased number of elements. In particular, the force-displacement curve of the simulation with 30 tool elements shows minor oscillation and the force value coincides with the force produced by the simulation with analytical tools. As can be seen in Figure 3.13, due to the very rough piece-wise representation of the tool curvature, the simulation with 5 tool elements overestimates the punch force, which increases the amount of tension in the product wall. Figure 3.14 shows the thickness strain distribution after forming in the $xz-$symmetry plane. Compared to the analytically-described tools, the thickness strain in the case of 5 tool elements is overestimated by almost 6%, whereas for 10 and more tool elements the results are almost identical. The influence of the increased tension in the product wall can be seen in Figure 3.15, where the product shape in

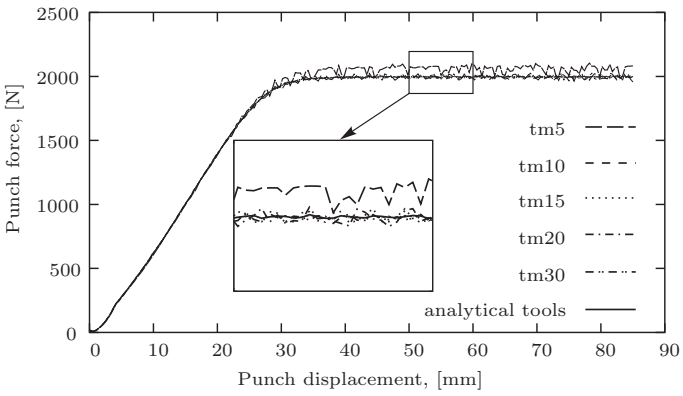

Figure 3.13: Force-displacement curves for different tool meshes.

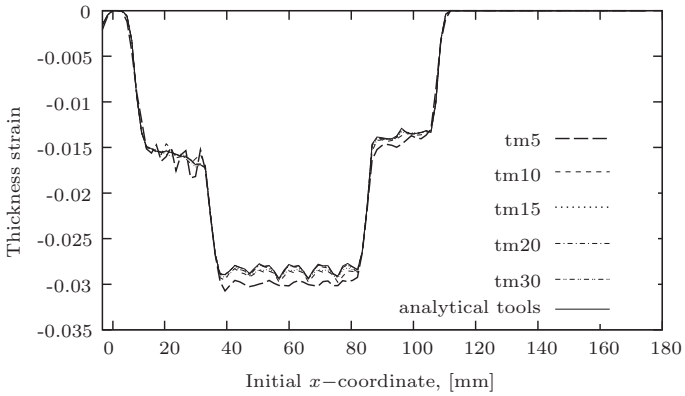

Figure 3.14: Thickness strain distribution (15 blank elements).

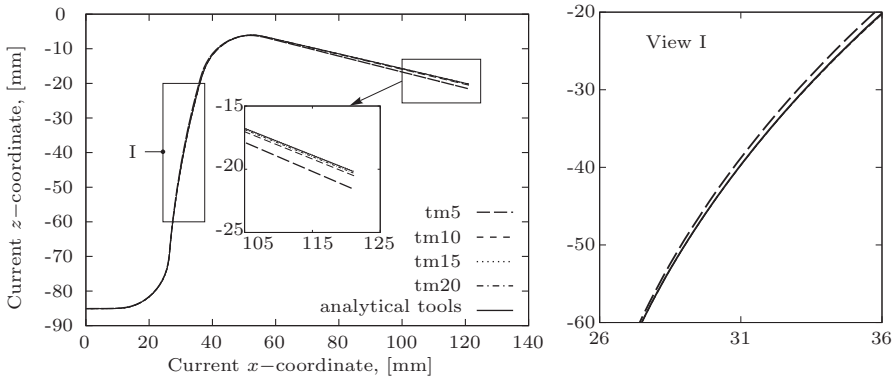

Figure 3.15: Product shape after springback (15 blank elements).

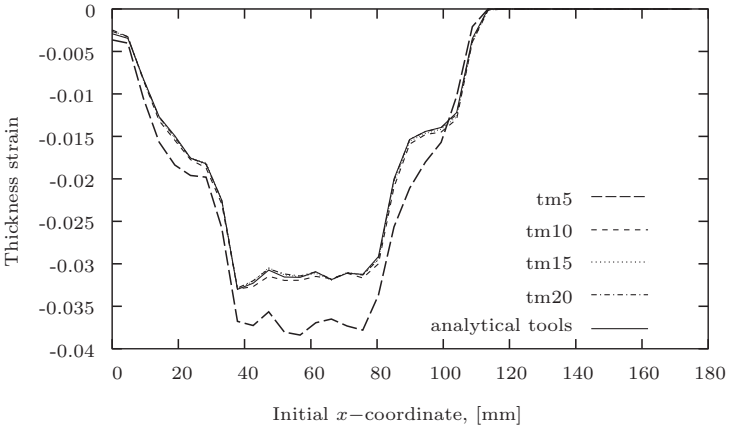

Figure 3.16: Thickness strain distribution (5 blank elements).

the $xz-$symmetry plane after springback is shown. For the case of 5 tool elements, due to the higher tension, shape deviations can be observed in the wall and flange regions. The deviation becomes even more pronounced when an insufficient number of elements is used to discretise the blank.

Several additional simulations were performed in which the blank mesh with 5 elements across the tool radius was used. Meshes 1-4 are used to describe the geometry of the tools. The thickness strain distributions in the $xz-$symmetry plane are shown in Figures 3.16. When the blank mesh is coarse, the increase in the strain in the product wall is significantly higher (about 18.5%). It is caused by the increased amount of in-plane tension at the tool radius. As can be seen in this figure, in the case of 5 tool elements the in-plane tension dominates in the bending/unbending region and the slope of the plateau increases significantly. Higher tension reduces the amount of product draw-in and leads to a significantly different shape of the blank after springback (see Figure 3.17).

Based on the simulations of the top-hat section test, with discretised tools, several important conclusions can be drawn. Very coarse meshes used to represent the tool surfaces reduce the accuracy. The spurious in-plane tension may change the draw-in amount and has a considerable influence on the product shape after springback. Coarse meshes of the tools also have a negative effect on the convergence behaviour of a simulation. Higher force oscillation destabilises the numerical solution process and may increase the total simulation time. To minimise the drawbacks of the tool discretisation about 10 elements are needed to describe the curved regions of a tool, 9° of turning angle per element. This level of discretisation gives an appropriate description of the tools' geometry and guarantees an accurate springback prediction.

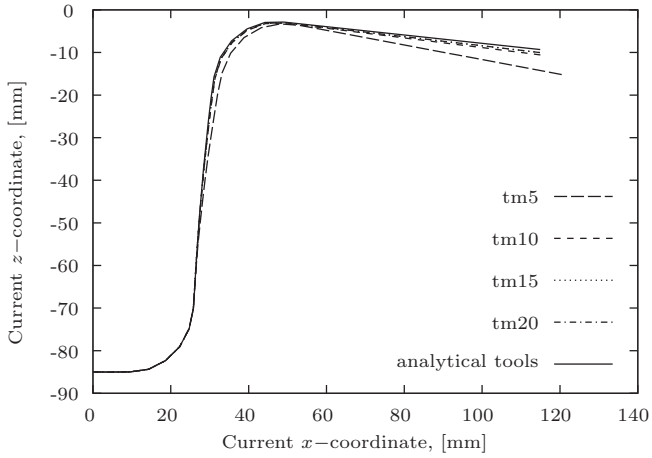

Figure 3.17: Product shape after springback (5 blank elements).

3.4 Concluding remarks

To improve the accuracy of stress state prediction in the end of forming, which governs the change of shape during unloading, the error due to the spatial discretisation must be minimised. This can be achieved by using sufficiently fine meshes to describe the blank and tools. The element size must be carefully chosen, since very fine meshes will lead to a drastic increase in computational costs.

Simulations of a single die bending test were used to define the level of blank discretisation which can accurately capture the high stress gradients that appear at the curved tool regions. When discretising the blank, one node per 9° of turning angle of the tool radius must be used to minimise the discretisation error. Springback simulations of the top-hat section test and square cup deep drawing showed that, when using the recommended mesh density in the analysis, the predicted shape of the part does not deviate significantly from that obtained in the reference simulation with a very fine mesh. It is important to note that the numerical study was performed using discrete Kirchhoff triangular shell elements. Therefore, the mesh density recommendation is applicable to situations when shell elements are used that have a similar order of interpolating functions. Due to higher convergence rates, higher-order elements will make it possible to guarantee an accurate springback prediction with less dense meshes.

A practical solution that can be employed in industrial simulations is to use the current recommendation in combination with adaptive mesh refinement. The main goal of adaptive refinement is to reach a required accuracy by using only as many degrees of freedom as absolutely necessary. It allows starting a simulation with a relatively coarse blank mesh. As the simulation progresses the blank mesh is refined, using the presented recommendation, at the places specified by the geometric error indicator. In this way a fine mesh will be used in the regions with high stress gradients and a coarser mesh in all other places. The refinement procedure can guarantee the improved accuracy of springback prediction at minimum cost.

If the forming tools are modelled with finite elements, an appropriate mesh density is required to minimise the negative effects of tool discretisation. Simulations of the top-hat section test showed that when meshing the tools, approximately one node per 9° of turning angle is required to describe curved regions. This level of discretisation minimises the punch force oscillation and does not introduce an additional in-plane tension which could affect the change of shape during unloading.

CHAPTER

FOUR

STRATEGY FOR ADAPTIVE THROUGH-THICKNESS INTEGRATION

In previous chapters it was shown that for a reliable simulation of springback, it is required to minimise the modelling and discretisation errors. Numerical integration through the thickness of shell elements is yet another reason for the low accuracy of springback prediction in sheet metal forming [17, 30, 133]. From the theory of FE analysis it is known that the characteristic matrices of a shell element are complex volume integrals. For example, the stiffness matrix of the discrete Kirchhoff shell element can be written as:

$$[\boldsymbol{k}] = \int_V [\boldsymbol{B}]^T [\boldsymbol{D}] [\boldsymbol{B}] \, dV = \int_A \int_{-\frac{t}{2}}^{\frac{t}{2}} [\boldsymbol{B}]^T [\boldsymbol{D}] [\boldsymbol{B}] \, dz \, dA \tag{4.1}$$

where $[\boldsymbol{B}]$ is the strain-displacement matrix; $[\boldsymbol{D}]$ is the matrix of material constants; V, A and t are correspondingly the volume, area and thickness of the shell. Both matrices $[\boldsymbol{B}]$ and $[\boldsymbol{D}]$ are not constant over the element, i.e. matrix $[\boldsymbol{B}]$ is a function of in-plane coordinates and matrix $[\boldsymbol{D}]$ varies in the element mid-plane and through its thickness. In general, it is not a trivial task to find the closed form solution of the integral in Equation (4.1) and for this reason the stiffness matrix and other characteristic matrices of the element are usually determined by means of numerical integration in the plane and in the thickness directions. The numerical integration includes multiplication of the integrand's value at the predefined locations within the element by weight factors and adding the results. The most widely used procedure for in-plane integration is Gauss quadrature. To decide on the number of Gauss points and to choose their most optimal location in the element plane one can use the recommendations provided in the literature [121, 134, 135].

To integrate through the thickness several integration schemes are commonly used, namely rules based on the Newton-Cotes formula, Gauss quadrature or the Lobatto rule. Each of these integration schemes has some advantages and a comparison of

their performance in plate and shell elements can be found in [136]. There is no clear recommendation for the number of through-thickness integration points that must be used to ensure accurate prediction of springback in sheet metal forming. As was discussed in Section 2.2.1, the through-thickness stress profile defines the internal bending moment which governs a change of shape during unloading. For a material in the elastic regime the through-thickness stress profile is smooth and the bending effects can be represented by a limited number of integration points. However, when the material undergoes plastic deformation the stress profile becomes non-smooth due to the presence of elastic-plastic transitions. In this case all traditional integration rules require a significant number of points to provide accurate stress resultants at the end of the deformation [133, 134, 136]. This number depends on the material, process parameters and the employed integration rule [133]. Increasing the number of through-thickness points in the numerical analysis places high demands on computational costs and is very undesirable.

To overcome this problem one may use the approach proposed by Simo et al. [137]. In this method a constitutive model is formulated directly in terms of stress resultants which allows the entire elimination of the through-thickness integration from a FE computational procedure. However, as mentioned by the authors themselves, the main disadvantage of this approach is that even the simplest yield criteria become very complex when expressed in terms of stress resultants.

A better option is to use an integration rule which can identify presence and location of the kinks and can adapt the position of available integration points depending on the stress profile. Such a scheme can guarantee more accurate stress resultants at the end of forming, and hence a more accurate springback prediction, while using a limited number of integration points. An adaptive through-thickness integration strategy for shell elements is developed and described in this chapter. The chapter starts with a short description of the traditional integration rules and a discussion of their limitations (Section 4.1). To be applicable in FE analyses, the adaptive strategy has to include several algorithms and their main tasks are described in Section 4.2. The potential of the adaptive integration is demonstrated using the simple plane strain bending problem (Section 4.3).

4.1 Traditional integration schemes

A short summary on the numerical schemes commonly used for the integration in the thickness direction of shell elements is given below. A full review of all possible integration strategies and detailed explanations of their underlying principles can be found in the literature, e.g. [120, 138].

4.1.1 Overview of available integration rules

In commercial FE packages the integration through the element thickness is usually performed with trapezoidal, Simpson's, Lobatto rules or Gauss quadrature. To explain the general idea underlying the numerical integration, suppose that $I(f) =$

$\int_a^b f(x)\,dx$ is an integral to be evaluated. Let $x_0, x_1, \ldots, x_n$ for $n \geq 1$ be a set of integration points that usually belong to the integration interval $[a, b]$. For the integrand $f(x)$ one can find an approximating function or a family of functions $f_n(x)$ and define [120]:

$$I_n(f) = \int_a^b f_n(x)\,dx \tag{4.2}$$

It is usually required that the approximations $f_n(x)$ satisfy:

$$||f - f_n||_\infty \to 0 \quad \text{with} \quad n \to \infty \tag{4.3}$$

and the form of $f_n(x)$ must be chosen such that $I_n(f)$ can be evaluated easily. Most integrals $I_n(f)$ after the evaluation will take the following form:

$$I_n(f) = \sum_{j=1}^{n} w_j\, f(x_j) \tag{4.4}$$

The coefficients w_j are the weights of $n + 1$ integration points.

Newton-Cotes integration

To define the Newton-Cotes formula a number of integration points $x_0, x_1, \ldots, x_n$ for $n \geq 1$, equally-spaced on the interval $[a, b]$, is chosen. A polynomial $P_n(x)$ is defined that approximates the integrand $f(x)$ at the integration points. The function $P_n(x)$ is usually defined using the Lagrange formula for an interpolating polynomial [120]:

$$\begin{aligned} P_n(x) &= \sum_{j=0}^{n} l_j(x) f(x_j)\,, \text{ where} \\ l_j(x) &= \prod_{i \neq j}^{n} \Big(\frac{x - x_i}{x_j - x_i} \Big), \quad \text{for } j = 0, 1, \ldots, n \end{aligned} \tag{4.5}$$

Analytically evaluating $I_n(f) = \int_a^b P_n(x)\,dx$ gives the equation for numerical integration with the Newton-Cotes formula:

$$I_n(f) = \int_a^b \sum_{j=0}^{n} l_j(x)\, f(x_j)\,dx = \sum_{j=0}^{n} w_j\, f(x_j) \tag{4.6}$$

where $w_j = \int_a^b l_j(x)\,dx$, for $j = 0, 1, \ldots, n$.

The Newton-Cotes formula provides a general framework for deriving several well-known integration rules. For example, with $n = 1$ it leads to the trapezoidal rule and with $n = 2$ to Simpson's rule. It is usually not recommended to use higher order integration formulae since they may not converge for well-behaved integrands [120].

Gauss quadrature

The trapezoidal and Simpson's rules use a fixed order polynomial to approximate the integrand $f(x)$. There is a class of integration methods that use polynomial approximations of $f(x)$ of increasing degree. A well-known representative of this class of methods is Gauss quadrature. In the case of Gauss quadrature, the problem of numerically calculating $I(f)$ is reduced to finding the location of the integration points x_j and the weight factors w_j which result in $I_n(f)$ being equal to $I(f)$ exactly for polynomials $f(x)$ of as high degree as possible [120]. Using Gauss quadrature with n integration points, a polynomial of degree $2n-1$ can be exactly integrated. For a large number of points, the parameters x_j and w_j can be calculated using the theory of orthogonal polynomials. A complete description of the theory and some computational procedures can be found in [120, 138, 139].

Lobatto rule

The Lobatto rule can be considered as a Gauss-type integration with two preassigned nodes [138]:

$$I_n(f) = a_1 f(a) + a_2 f(b) + \sum_{j=1}^{n} w_j \, f(x_j) \tag{4.7}$$

There are two integration points that are located at the limits of the integration interval $[a, b]$ and all other weight factors a_1, a_2, w_j and the locations x_j must be calculated. The algorithm to determine the weights and locations of the integration points of the Lobatto rule can be found in [140].

General remarks

The schemes based on the Newton-Cotes formula are simple to use, since calculation of the weights and locations of integration points is straightforward. However, in most of the cases the integration formulae of the Gauss type appear to be superior to the trapezoidal rule [120]. Furthermore, Gauss quadrature or the Lobatto rule are more preferable in situations where the function to be integrated is nonlinear and continuous in the interval $[a, b]$. The speed of convergence of these rules increases with increasing integrand smoothness [120, 138]. In contrast, the trapezoidal rule and Simpson's rule will not converge faster than a specific rate. The presence of integration points at the interval's limits may give extra advantages. If, during a numerical analysis, yielding of the material is initiated at the outer surface, the Lobatto and Newton-Cotes rules can directly identify it. For the same situation, the outermost Gauss integration point may still be in the elastic regime leading to less accurate results.

4.1.2 Limitations of traditional integration

In nonlinear FE analysis, when a material experiences plastic deformations, the through-thickness stress profile has discontinuous derivatives at the surfaces that

separate the elastic and plastic regions. The performance of various numerical schemes used for integration of plates and shells in this particular situation was investigated by Burgoyne and Crisfield [136]. Using four different problems they showed that none of the rules gives satisfactory accuracy when using less than 20 integration points. Nevertheless, Gauss quadrature was recommended as the most accurate one. It was additionally noted that, in some cases, it may be preferable to use a simpler integration strategy, such as the trapezoidal rule.

The influence of the through-thickness integration on the accuracy of springback prediction was studied extensively by Wagoner et al., [17, 133, 141]. Effects of varying material and process parameters on the error due to numerical integration were investigated by using a simple bending under tension model. It was shown that the error of springback analysis caused by the numerical integration oscillates with varying process parameters and the number of integration points. It was suggested that the error oscillation is related to changes in relative position of the integration points and the kinks in the stress profile.

To understand the origins of the numerical integration error and to explain its oscillatory behaviour, calculations of the plane strain bending problem shown in Figure 2.7 were performed. The underlying assumptions and a complete explanation of the problem was given in Section 2.2. A sheet material with a thickness of 1.0mm was deformed under combined bending and tension. The calculations were performed for an interstitial free steel (IF steel) with a Young's modulus of 210GPa, a yield stress of 150MPa and the Nadai hardening parameters C=425MPa and n=0.4. The bending moment M at the end of a deformation was found analytically and numerically. Equation (2.24) was used for the analytical calculations and the numerical value of the bending moment was found from the numerical integration formula, Equation (4.4). The numerical integration error is quantified by the relative difference between analytically and numerically calculated bending moments:

$$\text{RME} = \left| \frac{M_{num} - M_{analytical}}{M_{analytical}} \right| \cdot 100\% \tag{4.8}$$

where RME is the relative moment error. Note that, since the amount of springback is proportional to the bending moment (see Equation (2.38)), the error of springback prediction caused by the numerical integration is proportional to RME.

The first set of calculations was performed keeping the process parameters constant. The bending radius was 5.0mm and a tensile force was applied which shifted the neutral line by 0.4mm. Under these conditions the material underwent elastic-plastic deformation and a non-smooth stress profile, as shown in Figure 2.7(b), is expected through the thickness. Dependency of RME on the number of the integration points for the trapezoidal rule and the Gauss quadrature is shown in Figure 4.1. As expected, the Gauss quadrature performs better than the trapezoidal rule and converges faster to a zero value of the moment error. At the same time, due to the complexity and non-smoothness of the integrand ($\sigma_\theta \cdot z$), both rules lead to a high error when using $3-10$ integration points. It can also be seen that the moment error oscillates with a varying number of integration points.

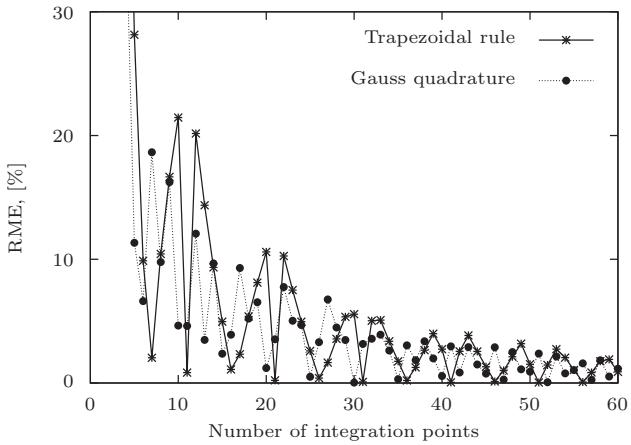

Figure 4.1: Relative moment error due to the numerical integration.

To demonstrate what happens to the integration error with changing process parameters, calculations with varying the R/t ratio and in-plane tension were performed. The moment error as a function of the in-plane tension for $R/t = 5$ is shown in Figure 4.2. The trapezoidal rule with 20 integration points was used in the calculations. The tension in this figure and all subsequent figures is represented by the normalised shift of the neutral line $\bar{a}$, which is defined as the neutral line shift divided by half of the sheet thickness, $\bar{a} = 2a/t$. As can be seen the error due to numerical integration oscillates and increases with increasing tension. The increase of the error can be explained by recalling the fact that the bending moment M decreases with increasing tension. Therefore, a given absolute moment error due to the numerical integration will lead to a larger relative error. At the same time, as shown in Figure 4.3, the integrand's profile becomes less smooth for higher values of tension, which increases the absolute moment error. Although it is not clearly visible

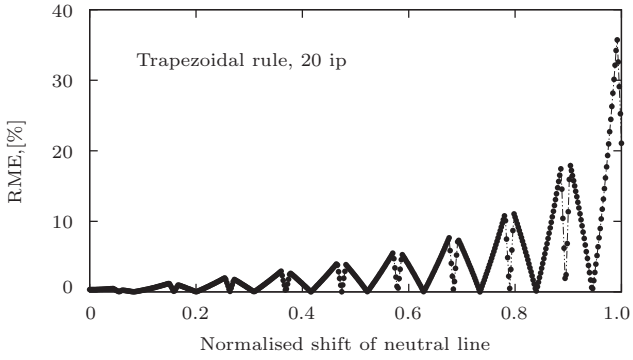

Figure 4.2: Influence of in-plane tension on the relative moment error.

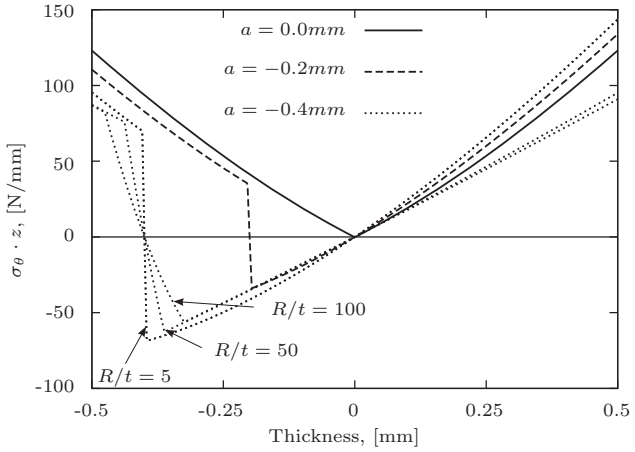

Figure 4.3: Integrand profiles for various R/t ratios and various values of tension indicated by the neutral line shift.

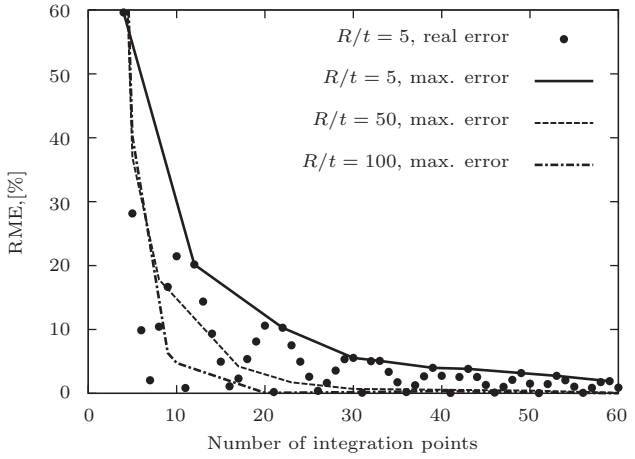

Figure 4.4: Influence of R/t ratio on the relative moment error.

in this figure, for the case of no tension (a =0.0mm) the integrand's distribution still contains two kinks that are located near the central line. As a result of bending to a small radius, the region with elastic material is very narrow and the elastic-plastic transitions are located very close to each other.

It is important to emphasise that the error oscillation makes it very difficult to develop practical guidelines for choosing the number of integration points which can ensure the accurate prediction of springback. For a particular problem, depending on process conditions a fixed number of integration points may lead to a high or a low error of prediction of stress resultants at the end of a deformation.

The influence of the R/t ratio on the integration error is shown in Figure 4.4. The

calculations were performed using the trapezoidal rule and the amount of tension was kept constant. Due to oscillation the term "maximum error" is introduced. It is an extreme value of RME for a given set of process conditions. Figure 4.4 shows that when the bending radius is small, the moment error is larger, and more integration points are needed to ensure a certain accuracy level. The observed increase of the RME for smaller bending radii can be explained with the help of Figure 4.3, where through-thickness profiles of the integrand are plotted for various R/t ratios. It can be seen that decreasing the bending radius causes the elastic region to shrink and the integrand's profile becomes less smooth.

Finally, to explain the error oscillation several calculations were performed with $R/t = 20$ and using different values of in-plane tension. The bending moments, calculated both analytically and numerically, are shown in Figure 4.5. The numerical calculations were performed using Gauss quadrature with 7 through-thickness integration points. The oscillation of the numerical bending moment is clearly visible and to explain its sudden steep decrease, five different values of tension (a, b, c, d and e) were considered. These values were used to calculate the profiles of the integrand shown in Figure 4.6. The through-thickness location of all seven integration points is indicated by the dashed lines. Additionally, two kinks in the integrand's profile are clearly distinguishable in this figure. These points define the places where the material transits from the elastic regime into the plastic regime. When the tension increases the kinks move with respect to the integration points. Before they reach the closest integration point (point 3 in Figure 4.6) the bending moment value decreases only slightly, since in the vicinity of every sampling point the integrand's profile undergoes only small modifications with changing process parameters. As soon as integration point 3 falls within the elastic region (profile b) its contribution to the bending moment value decreases abruptly and after this becomes negative. As a result the value of the bending moment drops sharply (see Figure 4.5). Soon after integration point 3 completely passes the elastic region (profile d), the moment value stabilises and

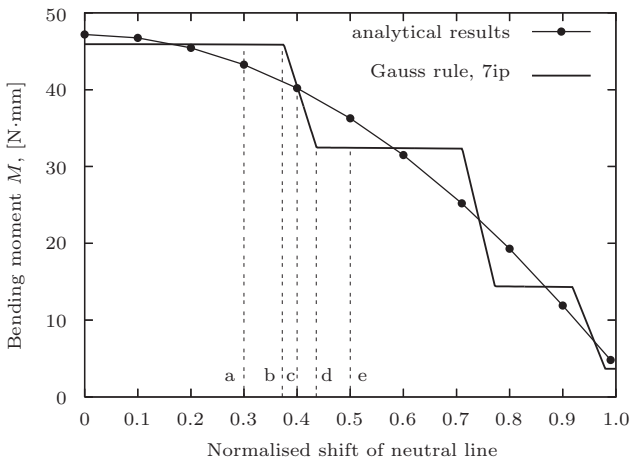

Figure 4.5: Variation of numerical and analytical bending moments with increasing tension.

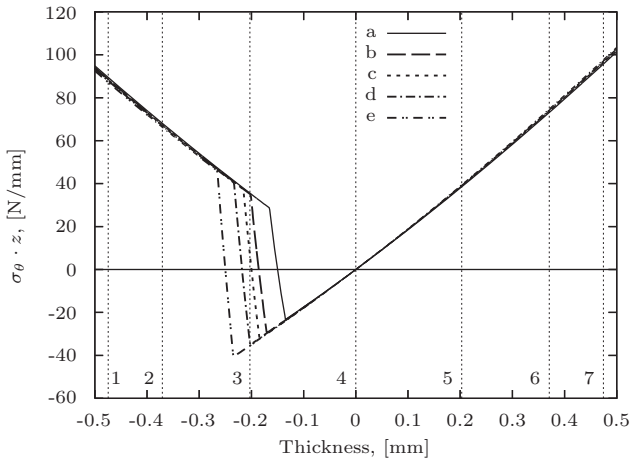

Figure 4.6: Integrand profile for different values of tension.

remains relatively constant until integration point 2 also falls within the elastic region.

It is clear that a numerical scheme that uses integration points which are fixed in the thickness direction is not so efficient in the numerical analysis of an elastic-plastic material [142, 143]. Both the trapezoidal rule and Gauss quadrature require a large number of integration points to give a negligible error of prediction of stress resultants. The error depends on the smoothness of the integrand profile and it increases with increasing tension or with bending to a smaller radius. The springback prediction error related to the numerical integration depends on the position of the integration points relative to the kinks and it oscillates if the kinks change their location with varying process parameters. For the traditional rules, the only way to minimise the difference between the analytical and numerical curves, shown in Figure 4.5, is by increasing the number of integration points. The oscillation then becomes more frequent but the accuracy of prediction of stress resultants becomes higher. In a realistic simulation of sheet metal forming the location and number of kinks in the stress profile is different in the various regions of the blank. Therefore, using the increased number of integration points in every element of the mesh is very unpractical and inexpedient. A good alternative to the traditional numerical schemes is an adaptive strategy that can identify the location of elastic-plastic transitions in the course of a simulation and, based on this information, can adapt the integration points to obtain the accurate solution at minimum cost. A procedure for such an integration strategy for shell elements is presented below.

4.2 Algorithms of adaptive integration

In this section an adaptive strategy for the through-thickness integration of shell elements is defined. The main distinctive feature of the strategy is the ability to

find an accurate numerical solution of an integral while using a limited number of integration points.

4.2.1 Outline of adaptive quadrature

All adaptive integration schemes can be classified as either iterative or noniterative [138]. In an iterative scheme, successive approximations to an integral are computed until the final result is satisfactory within a given tolerance. Several adaptive iterative algorithms have been developed, see for example [144–146], with the main goal to compute the integral value as accurately as possible with no strong restriction on the number of integration points used for that purpose.

In a noniterative scheme, prior to calculating the final integral value the integrand is evaluated to choose an optimum location and the number of integration points. This scheme, in contrast to the iterative one, is focused on finding the accurate integral value using a limited number of integration points. Therefore, it is the best candidate to be used for the through-thickness integration in shell elements.

The framework for constructing an adaptive integration scheme was suggested by Rice [144]. All possible components, that a numerical scheme may have, were summarised into a meta-algorithm for adaptive integration. Depending on the problem, specific components of the meta-algorithm can be chosen to build an adaptive integration strategy. Based on this framework, an adaptive noniterative integration strategy is defined. It consists of several components which are split between the interval manager and the interval processor (see Figure 4.7).

An adaptive integration strategy is developed for the implicit finite element solution procedure which is often employed for simulation of sheet metal forming and especially in a springback analysis. In the implicit procedure, state variables that satisfy the equilibrium at the end of a load increment are found iteratively by a Newton-Raphson method. Adapting the integration points during the iterative Newton-Raphson procedure will have an influence on the value of the internal force vector and therefore may result in a divergence of the solution process. To minimise the risk of divergence, the adaptation should take place after finding the converged solution at the end of a load increment. Then the interval manager of the adaptive strategy is called, kinks in the stress profile are located and the integration points are adapted to reduce the integration error. When an integration point is relocated or newly introduced, there is

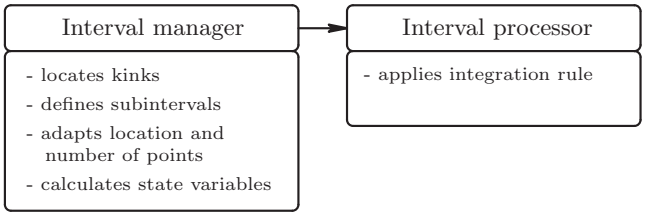

Figure 4.7: Block diagram of adaptive noniterative algorithm.

no history information available at that point. Therefore, the interval manager must include a component to calculate new values of internal variables, so that the deviation of the internal force vector after the adaptation from that obtained by the Newton-Raphson process is small. If unloading takes place during the next incremental step, the adapted integration points will guarantee more accurate stress resultants and hence - a more accurate springback prediction. If loading continues, the stiffness matrix is calculated and the iterative process is started to find state variables for the new load increment. All components of the interval manager and the interval processor are described in greater detail below.

4.2.2 Locating points of discontinuity

The interval manager evaluates the integrand prior to numerical integration. It includes several components and its first task is to locate kinks in the integrand's profile. When a material undergoes cyclic bending and unbending the through-thickness stress profile may contain several kinks. Figure 4.8 shows the fictive stress distribution which occurs in a beam after bending, reverse bending and repeated bending in the original direction. For simplicity, elastic, perfectly plastic material is chosen and in-plane tension is excluded. Due to symmetry, only half of the stress profiles is shown. While bending, as soon as yielding of the material is initiated, an elastic-plastic boundary or a point of discontinuity (POD1 in Figure 4.8) appears in the stress derivative. Having reached some given radius of bending the material is elastically unloaded and loaded in the reverse direction. For the elastic, perfectly plastic material, yielding in the reverse direction will start after reaching the initial yield stress value σ_{y1}. As a result, a new elastic-plastic transition or a point of discontinuity (POD2) is created. If the second elastic-plastic boundary does not propagate further than the first one, the stress profile contains two kinks. It can additionally be seen that lines $a-b$ and $c-d$ intersect the neutral axis at the yield

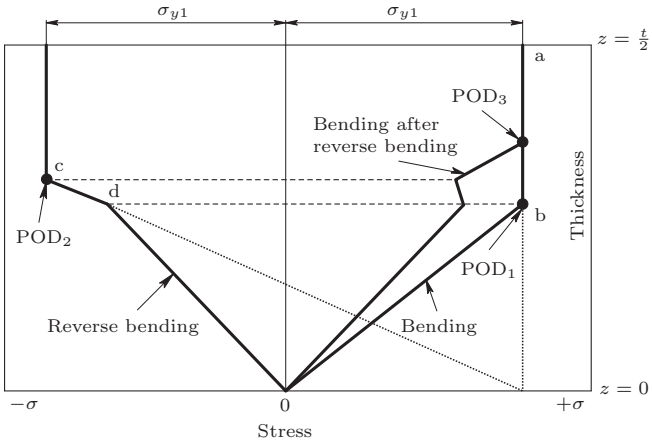

Figure 4.8: Kinks in the stress profile after cyclic bending without tension.

stress that is reached during the bending part of the cycle. This fact is explained in Appendix D where the equation that describes stress distribution during the unloading is derived. Unloading the beam from this situation and plastically loading it in the original direction produces a new point of discontinuity (POD3) (see Figure 4.8). In principle, for a high accuracy of integration the interval manager must include algorithms that are capable of locating all the stress profile kinks. The description of two of them which may be used for finding the location of the points of discontinuity POD1 and POD2 resulting from bending and reverse bending is given below.

To explain the algorithm for locating POD1, the problem shown in Figure 2.7 was considered. The typical distribution of the equivalent stress in a cross-section of the sheet for a material with arbitrary hardening is shown in Figure 4.9. For convenience, the stress distribution is plotted for the case of zero tension and only the upper part of the cross-section is shown. In this figure σ_{y1} is the initial yield stress and $\bar{\sigma}_1$ is the equivalent stress that occurs at the top layer during bending. Let z_1 and z_2 be the coordinates of elastic-plastic transitions POD1 with respect to the central line. Note that when the in-plane tension is applied, $z_1 \neq z_2$ due to the shift of the neutral line. To determine values of z_1 and z_2, the method proposed by Armen and Pifko [147] can be followed. The latter method is based on the von Mises yield criterion and allows location of the elastic-plastic transitions in beam and plate structures subjected to combined in-plane and lateral loading. Here, this method is developed further for application in planar anisotropic materials.

The vector of stresses for a material in the elastic region can be written using Hooke's law for plane stress:

$$\begin{Bmatrix} \sigma_{xx} \\ \sigma_{yy} \\ \tau_{xy} \end{Bmatrix} = \frac{E}{1-\nu^2} \begin{bmatrix} 1 & \nu & 0 \\ \nu & 1 & 0 \\ 0 & 0 & \frac{1-\nu}{2} \end{bmatrix} \begin{Bmatrix} \varepsilon_{xx} \\ \varepsilon_{yy} \\ \gamma_{xy} \end{Bmatrix} \quad \text{or} \quad \{\boldsymbol{\sigma}\} = \{\boldsymbol{E}\}\{\boldsymbol{\varepsilon}\} \tag{4.9}$$

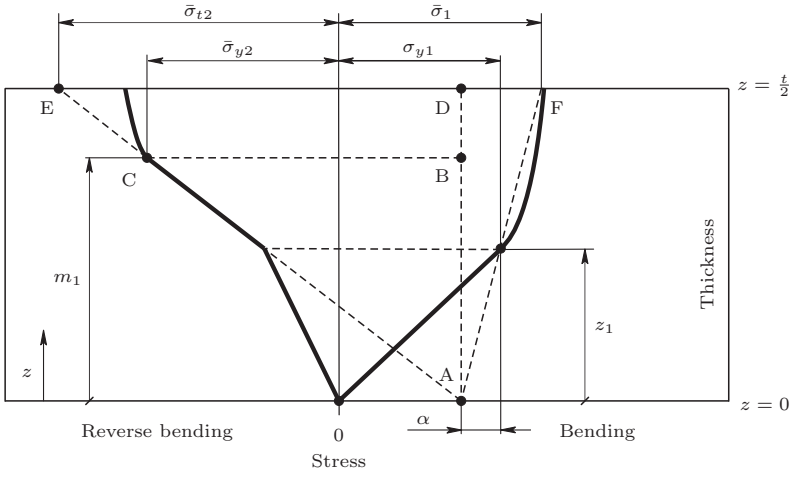

Figure 4.9: Equivalent stress profiles after bending and reverse bending.

Combining Equation (4.9) with Equation (3.2), it is possible to obtain the stress vector for a Kirchhoff plate in the elastic region:

$$\{\boldsymbol{\sigma}\} = \{\boldsymbol{E}\}\{\boldsymbol{\eta}\} - z \cdot \{\boldsymbol{E}\}\{\boldsymbol{\kappa}\} \quad \text{or} \quad \{\boldsymbol{\sigma}\} = \{\boldsymbol{A}\} - z \cdot \{\boldsymbol{B}\} \tag{4.10}$$

where $\{\boldsymbol{A}\}$ represents the contribution of the membrane part of the deformation and $\{\boldsymbol{B}\}$ represents the bending part. In the case of the small-strain formulation:

$$\{\boldsymbol{A}\} = \left\{ \begin{array}{c} A_{xx} \\ A_{yy} \\ A_{xy} \end{array} \right\} = \frac{E}{1-\nu^2} \left[\begin{array}{ccc} 1 & \nu & 0 \\ \nu & 1 & 0 \\ 0 & 0 & \frac{1-\nu}{2} \end{array} \right] \left\{ \begin{array}{c} u^{mp}_{,x} \\ v^{mp}_{,y} \\ u^{mp}_{,y} + v^{mp}_{,x} \end{array} \right\} \tag{4.11}$$

$$\{\boldsymbol{B}\} = \left\{ \begin{array}{c} B_{xx} \\ B_{yy} \\ B_{xy} \end{array} \right\} = \frac{E}{1-\nu^2} \left[\begin{array}{ccc} 1 & \nu & 0 \\ \nu & 1 & 0 \\ 0 & 0 & \frac{1-\nu}{2} \end{array} \right] \left\{ \begin{array}{c} w^{mp}_{,xx} \\ w^{mp}_{,yy} \\ 2w^{mp}_{,xy} \end{array} \right\} \tag{4.12}$$

It is known that a material remains elastic through its thickness until the yield condition is satisfied. The plane stress Hill'48 yield criterion is used to model anisotropic material behaviour:

$$F\sigma_y^2 + G\sigma_x^2 + H(\sigma_x - \sigma_y)^2 + 2N\sigma_{xy}^2 - \frac{2}{3}(F+G+H)\sigma_{yield}^2 = 0 \tag{4.13}$$

where σ_{yield} is the stress at yield and the parameters F, G, H and N describe the material anisotropy. These parameters can be defined as functions of the planar anisotropy parameters R_0, R_{45} and R_{90} [12].

Substituting the components of the stress vector (Equation (4.10)) into the last equation and gathering the terms gives:

$$\begin{aligned} &\left((G+H)B_{xx}^2 + (F+H)B_{yy}^2 - 2HB_{xx}B_{yy} + 2NB_{xy}^2\right) \cdot z^2 + \\ &\left(2H(A_{yy}B_{xx} + A_{xx}B_{yy}) - 2(G+H)A_{xx}B_{xx} - \right. \\ &\left. 2(F+H)A_{yy}B_{yy} - 4NA_{xy}B_{xy}\right) \cdot z + (G+H)A_{xx}^2 + (F+H)A_{yy}^2 - \\ &2HA_{xx}A_{yy} + 2NA_{xy}^2 - \frac{2}{3}(F+G+H)\sigma_{yield}^2 = 0 \end{aligned} \tag{4.14}$$

or in a more convenient form:

$$a_1 z^2 + a_2 z + a_3 - \frac{2}{3}(F+G+H)\sigma_{yield}^2 = 0 \tag{4.15}$$

Solving this quadratic equation gives two roots z_1 and z_2 which define the location of the elastic-plastic transitions during bending under tension. As can be seen, to locate the transition points the algorithm uses the membrane and bending components of the total strain vector. In the FE analysis based on the large-deformation plasticity these components can be easily calculated and made available at the end of each incremental step. If, for example, Kirchhoff shell elements are used to describe the sheet, then by using Equation (4.15) at each column of integration points of every

element in the mesh, the interval manager can always track the location of POD1 during the analysis.

The location of the POD2 kink can be determined using a graphical approach described in [147]. Figure 4.9 shows a typical distribution of the equivalent stress in the same cross-section after bending in the reverse direction. $\bar{\sigma}_{t2}$ is the equivalent trial stress that would exist if the material did not have plastic deformations in reverse loading and, if the hardening is isotropic, $\bar{\sigma}_{y2}$ is the equivalent stress reached in earlier plastic straining. The location of the upper POD2 kink can be calculated from the similar triangles ABC and ADE:

$$m_1 = \frac{\bar{\sigma}_{y2} + \sigma_{y1} - \alpha}{\bar{\sigma}_{t2} + \sigma_{y1} - \alpha} \cdot \frac{t}{2} \tag{4.16}$$

where α defines the point at which the equivalent elastic stress distribution intersects the neutral line during the reverse bending:

$$\alpha = \frac{\bar{\sigma}_1 - \sigma_{y1}}{\frac{t}{2} - z_1} \cdot z_1 \tag{4.17}$$

As explained in Appendix D, this point coincides with the point of intersection of the neutral line and the line $A - F$.

In contrast to the POD1 algorithm, the method for locating the POD2 kink has some limitations and cannot be generally applied. Firstly, the linear hardening assumption, which is required to calculate the value of α, may introduce some error. Secondly, this method is only applicable in situations when the material undergoes cyclic bending without tension. In realistic loading conditions, the in-plane tension may have a significant effect on the shape of the through-thickness stress distribution. To visualise this, two simulations of the top-hat section test, shown in Figure 3.4(b), were performed. The aluminium alloy AA5182 was used in the simulations and its properties are summarised in Table 3.2. The thickness of the blank was 0.81mm and a description of the process parameters is provided in Section 3.2.2. To describe the blank, discrete Kirchhoff triangular elements were used with 30 Gauss points through the thickness. The tools were described by means of analytical surfaces. Two simulations were performed to define the effect of tension on the through-thickness stress profiles, i.e. with friction and without friction. An element of the blank that passes the die radius completely during forming is tracked. For one specific column of integration points of this element the circumferential stress σ_{xx} is recorded at the moment when: the element is in the bending region (region AB in Figure 3.4(b)); the element is in the region of constant die curvature (region BC) and the element is in the unbending region (region CD).

The stress profiles obtained from both simulations are shown in Figure 4.10. The distribution of stresses obtained from the simulation without friction is comparable to that assumed in the algorithm for locating kink POD2 (see Figure 4.9). However, the simulation with friction shows that the influence of tension is two-fold: it causes a shift of the neutral line and it completely modifies the shape of the through-thickness stress profiles, so that it becomes impossible to locate kink POD2 on the basis of

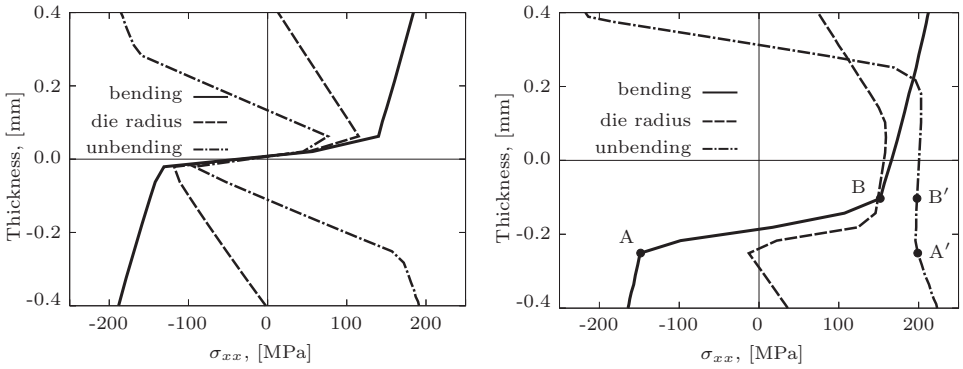

(a) without friction (b) with friction

Figure 4.10: Through-thickness stress distributions in the element that completely passes the die radius.

geometric considerations alone. It can additionally be seen that at the onset of yielding, the POD1 kinks (points A and B in Figure 4.10(b)) are both located in the plastic region and are less pronounced. Apparently, there is a need for a generally applicable algorithm of the interval manager that can locate kinks in stress profiles obtained from an arbitrary loading scenario. Such an algorithm is developed and validated in Chapter 5.

4.2.3 Relocating integration points

The interval manager divides the complete integration interval $[-t/2, t/2]$ into several parts as soon as the kinks in the stress profile are found. The subdivision is done in such a way that the endpoints of the subintervals coincide with the kinks, and hence the integrand at every subinterval is a continuous function. Integration points are rearranged so that there are several points inside every subinterval and two of the points are located at its limits. If required, the location and number of the integration points within each subinterval can be adapted depending on the numerical integration scheme used and the smoothness of the integrand. Applying an integration rule to every subinterval and adding the results gives the numerical value of the integral.

4.2.4 Updating internal variables

State variables must be available at each integration point and updated as the incremental-iterative solution procedure progresses. A newly introduced or relocated integration point does not contain any information about previous loading at this particular location and its internal variables must be calculated. For the integration points relocated in the elastic region, this can be accurately done by linear interpolation using the information at e.g. their old locations. The algorithm

to update internal variables of the integration points in the plastic region is more complex.

When using the Hill'48 yield criterion with isotropic hardening the state variables that must be updated are the stress vector $\boldsymbol{\sigma}$ and the accumulated equivalent plastic strain $\bar{\varepsilon}^p$. Let $\{\boldsymbol{\sigma}\}_1$, $\{\boldsymbol{\sigma}\}_2$, $\bar{\varepsilon}_1^p$ and $\bar{\varepsilon}_2^p$ be the stress vectors and the accumulated equivalent plastic strains at the integration points belonging to the same plastic region, and these will provide information for the variables update. The main goal now is to determine the stress vector $\{\boldsymbol{\sigma}\}_3$ and the accumulated equivalent plastic strain $\bar{\varepsilon}_3^p$ at the new integration point, labelled 3. The assumption of linearly varying strains through the thickness of the shells makes it possible to calculate the accumulated equivalent plastic strain $\bar{\varepsilon}_3^p$ by simple interpolation. From the Lagrange formula for an interpolating polynomial (see Equation (4.5)):

$$\bar{\varepsilon}_3^p = \frac{z_3 - z_2}{z_1 - z_2}\bar{\varepsilon}_1^p + \frac{z_3 - z_1}{z_2 - z_1}\bar{\varepsilon}_2^p \tag{4.18}$$

where z_1, z_2 and z_3 are the through-thickness coordinates of the integration points.

To update the stress state the following procedure can be used, based on [134, 148, 149]. At first, the flow stress at the new integration point 3 is calculated by using, for example, the Nadai hardening relation:

$$\sigma_{f3} = C\big(\bar{\varepsilon}_3^p\big)^n \tag{4.19}$$

with C and n being the material hardening parameters. Then the new stress vector $\{\boldsymbol{\sigma}\}_3^{int}$ is calculated by simple interpolation of the stress state from the fixed integration points:

$$\{\boldsymbol{\sigma}\}_3^{int} = f\big(\{\boldsymbol{\sigma}\}_1, \{\boldsymbol{\sigma}\}_2\big) \tag{4.20}$$

Generally, the interpolated stress vector will not satisfy the yield condition and therefore a scaling factor q is introduced to correct the stress state at the new integration point [148]:

$$q = \frac{\sigma_{f3}}{\bar{\sigma}_3^{int}} \tag{4.21}$$

where $\bar{\sigma}_3^{int}$ is the equivalent stress after the interpolation. Using the scaling factor it is now possible to find the approximate stress state that must exist at the new location:

$$\{\boldsymbol{\sigma}\}_3 = q \cdot \{\boldsymbol{\sigma}\}_3^{int} \tag{4.22}$$

The presented procedure provides an example of how to update state variables of integrations points at a new location. To be applicable in the numerical analysis with more advanced constitutive models that use additional hardening variables, the algorithm must be extended. The extension depends on the type of hardening parameters and their evolution equations.

4.2.5 Applying the integration rule

The interval processor performs the actual integration. After adaptation the integration points will not be equally spaced, and thus a numerical scheme is needed

that is capable of performing integration using unequally distributed points. The idea behind integration with unequally spaced points is similar to that of Newton-Cotes integration. Initially, a number of integration points $x_0, x_1, \ldots, x_n$ for $n \geq 1$, unequally spaced on the interval $[a, b]$, is chosen with $f(x_0), f(x_1), \ldots, f(x_n)$ being their corresponding integrand values. An interpolating function $P(x)$ is defined that approximates the integrand $f(x)$ at the integration points. Various functions can be used for the approximation, for example a polynomial or a spline. Using the second order polynomial gives Simpson's formula for integration with unequally spaced points:

$$I_n(f) = \sum_{j=1}^{n/2} \Big(\frac{k_j}{3}(x_{2j}^3 - x_{2j-2}^3) + \frac{l_j}{2}(x_{2j}^2 - x_{2j-2}^2) + m_j(x_{2j} - x_{2j-2}) \Big) \quad \text{for} \quad j = 1, 2, ..., n/2 \tag{4.23}$$

where k_j, l_j and m_j are coefficients of a quadratic polynomial defined using three consecutive integration points:

$$k_j = \frac{f(x_{2j-2})}{(x_{2j-2} - x_{2j-1})(x_{2j-2} - x_{2j})} + \frac{f(x_{2j-1})}{(x_{2j-2} - x_{2j-1})(x_{2j} - x_{2j-1})} + + \frac{f(x_{2j})}{(x_{2j-2} - x_{2j})(x_{2j-1} - x_{2j})} \tag{4.24}$$

$$l_j = -\frac{(x_{2j-1} + x_{2j})f(x_{2j-2})}{(x_{2j-2} - x_{2j-1})(x_{2j-2} - x_{2j})} - \frac{(x_{2j-2} + x_{2j})f(x_{2j-1})}{(x_{2j-2} - x_{2j-1})(x_{2j} - x_{2j-1})} - - \frac{(x_{2j-2} + x_{2j-1})f(x_{2j})}{(x_{2j-2} - x_{2j})(x_{2j-1} - x_{2j})} \tag{4.25}$$

$$m_j = \frac{x_{2j-1}\, x_{2j}\, f(x_{2j-2})}{(x_{2j-2} - x_{2j-1})(x_{2j-2} - x_{2j})} + \frac{x_{2j-2}\, x_{2j}\, f(x_{2j-1})}{(x_{2j-2} - x_{2j-1})(x_{2j+2} - x_{2j-1})} + + \frac{x_{2j-2}\, x_{2j-1}\, f(x_{2j})}{(x_{2j-2} - x_{2j})(x_{2j-1} - x_{2j})} \quad \text{for} \quad j = 1, 2, ..., n/2 \tag{4.26}$$

When using a FE solution procedure it is more convenient to have an array which contains the weights of the integration points. To update this array when the location of the integration points changes, the following equations can be used:

$$w_{2j-2} = w_{2j-2} + \frac{1}{(x_{2j-2} - x_{2j-1})(x_{2j-2} - x_{2j})} \times \times \Big(\frac{x_{2j}^3 - x_{2j-2}^3}{3} - (x_{2j-1} + x_{2j}) \frac{x_{2j}^2 - x_{2j-2}^2}{2} + x_{2j-1}\, x_{2j}(x_{2j} - x_{2j-2}) \Big)$$

$$
\begin{aligned}
w_{2j-1} &= \frac{1}{(x_{2j-1}-x_{2j-2})(x_{2j-1}-x_{2j})} \times \\
&\times \left(\frac{x_{2j}^3 - x_{2j-2}^3}{3} - (x_{2j-2}+x_{2j}) \frac{x_{2j}^2 - x_{2j-2}^2}{2} + x_{2j-2}\, x_{2j} (x_{2j} - x_{2j-2}) \right) \\
w_{2j} &= \frac{1}{(x_{2j}-x_{2j-2})(x_{2j}-x_{2j-1})} \times \\
&\times \left(\frac{x_{2j}^3 - x_{2j-2}^3}{3} - (x_{2j-2}+x_{2j-1}) \frac{x_{2j}^2 - x_{2j-2}^2}{2} + \right. \\
&+ \left. x_{2j-2}\, x_{2j-1} (x_{2j} - x_{2j-2}) \right)
\end{aligned}
$$

$$\text{for} \quad j = 1, 2, ..., n/2 \tag{4.27}$$

The complete derivation of Equations (4.23) and (4.27) is provided in Appendix E. Following the strategy presented there, the formula for the trapezoidal integration can easily be obtained. The equation for the spline integration with unequally spaced points can also be found in Appendix E.

Each of the considered integration rules places specific demands on the interval manager that are related to a minimum number of integration points required at each subinterval and their location. For example, the adaptive Simpson's and spline rules require at least three points within every subinterval. As for the adaptive trapezoidal rule, due to the lower order polynomial used for the interpolation, more points must be placed at highly curved regions of the integrand's profile to reduce the integration error. Gauss quadrature and the Lobatto rule are left out of consideration here since they do not allow an arbitrary placement of integration points.

4.3 Potential of adaptive integration

To demonstrate the potential of adaptive integration in springback analysis, the plane strain bending and stretching problem shown in Figure 2.7 is considered. The moment M resulting from bending of a sheet to a radius under in-plane tension was calculated from Equation (2.24). The material of the sheet was IF steel, its thickness was 1.0mm and the radius of bending was 5.0mm. The adaptive strategy outlined above was used to define an adaptive integration rule specifically adjusted for this problem. The interval manager of the adaptive rule performs the following tasks:

1) locates two elastic-plastic transitions (POD1) in the stress profile using Equations (2.14) and (2.17);

2) divides the complete integration interval $[-\frac{t}{2}, \frac{t}{2}]$ into three subintervals AB, BC and CD that are shown in Figure 2.7(b);

3) adapts the location and number of the integration points within each subinterval. The specific demands of the integration rule employed are considered here. As a reminder: the adaptive Simpson's rule and the spline rule

require at least three integration points at every subinterval. If necessary, the number of the integration points may change as a function of the subinterval's length. For this specific problem the subinterval AB decreases in size with increasing tension, therefore it is logical to move excessive integration points to subinterval CD which then increases in size.

To perform the actual integration the interval processor employs Simpson's rule and the rule based on the spline approximation of the integrand. The bending moment M was calculated using the adaptive Simpson's scheme with 7 integration points in total, the adaptive spline scheme with 11 points and the traditional trapezoidal rule with 50 points. The calculations were performed for a range of values of tension. The influence of the numerical integration on the amount of springback was again quantified by finding the relative difference between the numerical and analytical bending moments.

Results of the calculations are shown in Figure 4.11 where RME is plotted as a function of tension. The traditional trapezoidal rule requires a very large number of points to keep the integration error low. Additionally, by comparing Figures 4.2 and 4.11 one can note that the error oscillation becomes more frequent when using more integration points. At the same time, it can be seen that the adaptive integration strategy has a great potential. Compared to the traditional rule, an almost negligible integration error is obtained while using a very small number of points. By tracing the location of the points of discontinuity, the error oscillation can be avoided and as a result, the integration error increases smoothly with increasing the tension. Absence of error oscillation makes it easier to choose a number of integration points that can guarantee a specific accuracy of springback prediction.

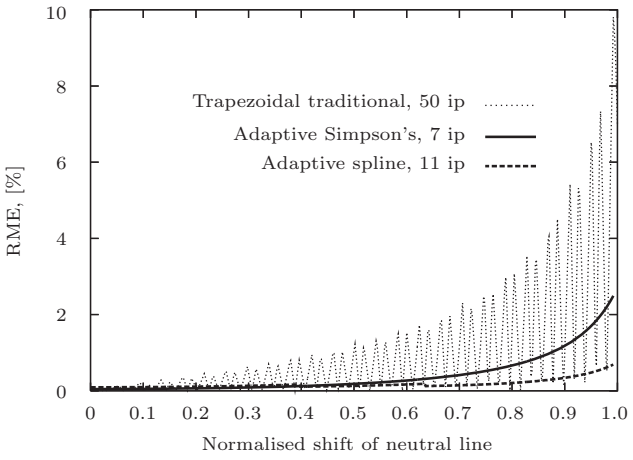

Figure 4.11: Relative moment error for various values of in-plane tension.

4.4 Concluding remarks

Traditional numerical schemes for through-thickness integration in shell elements are inefficient in elastic-plastic analysis. They show error oscillation and require a very large number of integration points to ensure a certain accuracy of springback prediction. The adaptive integration strategy, described in this chapter, can be used to define a numerical scheme that uses the integration points more efficiently. An adaptive integration scheme must include several algorithms that evaluate the through-thickness stress profile, adapt the location and the number of integration points, and perform the actual integration.

The potential of the adaptive integration was demonstrated using the bending with tension problem. Calculations showed that for a similar set of material and process parameters the adaptive Simpson's scheme with 7 points and adaptive spline scheme with 11 points perform significantly better than the traditional trapezoidal rule with 50 integration points. Compared to the traditional schemes, the adaptive strategy uses the integration points more efficiently and can guarantee accurate springback prediction at minimum cost.

To make the adaptive strategy generally applicable, some components of the interval manager must be modified. A new algorithm will be developed that can locate the stress profile kinks which occur in arbitrary loading conditions (see Chapter 5).

CHAPTER

FIVE

APPLICATION OF ADAPTIVE INTEGRATION IN SPRINGBACK ANALYSIS

In this chapter the advantages to be gained when using the adaptive integration in the analysis of springback in sheet metal forming are demonstrated. Based on the theory presented in the previous chapter an adaptive integration scheme is formulated and implemented in the implicit FE code DiekA. Its performance is evaluated with the help of two numerical examples in which the material is deformed in the bending dominated regime. In section 5.1 simulations of a simple academic problem and the characteristic component 1 (shown in Figure 2.9) are performed using the adaptive integration scheme and several traditional rules. Effects of varying some process parameters and the number of through-thickness integration points are investigated. To make the strategy for adaptive integration suitable in simulations of realistic deep drawing problems a more advanced algorithm that locates stress profile kinks is developed in Section 5.2. This algorithm can determine the location of elastic-plastic transitions which appear when a material is bent and unbent under tension. It is independent of the yield function used in the numerical analysis and forms the basis of the generally applicable adaptive integration scheme. An academic problem, in which the material undergoes cyclic bending deformation, is used in Section 5.2.5 to test the performance of the generally applicable adaptive scheme.

5.1 Bending dominated deformation regime

The adaptive scheme considered in this section can only trace the location of the elastic-plastic transitions which appear when a material is deformed under a combined influence of bending moment and tension. In the text below, this scheme will be referred to as AIS1. To perform the actual integration during a FE simulation, the interval processor of the scheme uses the formula for Simpson's integration with unequally spaced points. At the end of every incremental step, the algorithms of

the AIS1 scheme are called. Their main goal is to update the locations, weights and internal variables of the through-thickness integration points using the information of the finished incremental step. For each column of integration points of every element in the mesh, the interval manager of the adaptive scheme performs the following tasks:

1) the location of all elastic-plastic transitions are determined, using the method described in Section 4.2.2;

2) the complete integration interval $[-\frac{t}{2}, \frac{t}{2}]$ is divided into several subintervals, depending on the number of elastic-plastic transitions;

3) an integration point is relocated such that it coincides with the elastic-plastic transition. For simplicity this point is called the dynamic point. Since the Simpson's rule is used for the actual integration, it is ensured that there are at least three integration points within every subinterval;

4) the location of integration points adjacent to the dynamic point is adapted. They are relocated to lie in the middle of each subinterval. The position of the outermost integration points remains fixed and they are not considered for relocation;

5) a check is performed to ensure that the integration points are in ascending order after relocation;

6) the internal variables of all relocated points are updated using the theory presented in Section 4.2.4;

7) the weights of integration points are recalculated using Equations (4.27);

8) the adaptation of integration points if elastic unloading is taking place.

5.1.1 Example 1: Bending a strip under tension

The first test used to evaluate the performance of the AIS1 scheme is the simple academic problem shown in Figure 5.1. This test allows careful control of process parameters and is convenient to use for demonstration of the advantages of the adaptive integration on the scale of a single column of integration points. As shown in Figure 5.1, a strip of initially flat material was loaded by tensile and lateral forces. The thickness of the strip was 1mm, its width 8mm and the length 24mm. Boundary conditions of two symmetry planes were enforced and all translational and rotational degrees of freedom of node 1 were suppressed. The tensile forces were applied in the local coordinate system of element 6 and, therefore, their direction changed during the deformation. A magnitude of tension was chosen to give a significant shift of the neutral line. Discrete Kirchhoff triangular elements with 3 in-plane integration points were used to discretise the strip. The external loads were applied in several steps: during the first step only the tensile forces were applied, during all subsequent steps the tensile forces were kept constant and nodes 7 and 8 were displaced incrementally through a distance of 0.5mm. The material of the strip was IF steel with a Young's

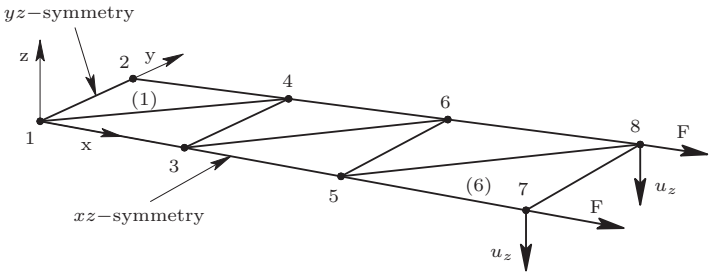

Figure 5.1: Set-up schematic for bending a strip under tension.

modulus of 210GPa, a Poisson's ratio of 0.3, an initial yield stress of 170MPa and hardening parameters C=540MPa and n=0.226. The material model used in the numerical analysis was the Hill'48 yield function with isotropic hardening. The stress-strain relation was represented by the Nadai hardening law: $\sigma = C(\varepsilon_0 + \varepsilon^p)^n$.

Simulations were performed using the AIS1 scheme as well as the traditional integration rules, i.e. Simpson's rule and Gauss quadrature. Figure 5.2 shows the integrand's profile $(\sigma_{xx} \cdot z)$ in a column of integration points of element 1 obtained at the end of the deformation before removal of the external loads. The reference solution in this figure was obtained by the standard Simpson's rule with 99 equally spaced points. This high number of the integration points was used to eliminate the numerical integration error and to obtain detailed information about the distribution of state variables through the material thickness. The adaptive scheme places the integration points in the most important locations and, therefore, provides the accurate approximation of the integrand with only 7 points. In contrast, the traditional rule with the same number of points ignores the information on the kinks

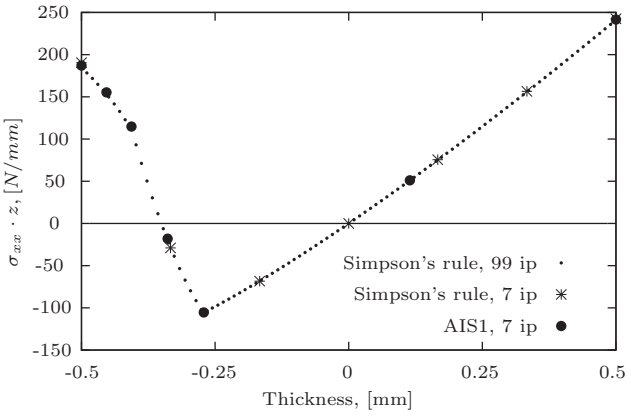

Figure 5.2: Integrand profile for a column of integration points of element 1.

and provides an oversimplified description of the integrand, which leads to a high error of stress resultants. To demonstrate this, the error in predicting the bending moment which exists in this particular location was calculated from:

$$\mathrm{RME} = \left| \frac{M_{xx} - M_{xx}^{ref}}{M_{xx}^{ref}} \right| \cdot 100\% \tag{5.1}$$

In this equation the bending moment M_{xx} is found using the σ_{xx} component of the stress vector:

$$M_{xx} = \frac{1}{2}\, t\, b \sum_{i=1}^{N_{ip}} w_i\, \sigma_{xx}(\zeta_i)\, \zeta_i \tag{5.2}$$

where N_{ip} is the number of the integration points through the thickness; b and t are the width and thickness of the material correspondingly; w_i and ζ_i are the weights and natural coordinates of the integration points. The reference bending moment M_{xx}^{ref} was obtained from the simulation with the traditional Simpson's rule and 99 integration points. The relative moment error (RME) is plotted in Figure 5.3 as a function of the number of integration points. It can be seen that the adaptive scheme performs better than the traditional rules. As can be deduced from Figure 5.2, the state of stress calculated at every integration point is equally accurate regardless of the numerical integration scheme used in the analysis. However, the adaptive scheme provides a more accurate resulting bending moment M_{xx} due to the proper location of the integration points. Note that the RME obtained when using the AIS1 scheme with 7 points remains high since only three integration points are available for the integrand's approximation on the largest subinterval with plastically deforming material. Increasing the number of points gives a better approximation of the integrand in this region and the relative moment error becomes almost negligible. To conclude, tracing the elastic-plastic transitions during a FE simulation helps to obtain

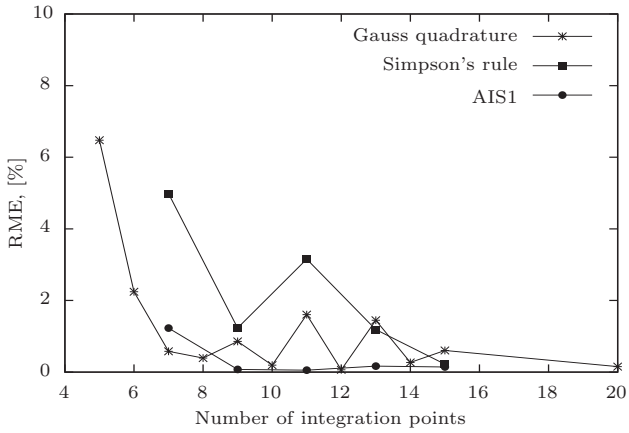

Figure 5.3: Relative error in predicting bending moment after the deformation.

more accurate stress resultants at the end of a deformation, which will guarantee an accurate prediction of the change of shape during unloading.

5.1.2 Example 2: Unconstrained cylindrical bending

To test the AIS1 scheme in realistic sheet metal forming conditions, the unconstrained cylindrical bending problem, as shown in Figure 2.9, was considered. A numerical study was carried out in which several simulations of this test were performed using different integration schemes with various numbers of points through the sheet thickness. Two materials were considered in this study: aluminium alloy (6111-T4) and dual phase steel (DP600). The material parameters are summarised in Tables 5.1 and 3.2.

In the numerical set-up the blank was arbitrary meshed with Kirchhoff triangular shell elements with 3 in-plane integration points. The average element length was 2.0mm. The tools were described using analytical functions and were considered to be perfectly rigid. The contact conditions between the blank and the tools were described using the penalty method and the Coulomb friction model. A penalty stiffness of 200MPa/mm was chosen. To model the behaviour of both materials, the Hill'48 yield criterion with isotropic hardening was used. Each simulation consisted of two steps. During the first step the actual forming was performed by closing the tools. During the springback step all contact forces were transformed into residual forces which were removed in several incremental steps.

To evaluate the developed numerical set-up, a reference simulation was performed. In this simulation, due to high computation costs, only 50 Gauss points were used through the element thickness. The aluminium alloy (6111-T4) was used as blank material. Results of the numerical analysis were compared to the experimental measurements presented at the NUMISHEET 2002 conference [22]. The angles after forming and springback predicted by the simulation were 21.77° and 59.19°, correspondingly. These values are slightly higher than the experimental ones which range from 19.5° to 21.0° for the forming angle and from 53.4° to 55.8° for the angle after springback. This discrepancy is probably caused by:

- low value of the penalty stiffness which is known to have a considerable effect on the angles in this problem, see Section 2.3.2;
- inappropriate material model used in the numerical set-up. The Hill'48 criterion

Table 5.1: Material parameters of 6111-T4 alloy.

Young's modulus, GPa	70.5
Poisson's ratio	0.33
YS_{mean}, MPa	181.8
R_0, R_{45}, R_{90}	0.894, 0.611, 0.660
C-value, MPa	539.5
n-value	0.2260

is less suitable for describing the behaviour of aluminium alloys and other yield functions must be used for that purpose [62, 102].

Qualitatively however, the simulation results are in agreement with the results of experiments and it is concluded that the numerical set-up resembles the problem with sufficient accuracy. The simulation with 50 Gauss points is considered to be a reference solution. Results of all subsequent simulations are only compared to the results obtained in the reference simulation.

Simulations with the traditional Gauss quadrature, Simpson's rule and AIS1 scheme were performed. All parameters of the numerical set-up were left unchanged and only the number of integration points through the material thickness was varied. Values of angle θ (defined in Figure 2.9) after springback obtained from these simulations are plotted in Figure 5.4. As expected, the value of the angle predicted in the simulations with the traditional integration schemes oscillates. Depending on the number of points used in the simulation, the angle after springback can be over- or underestimated (see Section 4.1.2). With an increasing number of integration points, the results converge towards the reference value which is indicated by the solid black line. In contrast, almost no oscillation of the angle value can be seen in the results obtained with the adaptive scheme. The angle is predicted quite accurately even with a small number of integration points.

The relative difference between the reference angle and the angles obtained from all other simulations is shown in Figure 5.5. From the actual shape of the blank after springback it was observed that insignificant shape deviations were obtained when the relative angle error was smaller than 0.1%. The adaptive integration scheme reaches this accuracy with 9 integration points. The traditional Gauss quadrature and Simpson's rule require at least 15 and 19 integration points respectively to guarantee the same level of error.

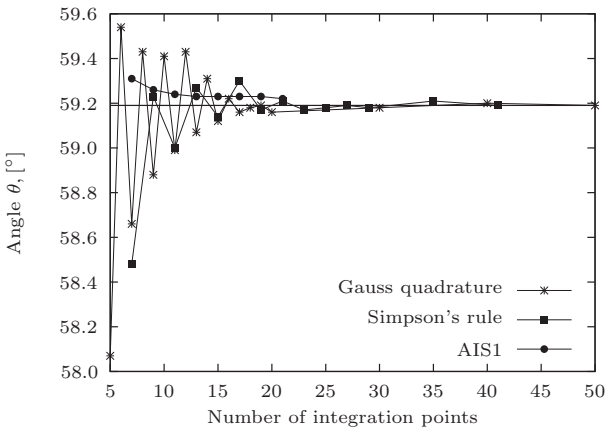

Figure 5.4: Angle after springback obtained with various integration schemes.

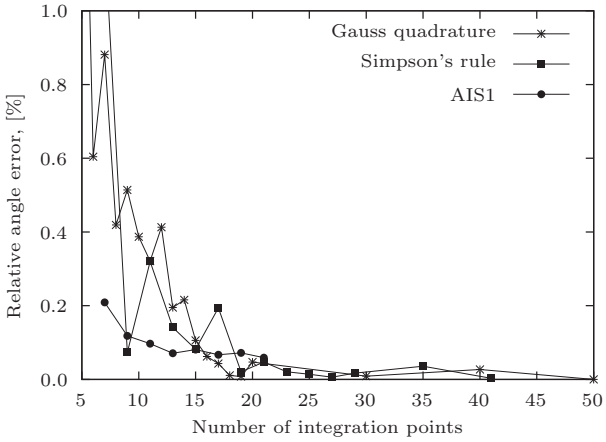

Figure 5.5: Relative error in predicting angle θ after springback.

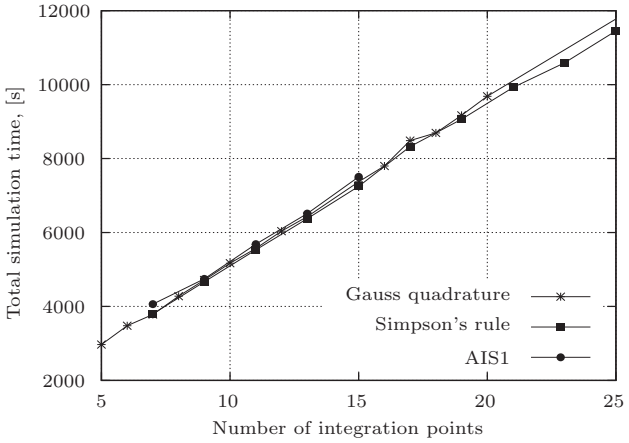

Figure 5.6: CPU time for a range of integration points.

Figure 5.6 shows the total simulation time as a function of the number of through-thickness integration points. One iteration of the Newton-Raphson procedure can generally be split into three parts: calculation of the stiffness matrix, calculation of the incremental displacement vector and calculation of the internal force vector. Using twice as many integration points will double the time needed to assemble the stiffness matrix and to calculate the vector of internal forces. The time needed to solve the global system of equations to find incremental displacements depends only on the number of degrees of freedom. For a numerical model with up to 10000 degrees of freedom the time needed by a solver takes a negligible fraction of the total iteration time [111]. The number of independent degrees of freedom in the current model is

6902. Therefore, as can be seen in Figure 5.6, increasing the number of integration points leads to a linear increase in the total simulation time. It is interesting to note that the extra calculations needed for the adaptive integration lead to a very small increase in the total time (about 5%). For this problem, compared to the traditional numerical schemes, using the adaptive integration in the analysis results into substantial CPU time savings.

Two additional sets of simulations of this test were performed in which the material and some geometric parameters were changed. The relative angle error obtained from the simulations with the dual phase steel (DP600) is shown in Figure 5.7. As can be

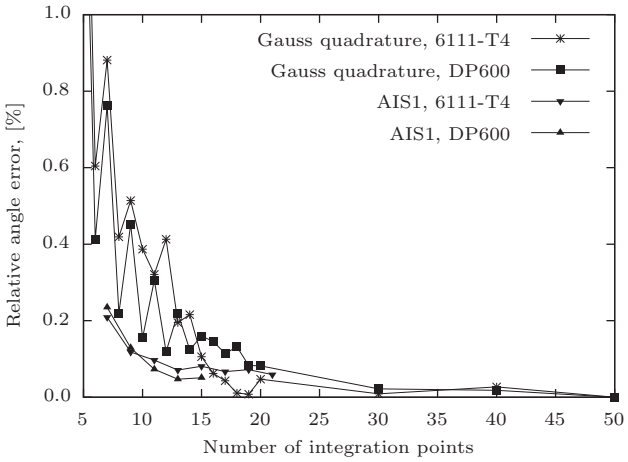

Figure 5.7: Relative error in predicting angle θ: simulations with different materials.

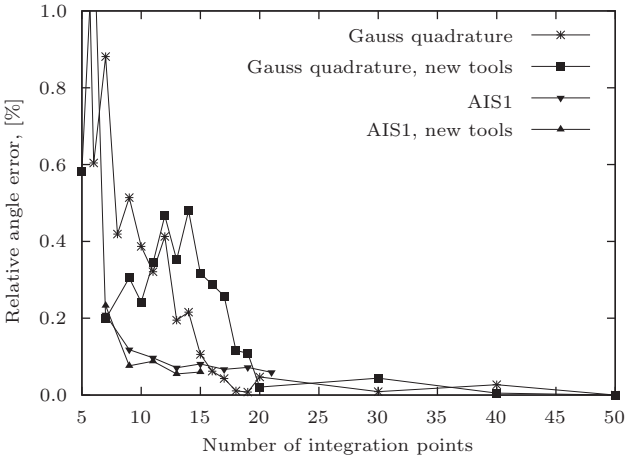

Figure 5.8: Relative error in predicting angle θ: simulations with modified tool geometry.

seen, when the material parameters are changed, the traditional Gauss quadrature requires more integration points to guarantee the same level of accuracy compared to the simulations with the aluminium alloy. In this case, it was necessary to use 19 Gauss points to minimise the influence of the numerical integration error on the accuracy of springback prediction. For the adaptive scheme this number remains unchanged. A similar situation occurs when some geometric parameters of the problem are changed, e.g. the tools' radii are increased by 5.0mm. Figure 5.8 shows that the traditional Gauss quadrature requires 19 integration points to ensure the specific error level. Again, the number of points of the adaptive scheme to achieve the accuracy of 0.1% does not change. Hence, contrary to the traditional integration, the accuracy of the adaptive integration is insensitive to material properties and changes in geometry. These results show that in addition to the CPU time savings the adaptive scheme promises better accuracy when using a specific number of integration points.

5.2 Cyclic deformation

In the deep drawing process a material is usually subjected to a cyclic bending deformation under tension. When the material is drawn over a tool radius it undergoes one cycle of bending and unbending. Several cycles are possible when the material is pulled through a drawbead and their number depends on the actual drawbead geometry. These cyclic loading conditions may produce multiple kinks in the through-thickness stress profile which can be detrimental to the accuracy of the numerical integration. To be applicable for simulations of realistic industrial problems, the adaptive strategy defined in Chapter 4 must be extended. A new algorithm for the interval manager is needed that can locate stress profile kinks in arbitrary loading conditions.

5.2.1 Definition of important stress profile kinks

In order to demonstrate what stress profiles can develop through the material thickness under realistic loading conditions, simulations of the academic problem shown in Figure 5.1 were performed. Geometrical parameters of the test and the boundary conditions are described in Section 5.1.1. Cyclic bending was enforced by displacing nodes 7 and 8 in the positive and the negative $z-$directions. A constant tensile force which caused a considerable neutral line shift was applied to nodes 7 and 8 in the local coordinate system of element 6. The simulations were performed with the dual phase steel DP600 (see Table 3.2 for the material properties). The strip was meshed using 6 discrete Kirchhoff triangular elements and the integration in the thickness direction was performed by the traditional Simpson's rule with 99 points.

A simulation of a deformation sequence was performed which included bending (B), reverse bending (BR) and repeated bending in the original direction (BRB). The total displacement of nodes 7 and 8 during each step of the deformation sequence was 1mm. Evolution of the circumferential stress σ_{xx} in a particular column of integration points of element 1 is shown in Figure 5.9. After the bending, there are two elastic-plastic

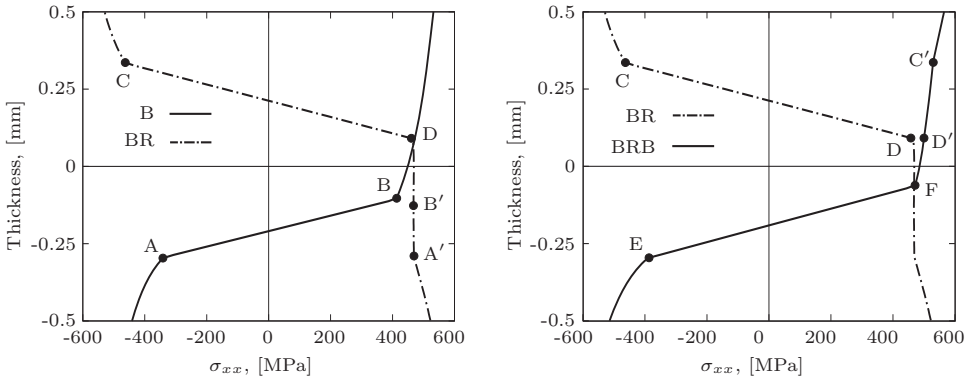

(a) loading steps B and BR (b) loading steps BR and BRB

Figure 5.9: Distribution of σ_{xx} in a column of integration points of element 1 during cyclic loading: a) stress profiles after bending and reverse bending; b) stress profiles after reverse bending and repeated bending in the original direction.

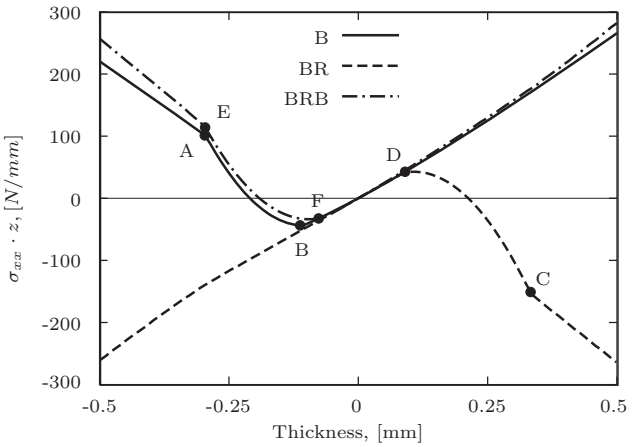

Figure 5.10: Integrand profile at various steps of cyclic bending.

transitions (A and B). At the beginning of reverse loading the material is released from the bending loads and stress relaxation takes place. Bending in the reverse direction straightens the material and two new elastic-plastic transitions (C and D) can be found in the stress profile. At this moment the old kinks, now located in the plastic region below the central line, are less pronounced. As shown in Figure 5.9(b), a similar situation occurs during the last step of the deformation sequence. After the stress relaxation the material again starts to deform plastically and a new pair of elastic-plastic transitions (E and F) becomes more prominent.

The stress distribution at the end of every step of the deformation sequence contains an elastic region. The size of this region is determined by the elastic-plastic transitions

which also define the global shape of the stress profile. By the time the plastic deformations are initiated during bending in the opposite direction, the old stress profile kinks dissolve in the newly-formed plastic region and are of little interest for the adaptive integration. This is more clearly illustrated in Figure 5.10 by plotting the integrand's profiles ($\sigma_{xx} \cdot z$) at the end of every loading step of the deformation sequence. It can be seen that the profiles' shapes are mainly characterised by the points that separate the elastic and plastic material. Therefore, it is possible to conclude that in the case of a cyclic deformation, the interval manager of the adaptive scheme must be able to trace the location of the actual elastic-plastic transitions that bound the elastic region during the current loading step.

It is believed that the FE model considered here is sufficiently accurate to be a reliable basis for drawing the latter conclusion. Using, for example, an advanced hardening model which can accurately describe the cyclic deformation is likely to change the position of elastic-plastic transitions, but the global shape of the stress profiles will remain the same. Additionally, the stress profiles obtained in the considered FE simulation do not contradict the results of the cyclic bending analysis presented in the literature, e.g. [150, 151]. In their study, Roberts and Sheppard developed, and experimentally validated a numerical model used to predict stress and strain distributions in sheet material during the tension-levelling process.

5.2.2 Locating elastic-plastic interfaces in cyclic bending

In this section an algorithm is presented which can be used to determine the through-thickness location of elastic-plastic transitions in a material subjected to a cyclic bending deformation. The calculations discussed here were performed at the end of the incremental step and for each column of integration points of every element in the mesh. It is assumed that a set of internal variables at the end and at the beginning of the current step n is available at every integration point. This includes the total strain $\{\boldsymbol{\varepsilon}\}$, the plastic strain $\{\boldsymbol{\varepsilon}^p\}$, the equivalent plastic strain $\bar{\varepsilon}$, the stress state $\{\boldsymbol{\sigma}\}$ and some hardening parameters $\{\boldsymbol{q}\}$. In the text below the subscript $n-1$ denotes variables at the beginning of the current step and the subscript n denotes variables at the end of the step.

General idea

To find the location of elastic-plastic transitions the through-thickness distribution of the yield condition $\phi\big(\{\boldsymbol{\sigma}_n^{trial}\}, \{\boldsymbol{q}_n\}\big)$ can be used. In case of the Hill'48 yield criterion and isotropic hardening the yield condition can be described in the following simple form [152]:

$$\begin{aligned} \phi &= \sqrt{\{\boldsymbol{\sigma}_n^{trial}\}^T [\boldsymbol{P}] \{\boldsymbol{\sigma}_n^{trial}\}} - \sqrt{\frac{2}{3}(F+G+H)}\, \sigma_f(\bar{\varepsilon}_n^p) = \\ &= \sqrt{\{\boldsymbol{\sigma}_n^{trial}\}^T [\boldsymbol{P}] \{\boldsymbol{\sigma}_n^{trial}\}} - \sqrt{\xi}\, \sigma_f(\bar{\varepsilon}_n^p) \end{aligned} \tag{5.3}$$

where $\{\boldsymbol{\sigma}_n^{trial}\}$ is the trial stress calculated by considering the total strain increment

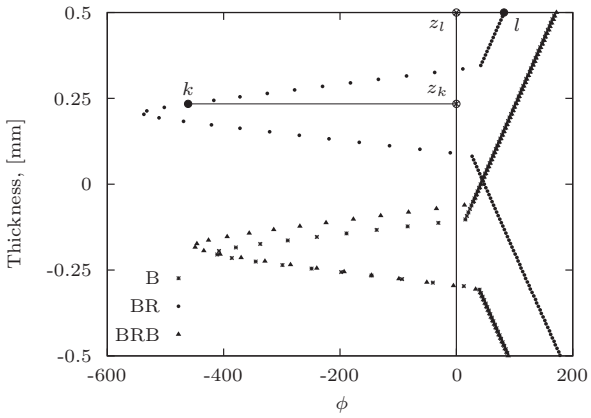

Figure 5.11: Through-thickness distribution of the yield condition during cyclic loading. The results were obtained from a FE simulation with 99 integration points.

as elastic, $[\boldsymbol{P}]$ is the matrix that includes the material anisotropy parameters and σ_f is the current flow stress. The academic problem considered in Section 5.2.1 was used to visualise the distribution of the yield condition and some other state variables through the material thickness. Figure 5.11 shows values of ϕ for a complete column of integration points of element 1 after bending, reverse bending and repeated bending in the original direction. Note that $\phi > 0$ in the regions of plastic deformation since the trial stress state is used in Equation (5.3). The point where the yield condition is satisfied ($\phi = 0$) indicates the location of the elastic-plastic transition. The procedure to locate this transition using a limited number of integration points comprises three major steps. First, the region which incorporates the elastic-plastic transition is found. This is done by evaluating the state information of all available integration points. The stress profile kink lies between two adjacent points that are in elastic and plastic deformation regimes (for example points k and l in Figure 5.11). Hence, using the information from these or some additional points, the yield condition ϕ is defined locally as a function of the through-thickness coordinate z. Finally, by finding numerically the root of equation $\phi(z) = 0$ at the end of the current incremental step it is possible to calculate the location of the elastic-plastic transition.

It is important to mention that the Hill'48 yield condition is chosen here for demonstration purposes only. The algorithm described in this section imposes no restrictions on the type of yield function that can be used in the numerical analysis. Complexity of the yield condition equation $\phi(z) = 0$ will not become an obstacle since a numerical method is used to find the roots of this function.

Trial stress and total strain

To completely define $\phi(z)$ on subinterval $[z_k, z_l]$, the trial stress $\{\boldsymbol{\sigma}_n^{trial}\}$ and the flow stress σ_f must be expressed as a function of the $z-$coordinate. From the definition

of the trial stress:

$$\{\boldsymbol{\sigma}_n^{trial}\} = \{\boldsymbol{\sigma}_{n-1}\} + [\boldsymbol{E}]\,\{\Delta\boldsymbol{\varepsilon}_n\} \tag{5.4}$$

where $\{\boldsymbol{\sigma}_{n-1}\}$ is the stress state at the beginning of the increment, $[\boldsymbol{E}]$ is the elasticity matrix and $\{\Delta\boldsymbol{\varepsilon}_n\}$ is the total strain increment during the current step. The stress state at the beginning of the incremental step is given by:

$$\{\boldsymbol{\sigma}_{n-1}\} = [\boldsymbol{E}]\left(\{\boldsymbol{\varepsilon}_{n-1}\} - \{\boldsymbol{\varepsilon}_{n-1}^p\}\right) \tag{5.5}$$

Combining Equations (5.4) and (5.5) yields the following expression for the trial stress:

$$\begin{aligned}\{\boldsymbol{\sigma}_n^{trial}\} &= [\boldsymbol{E}]\left(\{\boldsymbol{\varepsilon}_{n-1}\} - \{\boldsymbol{\varepsilon}_{n-1}^p\}\right) + [\boldsymbol{E}]\,\{\Delta\boldsymbol{\varepsilon}_n\} = \\ &= [\boldsymbol{E}]\left(\{\boldsymbol{\varepsilon}_{n-1}\} + \{\Delta\boldsymbol{\varepsilon}_n\} - \{\boldsymbol{\varepsilon}_{n-1}^p\}\right) = \\ &= [\boldsymbol{E}]\left(\{\boldsymbol{\varepsilon}_n\} - \{\boldsymbol{\varepsilon}_{n-1}^p\}\right)\end{aligned} \tag{5.6}$$

As follows from Equation (3.2), the distribution of the total strain through the thickness of a shell element is linear. Therefore, the accumulated total strain $\{\boldsymbol{\varepsilon}_n\}$ can be written as a function of the $z-$coordinate by using simple interpolation of values at the outer integration points. Let $\{\boldsymbol{\varepsilon}\}_b$ and $\{\boldsymbol{\varepsilon}\}_t$ be the total strains calculated at the outer integration points and let z_b, z_t be their corresponding coordinates. The distribution of the total strain on subinterval $[z_k, z_l]$ can be described as follows:

$$\begin{aligned}\{\boldsymbol{\varepsilon}\} &= \frac{\{\boldsymbol{\varepsilon}\}_t - \{\boldsymbol{\varepsilon}\}_b}{z_t - z_b}\,z + \frac{\{\boldsymbol{\varepsilon}\}_b z_t - \{\boldsymbol{\varepsilon}\}_t z_b}{z_t - z_b} = \\ &= \{\boldsymbol{a}_1\}\cdot z + \{\boldsymbol{a}_2\}, \quad z_b \le z \le z_t\end{aligned} \tag{5.7}$$

Note that all quantities in this equation are evaluated at the end of the current incremental step.

The procedure for defining distributions of the remaining quantities $\{\boldsymbol{\varepsilon}_{n-1}^p\}$ and σ_f on the target subinterval is given below. For convenience of explanation, the particular steps of the loading sequence discussed in Section 5.2.1 are considered.

Loading step 1: Initial bending

During this loading step the material which has not been plastically deformed earlier, is bent and stretched simultaneously. As soon as the outermost integration points start to deform plastically and the target subinterval is specified, the trial stress distribution can easily be determined, since during the previous step all integration points remained elastic, i.e. $\{\boldsymbol{\varepsilon}_{n-1}^p\}_i = 0$, for $i = 1, \ldots, N_{ip}$. As a result, combining Equations (5.6) and (5.7) gives the expression for the trial stress on subinterval $[z_k, z_l]$:

$$\{\boldsymbol{\sigma}_n^{trial}\}_{kl} = [\boldsymbol{E}]\left(\{\boldsymbol{a}_1\}\cdot z + \{\boldsymbol{a}_2\}\right), \quad z_b \le z \le z_t \tag{5.8}$$

The flow stress expression can easily be obtained if the distribution of the equivalent plastic strain $\bar{\varepsilon}_n^p$ is known. Under these loading conditions, the equivalent plastic

strain has an approximately bilinear distribution on subinterval $[z_k, z_l]$. It equals zero between the elastic point k and the elastic-plastic transition, and from the elastic-plastic transition up to the plastic point l it varies almost linearly. This approximation is possible since for metals elastic strains are much smaller compared to the plastic strains. Therefore, the distribution of the accumulated plastic strain $\{\boldsymbol{\varepsilon}_n^p\}$, and hence of the equivalent plastic strain $\bar{\varepsilon}_n^p$, is approximately linear in the region of plastic deformation. The actual slope of this distribution is not known since only two integration points are available within subinterval $[z_k, z_l]$. This difficulty, however, can be easily evaded by noting that the yield condition must be defined accurately only between the elastic point k and the elastic-plastic transition (see Figure 5.11). In this case there will be enough information to find the needed point of intersection. Therefore it is assumed that the equivalent plastic strain equals zero throughout the entire subinterval, which means that the flow stress between points k and l remains constant and equal to the initial yield stress, i.e. $\sigma_f = \sigma_{y0}$.

At this stage, all terms have been defined and the equation which describes the distribution of the yield condition on the target subinterval becomes:

$$\phi(z) = \sqrt{\{\boldsymbol{\sigma}_n^{trial}\}_{kl}^T [\boldsymbol{P}] \{\boldsymbol{\sigma}_n^{trial}\}_{kl}} - \sqrt{\xi}\,\sigma_{y0}, \quad z_k \le z \le z_l \tag{5.9}$$

Loading step 2: Reverse bending

Prior to this loading step the accumulated plastic strain at some integration points of the considered column may have a nonzero value. Hence, the distribution of the plastic strain on subinterval $[z_k, z_l]$ must be derived. As an example, the through-thickness distribution of the ε_{xx}^p component of the plastic strain vector is plotted in Figure 5.12, to support the explanation. As can be seen, after bending in the original direction there remains a fraction of the material which is still elastic ($\varepsilon_{xx}^p = 0$) and the plastic strain distribution above and below the elastic zone is approximately linear. During the reverse bending, there is a region between points C and D where the plastic strain does not change, indicating the zone where the material remains elastic. As soon as integration point l becomes plastic, the expression that describes distribution of the plastic strain $\{\boldsymbol{\varepsilon}_{n-1}^p\}$ on subinterval $[z_k, z_l]$ can be found by interpolating values at the elastic point k and the plastic point l. This is possible since at the beginning of the current incremental step the integration point l was still elastic, and hence it can be used to define the actual slope of CD:

$$\begin{aligned} \{\boldsymbol{\varepsilon}^p\} &= \frac{\{\boldsymbol{\varepsilon}^p\}_l - \{\boldsymbol{\varepsilon}^p\}_k}{z_l - z_k}\, z + \frac{\{\boldsymbol{\varepsilon}^p\}_k z_l - \{\boldsymbol{\varepsilon}^p\}_l z_k}{z_l - z_k} = \\ &= \{\boldsymbol{a}_3\} \cdot z + \{\boldsymbol{a}_4\}, \qquad \text{with} \quad z_k \le z \le z_l \end{aligned} \tag{5.10}$$

Note that linear interpolation is used and all quantities are defined at the beginning of the current step. Before the next incremental step, the algorithms of adaptive integration will relocate the integration point k to lie on the elastic-plastic transition and update its internal variables. As yielding during the next incremental step progresses, this point will become plastic and it will be possible to use point k and a subsequent point m to define the plastic strain profile on the new target subinterval.

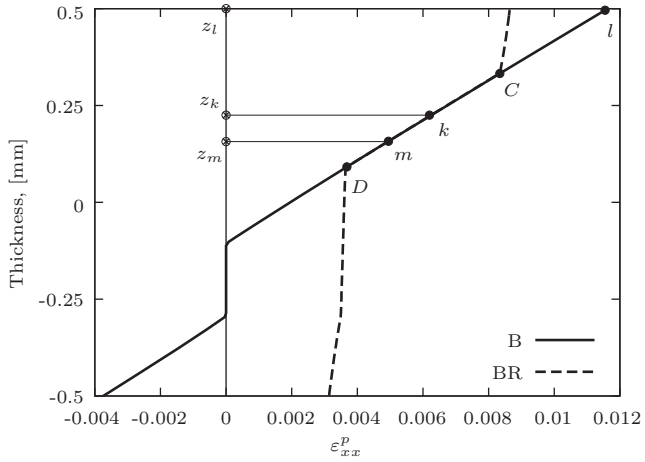

Figure 5.12: Through-thickness distribution of the accumulated plastic strain after bending and reverse bending.

Substituting Equations (5.7) and (5.10) into Equation (5.6) gives the trial stress distribution on the target subinterval during reverse bending:

$$\{\boldsymbol{\sigma}_n^{trial}\}_{kl} = [\boldsymbol{E}]\Big(\big(\{\boldsymbol{a}_1\} - \{\boldsymbol{a}_3\}\big)\cdot z + \{\boldsymbol{a}_2\} - \{\boldsymbol{a}_4\}\Big), \quad z_k \le z \le z_l \tag{5.11}$$

Next, the flow stress profile on the target subinterval must be defined. In order to do this, the equation that describes the equivalent plastic strain $\bar{\varepsilon}^p_n$ distribution is needed. Similar to the initial bending case, this equation cannot be accurately defined by using simple interpolation of values of the elastic point k and the plastic point l. This is demonstrated in Figure 5.13, where reference profiles of the equivalent plastic strain obtained at the previous incremental step $n-1$ and the current step n are shown. As soon as the material starts yielding during the current step, the plastic point l departs from the elastic slope CD and the equivalent plastic strain distribution becomes approximately bi-linear. This distribution is then approximated by a line which is defined using information from the elastic point k at the end of the increment and information from the plastic point l at the beginning of the increment:

$$\begin{aligned} \bar{\varepsilon}^p &= \frac{\bar{\varepsilon}^p_{l(n-1)} - \bar{\varepsilon}^p_{k(n)}}{z_{l(n-1)} - z_{k(n)}}\, z + \frac{\bar{\varepsilon}^p_{k(n)} z_{l(n-1)} - \bar{\varepsilon}^p_{l(n-1)} z_{k(n)}}{z_{l(n-1)} - z_{k(n)}} = \\ &= a_5 \cdot z + a_6, \qquad \text{for} \quad z_k \le z \le z_l \end{aligned} \tag{5.12}$$

In this way the flow stress, and hence the yield condition, will be defined accurately only between points k and C which is sufficient to find the location of the elastic-plastic transition. The flow stress distribution at the end of the current step can now be determined. For example, for isotropic hardening and using the Nadai relation:

$$\sigma_f = C\left(\varepsilon_0 + a_5 \cdot z + a_6\right)^n, \quad z_k \le z \le z_l \tag{5.13}$$

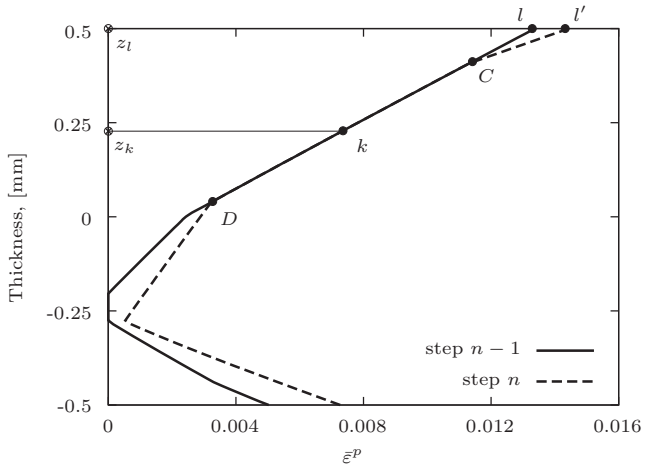

Figure 5.13: Through-thickness distribution of equivalent plastic strain calculated at two subsequent incremental steps.

Finally, the yield condition as a function of the through-thickness coordinate in the case of reverse bending becomes:

$$\begin{aligned} \phi(z) &= \sqrt{\{\boldsymbol{\sigma}_n^{trial}\}_{kl}^T [\boldsymbol{P}] \{\boldsymbol{\sigma}_n^{trial}\}_{kl}} - \sqrt{\xi}\, C \left(\varepsilon_0 + a_5 \cdot z + a_6\right)^n, \\ &\text{where} \quad z_k \leq z \leq z_l \end{aligned} \tag{5.14}$$

The same procedure can be followed to define the distributions of $\{\boldsymbol{\varepsilon}_{n-1}^p\}$ and σ_f on the target subinterval for the case in which the material is subjected to repeated bending in the original direction.

Validation: Local approximation of yield condition

To validate the accuracy of the developed equations for the yield condition distribution ((5.9) and (5.14)), a FE simulation of the cyclic bending problem was performed using only 9 integration points through the element thickness. Local approximations of the yield condition are compared to the reference profiles in Figure 5.14. The results are plotted at the end of bending and reverse bending steps of the loading sequence. The elastic and plastic points that define the target subintervals during every step are marked with solid dots. It can be seen that the approximating functions coincide with the reference distributions, which means that the developed equations can give an accurate local approximation of the yield condition using a limited number of integration points.

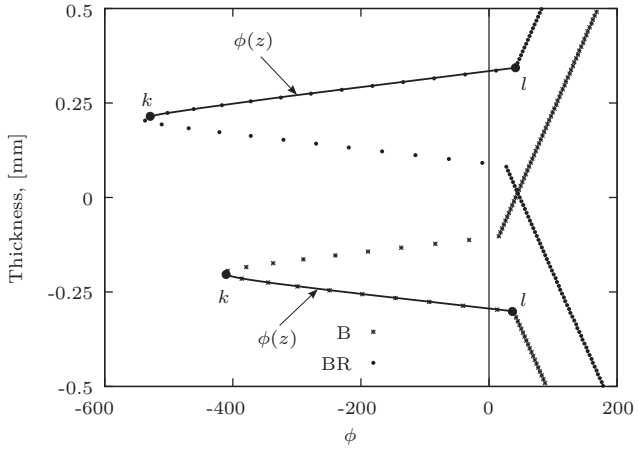

Figure 5.14: Local approximations of the yield condition after bending and reverse bending.

Finding roots of approximating functions

As soon as the yield condition is approximated locally, the location of the elastic-plastic transition is determined by finding the numerical solution of the equation $\phi(z) = 0$. Various root-finding algorithms can be used for this purpose, see for example methods presented in [120]. Since the local approximation of the yield condition is a simple and continuous function, the false position method is used here. The description of this fast and robust method can be found in [120] and an example of its efficient implementation is given in [153].

5.2.3 Generally applicable adaptive integration scheme

By combining the algorithm that locates elastic-plastic interfaces in cyclic bending and some other components of the adaptive integration, the generally applicable adaptive integration scheme (GAIS) is defined. To perform the actual integration during a simulation the interval processor of the scheme uses Simpson's rule, which can cope with unequally spaced points. Most of the procedures of the interval manager are similar to those of the AIS1 scheme described in Section 5.1. An important additional task, performed by the interval manager of GAIS scheme, includes redistribution of integration points before yielding of the material is initiated during the reverse bending. While bending in the original direction, due to the neutral line shift, it may happen that most of the integration points are concentrated on one side of the central line (see for example Figure 5.2). The redistribution will ensure that there is a sufficient number of integration points above and below the central line to trace the elastic-plastic transitions during the reverse bending.

5.2.4 Numerical validation of GAIS scheme

The generally applicable adaptive integration scheme is first validated by performing simulations of the problem considered already, i.e. the unconstrained cylindrical bending. The complete description of the numerical set-up was given in Section 5.1.2. Several FE simulations of this test were performed using the GAIS scheme with various numbers of through-thickness integration points. The aluminium alloy 6111-T4 was used in the simulations and its material properties were summarised in Table 5.1. At the end of every simulation, the angle θ defined in Figure 2.9 was calculated and compared to the reference value obtained in the numerical analysis with 50 Gauss points. The relative difference between the angles is plotted in Figure 5.15 as a function of the total number of points in the thickness direction. Previous results obtained with traditional Gauss quadrature, Simpson's rule and the adaptive AIS1 scheme are added to this plot. By comparing the adaptive rules, it is possible to conclude that the GAIS scheme performs equally well in this deformation regime. It is also observed that employing this scheme in the analysis only leads to an increase in the total simulation time of about 5%. The reason is that although it uses an iterative method to find the elastic-plastic transitions, the local approximations of the yield condition are smooth and continuous functions and only few iterations are needed to find their roots.

5.2.5 Simulation of cyclic bending of a strip

A numerical study was carried out to demonstrate the performance of the GAIS scheme in a cyclic deformation regime. The academic problem depicted in Figure 5.1 was considered in the study. The geometrical parameters and the boundary conditions of the numerical model were described in Section 5.1.1. The strip was meshed with 6

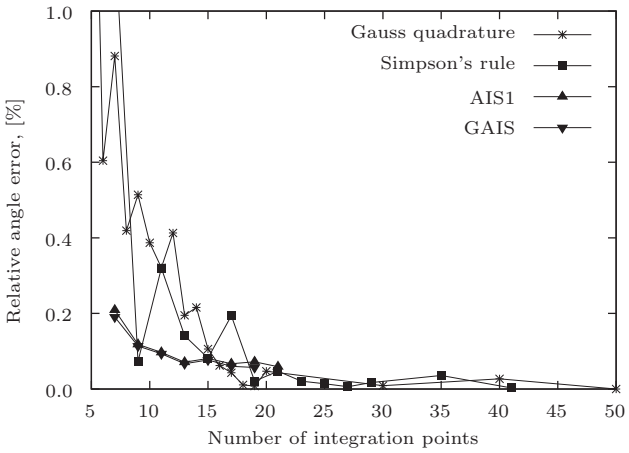

Figure 5.15: Relative error in predicting angle θ after springback.

discrete Kirchhoff triangular elements. The cyclic deformation included three loading steps, i.e. bending, reverse bending and repeated bending in the original direction. During the deformation, the strip was additionally loaded by a tensile force to create a significant shift of the neutral line. Dual phase steel (DP600) was used in the study and the material behaviour was described by the Hill'48 yield criterion with isotropic hardening. A set of simulations was performed using the traditional rules and the adaptive GAIS scheme while varying the number of the through-thickness integration points. Results of the simulations are compared to the reference solution which is obtained by using the traditional Simpson's rule with 99 integration points.

The distribution of the integrand ($\sigma_{xx} \cdot z$) in a column of integration points of element 1 is examined first. The integrand's values at every integration point after all the loading steps are plotted in Figure 5.16. As shown, the GAIS scheme can accurately trace the location of elastic-plastic transitions at every step of the loading sequence. It makes an efficient use of available integration points and provides an accurate approximation of the integrand during the numerical analysis. Note that only the important kinks are traced during the simulation, which means that when new elastic-plastic transitions are formed during every subsequent loading step, tracing of the old kinks is stopped.

The error in predicting the stress resultants is discussed next. State variables after the reverse bending step were used in all calculations. The relative error of the bending moment in a particular location of element 1 is shown in Figure 5.17. By comparing the results presented in Figures 5.3 and 5.17 it is possible to see that the adaptive integration performs equally well in the cyclic deformation regime. Compared to the traditional rules, for a fixed number of the integration points it gives a better prediction of the stress resultants and suppresses the error oscillation. The accuracy of the change of shape due to springback will be high if the stress resultants are accurately predicted in every column of integration points of the complete mesh. To characterise the influence of numerical integration in the thickness direction on the

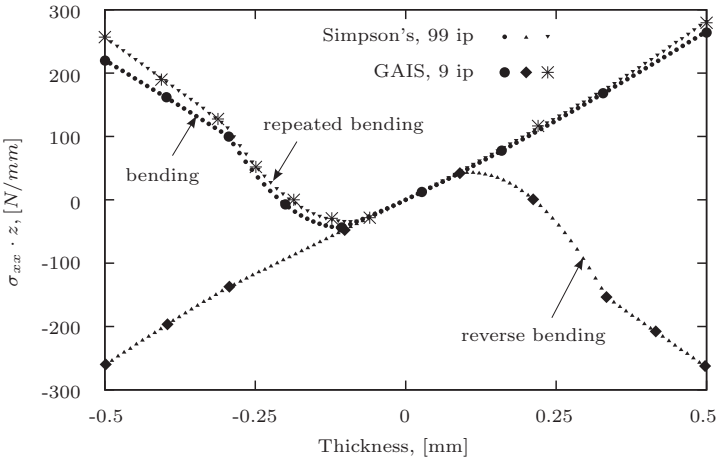

Figure 5.16: The integrand's profile at various steps of cyclic bending.

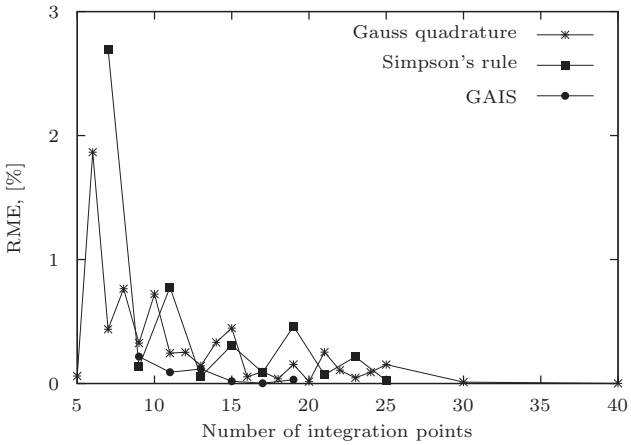

Figure 5.17: Relative error in predicting the moment after the reverse bending.

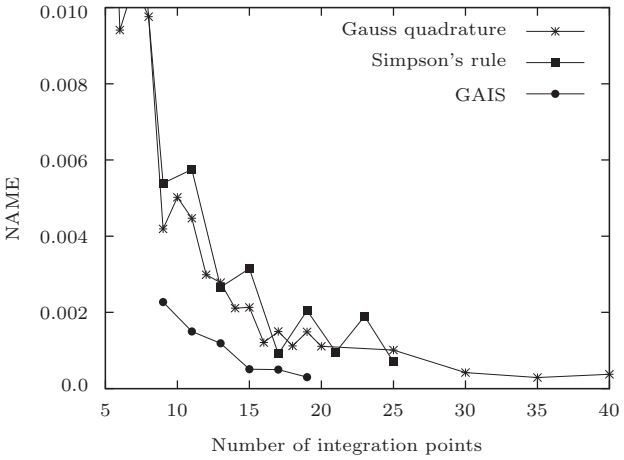

Figure 5.18: Variation of the normalised average moment error with N_{ip} for various integration rules.

accuracy of change of shape during unloading, the normalised average moment error (NAME) is introduced. This quantity is a ratio of ℓ_2 norms:

$$NAME = \frac{\|\{\boldsymbol{M}_{xx}\} - \{\boldsymbol{M}_{xx}^{ref}\}\|_2}{\|\{\boldsymbol{M}_{xx}^{ref}\}\|_2} = \frac{\left[\sum_{i=1}^{N_{col}} \left(M_{xx(i)} - M_{xx(i)}^{ref}\right)^2\right]^{\frac{1}{2}}}{\left[\sum_{i=1}^{N_{col}} \left(M_{xx(i)}^{ref}\right)^2\right]^{\frac{1}{2}}} \tag{5.15}$$

where N_{col} is the total number of columns of integration points in the complete mesh,

$M^{ref}_{xx(i)}$ is the bending moment in a particular column calculated in the reference simulation and $M_{xx(i)}$ is the bending moment in the same column obtained in all other simulations. Dependency of the normalised average moment error on the integration rule and the number of points in thickness direction is shown in Figure 5.18. A more accurate change of shape during unloading is expected in the simulation which uses the adaptive GAIS scheme, since for this scheme NAME has the lowest value on almost the entire range of integration points. By tracing the location of elastic-plastic transitions during the cyclic deformation, the scheme ensures more accurate stress resultants before elastic unloading begins.

5.3 Concluding remarks

A simplified adaptive scheme to integrate through the thickness of discrete Kirchhoff shell elements was implemented in the implicit FE code DiekA. The scheme changes the through-thickness position of the integration points during the FE simulation. Depending on the location of elastic-plastic transitions, the integration points are relocated to guarantee a more accurate change of shape during unloading.

The performance of the scheme in a numerical analysis of springback was evaluated using several test problems. Simulations of a simple academic test clearly demonstrated the advantages of adaptive integration. In contrast to the traditional rules, it ensures that accurate stress resultants are obtained at the end of a deformation with a limited number of integration points. Since the location of the points is not fixed during the analysis, the adaptive integration does not exhibit the error oscillation typical of the traditional schemes. The numerical integration error decreases monotonically with increasing number of points. The numerical study based on the unconstrained cylindrical bending problem showed that by requiring less integration points for the accurate analysis of springback the adaptive scheme significantly decreased the total computation time. Additionally, it was demonstrated that the accuracy of adaptive integration was not influenced by changes in physical and numerical parameters and a specific error level can be ensured by using a particular number of points.

The simplified adaptive scheme has been extended to make it applicable in realistic loading conditions. Simulations of the cyclic deformation of a strip were used to define the stress profile kinks that have the biggest influence on the accuracy of numerical integration. A new algorithm was developed to trace the location of the main elastic-plastic transitions that appear during a cyclic deformation. It is based on defining the local approximation of the yield condition between the elastic and plastic integration points and poses no restrictions on choosing the type of yield function. The performance of the generally applicable adaptive integration scheme was evaluated using a simple academic problem. Simulations of the test showed that in the numerical analysis of cyclically deforming material the adaptive scheme provides a better prediction of the stress resultants and thus ensures an accurate change of shape upon unloading.

CHAPTER

SIX

CONCLUSIONS AND RECOMMENDATIONS

FE simulation of sheet metal forming is a well-established tool which is used in the industrial practice to evaluate geometrical defects caused by elastic springback after forming. The accuracy of the information obtained in a numerical simulation is essential for product designers and die makers. To keep the product development time and manufacturing costs low, FE analysis must provide reliable information necessary for the modification of tool and product geometry. Modelling guidelines and advanced numerical algorithms that can be used to perform an accurate FE simulation of springback in sheet metal forming are presented in this thesis.

To obtain reliable information from the FE analysis of springback, it is essential to fully understand the phenomenon and to carefully consider all sources of error of its prediction. It was demonstrated that the change of shape of the formed part is mainly caused by the relief of internal stresses developed during the deformation, hence all factors that govern the evolution of the stress state in sheet material have a direct influence on the amount of springback. A brief description of experimental procedures that are typically used to study the influence of various factors on the magnitude of springback in sheet metal forming was provided. Springback dependency on some material and process parameters was demonstrated with the help of a simple analytical model. The presented analytical model can be used to predict the change of curvature in the elastic-plastic sheet in the case of plane strain bending under tension.

For a successful FE analysis of springback it is important to prepare an adequate numerical model. Special attention must be given to choosing the appropriate constitutive law which must accurately represent the material behaviour during a deformation. It was emphasised that for an accurate springback prediction, it may be required to use a material model which can take into account the inelastic effects that occur during unloading. Although the mechanisms underlying the degradation of the apparent Young's modulus have been understood, the amount of extra inelastic strain in realistic loading conditions is not known and research in this field is recommended.

Extension of the existing constitutive laws to make them capable of describing the Young's modulus degradation could be an additional topic for research.

Based on the simulations of two benchmark problems it was demonstrated that the numerical model must reflect the physical contact conditions that exist during the stamping process. It is recommended to use the real drawbead geometry during forming and realistic tool retraction during unloading. Simplifying assumptions and the uncertainty with the parameters of equivalent drawbeads make the numerical model unreliable for the accurate analysis of springback. When retracting the tools after forming, contact forces are present between the tools and the blank. It was shown that these forces may have an influence on the change of shape during unloading and must not be neglected. Research should be done to investigate the possibility of developing a method for simulation of unloading that provides a good approximation of the realistic retraction procedure and which is more computationally efficient.

Large modelling errors may also be encountered if an inappropriate element type is used in the springback analysis. It was shown that a two-dimensional plane strain model may not be adequate since it completely neglects lateral bending effects and, thus provides an oversimplified representation of the problem. Finally, while analysing results of the FE simulation it is important to remember that there are different types of springback in sheet metal forming. Overstretching of shallowly curved parts during forming may lead to larger distortions of the product shape during unloading.

Minimising the discretisation error is equally important for an accurate springback prediction. Simulations of the single die bending test and the top-hat section test were used to define guidelines for the blank and tool discretisation. It was shown that using less than 10 blank and tool elements in the curved regions results into an inaccurate prediction of the stress state at the end of forming.

Major limitations of the traditional schemes employed for the through-thickness integration of shell elements were demonstrated using the analytical stretch bending model. It was shown that efficiency of the numerical integration can be improved by making integration points dynamic and by placing a point to coincide with the interface which separates elastic and plastic regions of the material. A strategy for the adaptive through-thickness integration for shell elements was presented. To be able to perform the adaptation of the integration points during the FE simulation, the strategy requires algorithms that locate the elastic-plastic transitions, redistribute the available points, update their state variables and perform the actual integration. Several formulae for integration with unequally distributed points were derived. To make the strategy generally applicable, an algorithm was developed to locate elastic-plastic interfaces in realistic loading conditions and independently of the yield function used in the numerical analysis. It is based on defining the approximation of the yield condition on the small interval between the elastic and plastic integration points.

By combining the algorithms of the strategy, a generally applicable adaptive integration scheme was formulated and implemented in an implicit FE code. The unconstrained cylindrical bending problem and several academic examples were used to evaluate its performance and to demonstrate the advantages of adaptive integration over the traditional schemes. The simulations showed that accurate stress resultants

can be obtained at the end of forming with a limited number of the integration points. By requiring less points for the accurate analysis of springback, the adaptive scheme significantly decreases the total computation time. It was additionally demonstrated that its accuracy is not influenced by changes in physical and numerical parameters and a specific error level can be ensured by using a particular number of points.

The algorithm that performs the update of state variables of relocated integration points was only defined for the case of isotropic hardening. This algorithm must be extended to make the adaptive strategy applicable in simulations in which advanced hardening laws are used. To increase the efficiency of the numerical integration even further it is recommended to investigate the possibility of making the number of through-thickness integration points variable. Only few points are needed for the accurate prediction of springback in deformation regimes that produce no elastic-plastic interfaces.

APPENDIX

A

CHARACTERISTIC COMPONENTS

This appendix presents three sheet metal parts which were used to investigate the sensitivity of springback prediction to various physical and numerical factors. The description of geometrical, process and material parameters is given. Unless indicated otherwise, all simulations of stamping of these components described in the main text are performed using the materials defined below.

A.1 Component 1

The unconstrained cylindrical bending test was proposed as a benchmark problem for the NUMISHEET 2002 conference [22]. The main aim of this benchmark was to investigate the springback and contact behaviour. The geometrical layout of the test problem is given in Figure A.1. The initial and final positions of the punch relative to the die are also illustrated in this figure. At the outset, the punch just touches the sheet, whose lower side contacts the upper side of the die. The geometrical parameters of the problem are summarized in Table A.1.

Table A.1: Geometrical, process and material parameters.

Model parameter	**[mm]**	**Sheet metal**	
Punch radius, $R1$	23.5	Young's modulus, GPa	70.5
Die radius, $R2$	25.0	Poisson's ratio	0.342
Die shoulder, $R3$	4.0	YS, MPa	194.1
Width of tools	50.0	R_0, R_{45}, R_{90}	1, 1, 1
Initial length of sheet	120.0	C-value, MPa	550.4
Sheet thickness	1.0	n-value	0.223
Sheet width, w	30.0		
Punch stroke	28.5		

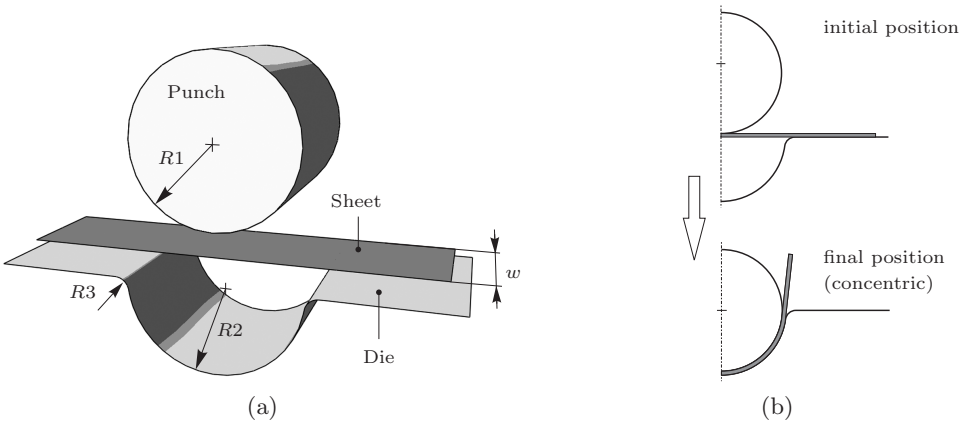

Figure A.1: Unconstrained cylindrical bending: a) geometry of tools; b) definition of the punch stroke.

An aluminium alloy 6111-T4 was used in the FE simulations of this problem and its properties can be found in Table A.1. These parameters and the value of the coefficient of friction ($\mu = 0.1348$) were taken from the benchmark specifications. Since the material model was assumed isotropic, the parameters obtained from a uniaxial experiment on a sample aligned with the rolling direction were used.

Angle $ABCD$ defined in Figure 2.10(b) was used to measure the amount of springback. This angle was reported before and after the springback at the maximum punch displacement. Default settings which were used in the numerical analyses with the FE codes Abaqus/Standard and DiekA are summarised below:

- the tools were considered perfectly rigid and the contact stiffness of 200MPa/mm was specified;
- 4-node shell element with reduced integration (S4R, [97]) was used in Abaqus/Standard. The discrete shear triangles (see for details in [154]) were used to describe the blank in DiekA. Typical element length of 2mm was chosen;
- the tools were represented by analytical surfaces;
- implicit solution procedure was used;
- gradual tool release method was employed in Abaqus/Standard. Instantaneous tool release was used in DiekA simulations;
- friction between the blank and tools was described using the Coulomb friction model;
- the stress-strain relation was represented using the Nadai hardening.

A.2 Component 2

The second component - scaled-down car roof - was provided by Corus RD&T. Main geometrical parameters of the test are shown in Figure A.2. The bottom of the punch is doubly curved. The radius of curvature along the $x-$symmetry axis is 4000mm and along the $y-$symmetry axis is 1000mm. The material of the blank is high strength steel, its thickness is 0.6mm and the in-plane dimensions are 300×500mm. Material and process parameters used in the simulations of this test are provided in Table A.2. The default settings of the numerical set-up are listed below:

- a quarter of the blank was used in the simulations;
- the tools were represented by analytical surfaces. They were considered perfectly rigid and the contact stiffness of 100MPa/mm was specified;
- the discrete shear triangular elements were used to describe the blank with the typical element length of 2.5mm;
- gradual tool release method was employed;
- friction between the blank and tools was described using the Coulomb friction model;

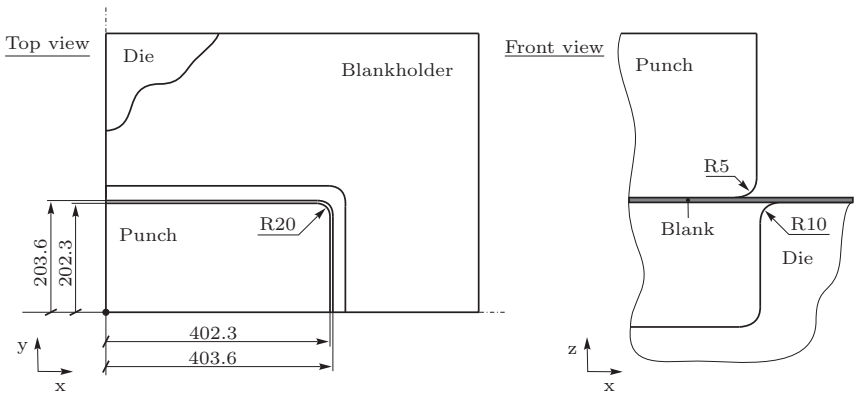

Figure A.2: Geometry of the scaled-down car roof. All dimensions are in millimeters.

Table A.2: Scaled-down car roof. Material and process parameters.

Process parameters		Sheet metal	
Punch stroke, mm	21	Young's modulus, GPa	200
Blankholder force, kN	400	Poisson's ratio	0.3
Friction coefficient	0.13	YS, MPa	277
		R_0, R_{45}, R_{90}	0.981, 1.718, 1.540
		C-value, MPa	645
		n-value	0.18

- Hill'48 yield function with isotropic hardening was used to describe the material behaviour. The stress-strain relation was represented using the Nadai hardening.

A.3 Component 3

The schematic illustration of the draw bending test, used as the NUMISHEET 1993 benchmark problem is shown in Figure A.3. The initial blank size is 350×35mm.

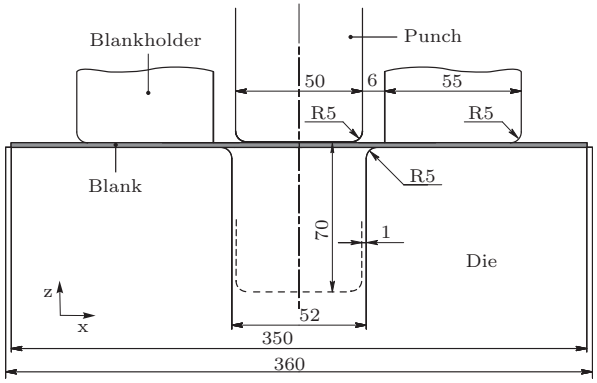

Figure A.3: Front view of the draw bending test. All dimensions are in millimeters.

The blank is made of mild steel and its thickness is 0.78mm. Material and process parameters can be found in Table A.3. In the numerical analysis the material behaviour was described using the Hill'48 yield function with isotropic hardening. Nadai law was used to represent the stress-strain relation. Discrete Kirchhoff triangular element with 7 integration points through the thickness was used to describe the blank. The typical element length in the uniform mesh was 0.79mm. Due to symmetry, only a quarter of the blank was simulated. The tools were described by means of analytical surfaces and the Coulomb model was used to represent friction between the blank and tools. The tools were considered to be undeformable and the contact stiffness of 300MPa/mm was chosen. Gradual tool release method was used during the springback step to imitate the realistic unloading procedure.

Table A.3: Draw bending. Material and process parameters.

Process parameters		Sheet metal	
Punch stroke, mm	70	Young's modulus, GPa	206
Blankholder force, kN	19.6	Poisson's ratio	0.3
Friction coefficient	0.144	YS, MPa	173.1
		R_0, R_{45}, R_{90}	1.79, 1.51, 2.27
		C-value, MPa	565.32
		n-value	0.235

APPENDIX

B

EQUATIONS FOR STRESS RESULTANTS

Equations of stress resultants in plane strain stretch bending are derived in this appendix.

Analytically solving the integral from Equation (2.26) it can be shown that the contribution of elastic stress to the total tension is zero.

$$\begin{aligned} T^e &= \int_{z_2}^{z_1} E' \left(\frac{z+a}{\rho}\right) dz = \frac{E'}{\rho} \int_{-a-b_2}^{-a+b_1} (z+a)\, dz = \\ &= \frac{E'}{\rho} \left(\frac{z^2}{2} \Big|_{-a-b_2}^{-a+b_1} + a\, z \Big|_{-a-b_2}^{-a+b_1} \right) = \\ &= \frac{E'}{\rho} \left(\frac{(-a+b_1)^2 - (a+b_2)^2}{2} + a\,(-a+b_1) + a\,(a+b_2) \right) = \\ &= \frac{E'}{\rho} \left(\frac{a^2 - 2ab_1 + b_1^2 - a^2 - 2ab_2 - b_2^2}{2} - a^2 + ab_1 + a^2 + ab_2 \right) = \\ &= \frac{E'}{\rho} \frac{b_1^2 - b_2^2}{2} = 0 \end{aligned} \tag{B.1}$$

The tension caused by the plastic stress can be derived by solving Equation (2.27):

$$T_T^p = \int_{z_1}^{\frac{t}{2}} C' \left(\varepsilon_0 + \frac{z+a}{\rho} - \frac{S_0}{E'} \right)^n dz = \int_{-a+b_1}^{\frac{t}{2}} C' \left(\varepsilon_0 + \frac{z+a}{\rho} - \frac{S_0}{E'} \right)^n dz$$

Let u be a new integration variable, then:

$$\begin{aligned} u &= \varepsilon_0 + \frac{z+a}{\rho} - \frac{S_0}{E'} \quad \Rightarrow \quad \frac{z+a}{\rho} = u + \frac{S_0}{E'} - \varepsilon_0 \quad \Rightarrow \\ z &= u\,\rho + \frac{S_0\,\rho}{E'} - \varepsilon_0\,\rho - a \end{aligned} \tag{B.2}$$

and

$$dz = \rho\, du$$

lower integration limit

$$u_1 = \varepsilon_0 + \frac{-a + b_1 + a}{\rho} - \frac{S_0}{E'} = \varepsilon_0 + \frac{b_1}{\rho} - \frac{S_0}{E'} = \varepsilon_0$$

upper integration limit

$$u_2 = \varepsilon_0 + \frac{\frac{t}{2} + a}{\rho} - \frac{S_0}{E'}$$

Hence, the tension T_T^p becomes:

$$\begin{aligned} T_T^p &= \int_{u_1}^{u_2} C'\, u^n\, \rho\, du = C'\, \rho\, \frac{u^{n+1}}{n+1}\Big|_{u_1}^{u_2} = \\ &= \frac{C'\, \rho}{n+1} \left(\left(\varepsilon_0 + \frac{\frac{t}{2} + a}{\rho} - \frac{S_0}{E'} \right)^{n+1} - \varepsilon_0^{n+1} \right) \end{aligned} \tag{B.3}$$

Solving Equation (2.28) gives the expression for the compressive force caused by the plastic stress:

$$T_C^p = -\int_{-\frac{t}{2}}^{z_2} C' \left(\varepsilon_0 + \left| \frac{z + a}{\rho} + \frac{S_0}{E'} \right| \right)^n dz = -\int_{-\frac{t}{2}}^{-a-b_2} C' \left(\varepsilon_0 + \left| \frac{z + a}{\rho} + \frac{S_0}{E'} \right| \right)^n dz$$

Let u be a new integration variable:

$$u = \frac{z + a}{\rho} + \frac{S_0}{E'} \quad \Rightarrow \quad \frac{z + a}{\rho} = u - \frac{S_0}{E'} \quad \Rightarrow \quad z = u\, \rho - \frac{S_0\, \rho}{E'} - a$$

and

$$dz = \rho\, du$$

lower integration limit

$$u_1 = \frac{-\frac{t}{2} + a}{\rho} + \frac{S_0}{E'}$$

upper integration limit

$$u_2 = \frac{-a - b_2 + a}{\rho} + \frac{S_0}{E'} = -\frac{b_2}{\rho} + \frac{S_0}{E'} = 0$$

Hence, the compressive force T_C^p becomes:

$$\begin{aligned} T_C^p &= -\int_{u_1}^{u_2} C' \left(\varepsilon_0 + |u| \right)^n \rho\, du = -C'\, \rho\, \frac{\left(\varepsilon_0 + |u| \right)^{n+1}}{n+1}\Big|_{u_1}^{u_2} = \\ &= -\frac{C'\, \rho}{n+1} \left(\varepsilon_0^{n+1} - \left(\varepsilon_0 + \left| \frac{-\frac{t}{2} + a}{\rho} + \frac{S_0}{E'} \right|^{n+1} \right) \right) \end{aligned} \tag{B.4}$$

Closed form solution of Equation (2.30) gives the elastic stress contribution to the total bending moment

$$\begin{aligned}
M^e &= \int_{z_2}^{z_1} E'\left(\frac{z+a}{\rho}\right) z\,dz = \frac{E'}{\rho}\int_{-a-b_2}^{-a+b_1} (z^2+az)\,dz = \\
&= \frac{E'}{\rho}\Big(\frac{z^3}{3}\Big|_{-a-b_2}^{-a+b_1} + \frac{az^2}{2}\Big|_{-a-b_2}^{-a+b_1}\Big) = \\
&= \frac{E'}{\rho}\Big(\frac{(-a+b_1)^3+(a+b_2)^3}{3} + \frac{a\big((-a+b_1)^2-(a+b_2)^2\big)}{2}\Big) = \\
&= \frac{E'}{\rho}\Big(\frac{-a^3+3a^2b_1-3ab_1^2+b_1^3+a^3+3a^2b_2+3ab_2^2+b_2^3}{3} + \\
&+ \frac{a^3-2a^2b_1+ab_1^2-a^3-2a^2b_2-ab_2^2}{2}\Big) = \\
&= \frac{E'}{\rho}\Big(\frac{3a^2b_1-3ab_1^2+b_1^3+3a^2b_2+3ab_2^2+b_2^3}{3} + \\
&+ \frac{ab_1^2-2a^2b_1-2a^2b_2-ab_2^2}{2}\Big) = \frac{E'}{\rho}\Big(\frac{-3ab_1^2+2b_1^3+3ab_2^2+2b_2^3}{6}\Big) \qquad \text{(B.5)}
\end{aligned}$$

Recalling that $b_2 = b_1$, the elastic moment becomes:

$$M^e = \frac{2E'}{3\rho}b_1^3 = \frac{2E'}{3\rho}\Big(\frac{S_0\rho}{E'}\Big)^3 = \frac{2S_0^3\rho^2}{3E'^2} \qquad \text{(B.6)}$$

The part of the total bending moment caused by the plastic stress in the region of tension becomes:

$$M_T^p = \int_{z_1}^{\frac{t}{2}} C'\Big(\varepsilon_0 + \frac{z+a}{\rho} - \frac{S_0}{E'}\Big)^n z\,dz = \int_{-a+b_1}^{\frac{t}{2}} C'\Big(\varepsilon_0 + \frac{z+a}{\rho} - \frac{S_0}{E'}\Big)^n z\,dz$$

Let u be a new integration variable:

$$u = \varepsilon_0 + \frac{z+a}{\rho} - \frac{S_0}{E'} \quad \Rightarrow \quad \frac{z+a}{\rho} = u + \frac{S_0}{E'} - \varepsilon_0 \quad \Rightarrow \quad z = u\,\rho + \frac{S_0\,\rho}{E'} - \varepsilon_0\,\rho - a$$

and

$$dz = \rho\,du$$

lower integration limit

$$u_1 = \varepsilon_0 + \frac{-a+b_1+a}{\rho} - \frac{S_0}{E'} = \varepsilon_0 + \frac{b_1}{\rho} - \frac{S_0}{E'} = \varepsilon_0$$

upper integration limit

$$u_2 = \varepsilon_0 + \frac{\frac{t}{2}+a}{\rho} - \frac{S_0}{E'}$$

Hence, the moment M_T^p becomes:

$$\begin{aligned} M_T^p &= \int_{u_1}^{u_2} C'\,u^n\left(u\,\rho+\frac{S_0\,\rho}{E'}-\varepsilon_0\,\rho-a\right)\rho\,du = \\ &= C'\,\rho\Big(\int_{u_1}^{u_2}\rho\,u^{n+1}\,du+\int_{u_1}^{u_2}\left(\frac{S_0\,\rho}{E'}-\varepsilon_0\,\rho-a\right)u^n\,du\Big) = \\ &= C'\,\rho\Big(\frac{\rho}{n+2}\,u^{n+2}\Big|_{u_1}^{u_2}+\left(\frac{S_0\,\rho}{E'}-\varepsilon_0\,\rho-a\right)\frac{u^{n+1}}{n+1}\Big|_{u_1}^{u_2}\Big) = \\ &= C'\,\rho\Big(\frac{\rho}{n+2}\Big(\Big(\frac{\frac{t}{2}+a}{\rho}-\frac{S_0}{E'}+\varepsilon_0\Big)^{n+2}-\varepsilon_0^{n+2}\Big)+\left(\frac{S_0\,\rho}{E'}-\varepsilon_0\,\rho-a\right)\times \\ &\times\ \frac{1}{n+1}\Big(\Big(\frac{\frac{t}{2}+a}{\rho}-\frac{S_0}{E'}+\varepsilon_0\Big)^{n+1}-\varepsilon_0^{n+1}\Big)\Big) \end{aligned} \tag{B.7}$$

Solving analytically Equation (2.32) one obtains the expression for the part of the total bending moment in the compression region:

$$M_C^p = -\int_{-\frac{t}{2}}^{z_2} C'\Big(\varepsilon_0+\Big|\frac{z+a}{\rho}+\frac{S_0}{E'}\Big|\Big)^n\,z\,dz = -\int_{-\frac{t}{2}}^{-a-b_2} C'\Big(\varepsilon_0+\Big|\frac{z+a}{\rho}+\frac{S_0}{E'}\Big|\Big)^n\,z\,dz$$

Let u be a new integration variable:

$$u=\frac{z+a}{\rho}+\frac{S_0}{E'} \quad\Rightarrow\quad \frac{z+a}{\rho}=u-\frac{S_0}{E'} \quad\Rightarrow\quad z=u\,\rho-\frac{S_0\,\rho}{E'}-a$$

and

$$dz=\rho\,du$$

lower integration limit

$$u_1=\frac{-\frac{t}{2}+a}{\rho}+\frac{S_0}{E'}$$

upper integration limit

$$u_2=\frac{-a-b_2+a}{\rho}+\frac{S_0}{E'}=-\frac{b_2}{\rho}+\frac{S_0}{E'}=0$$

Hence, the moment M_C^p becomes:

$$\begin{aligned} M_C^p &= -\int_{u_1}^{u_2} C'\left(\varepsilon_0+|u|\right)^n\Big(u\,\rho-\frac{S_0\,\rho}{E'}-a\Big)\rho\,du = \\ &= -C'\,\rho\left(\int_{u_1}^{u_2}\left(\varepsilon_0+|u|\right)^n u\,\rho\,du-\Big(\frac{S_0\,\rho}{E'}+a\Big)\int_{u_1}^{u_2}\left(\varepsilon_0+|u|\right)^n du\right) = \\ &= -C'\,\rho\left(\frac{(n+1)u-\varepsilon_0}{(n+1)(n+2)}\left(\varepsilon_0+|u|\right)^{n+1}\Big|_{u_1}^{u_2}-\Big(\frac{S_0\,\rho}{E'}+a\Big)\times\right. \end{aligned} \tag{B.8}$$

$$\times \quad \frac{\left(\varepsilon_0 + |u|\right)^{n+1}}{n+1}\Bigg|_{u_1}^{u_2}\Bigg) = -C'\,\rho\Bigg(\frac{-\varepsilon_0^{n+2}}{(n+1)(n+2)} - \frac{(n+1)\Big(\frac{-\frac{t}{2}+a}{\rho} + \frac{S_0}{E'}\Big) - \varepsilon_0}{(n+1)(n+2)} \times$$

$$\times \quad \Big(\varepsilon_0 + \Big|\frac{-\frac{t}{2}+a}{\rho} + \frac{S_0}{E'}\Big|\Big)^{n+1} - \Big(\frac{S_0\,\rho}{E'} + a\Big)\Big(\frac{\varepsilon_0^{n+1}}{n+1} - \frac{\Big(\varepsilon_0 + \Big|\frac{-\frac{t}{2}+a}{\rho} + \frac{S_0}{E'}\Big|\Big)^{n+1}}{n+1}\Big)\Bigg) \tag{B.9}$$

APPENDIX

C

GENERAL DESCRIPTION OF KIRCHHOFF ELEMENT

Main definitions of the Kirchhoff plate bending theory are given in this appendix. For simplicity of explanation the following description is restricted to small elastic deformations. The extension to plastic deformations is possible if displacements and strains are regarded as small increments. The deformation of a plate can be divided into a membrane part and a bending part. If one considers the membrane part, displacements of the plate are defined using values of the mid-plane [126]:

$$\left\{ \begin{array}{c} u \\ v \\ w \end{array} \right\} = \left\{ \begin{array}{c} u^{mp}(x,y) \\ v^{mp}(x,y) \\ w^{mp}(x,y) \end{array} \right\} \tag{C.1}$$

Where u, v and w are the displacements in $x-, y-$ and $z-$ directions correspondingly and superscript mp denotes that the displacements of the mid-plane are considered. The strains due to these displacements can be found from:

$$\left\{ \begin{array}{c} \varepsilon_{xx} \\ \varepsilon_{yy} \\ \varepsilon_{zz} \\ \gamma_{xy} \end{array} \right\} = \left\{ \begin{array}{c} \frac{\partial u}{\partial x} \\ \frac{\partial v}{\partial y} \\ \frac{\partial w}{\partial z} \\ \frac{\partial u}{\partial y} + \frac{\partial v}{\partial x} \end{array} \right\} = \left\{ \begin{array}{c} u,_x^{mp} \\ v,_y^{mp} \\ f(\varepsilon_{xx}, \varepsilon_{yy}) \\ u,_y^{mp} + v,_x^{mp} \end{array} \right\} \tag{C.2}$$

The thickness-direction strain ε_{zz} cannot be derived from the kinematic relations. For elastic deformations it is found using constitutive relations and the in-plane components. For example, for isotropic elastic material and in case of the plane stress state, the thickness-direction strain becomes:

$$\varepsilon_{zz}^e = -\frac{\nu}{1-\nu}(\varepsilon_{xx}^e + \varepsilon_{yy}^e) \tag{C.3}$$

In case of plastic deformations the thickness strain is found from the incompressibility condition:

$$\varepsilon_{zz}^p = -\varepsilon_{xx}^p - \varepsilon_{yy}^p \tag{C.4}$$

When considering only the bending part of the deformation, the vector of plate displacements can be written as [126]:

$$\left\{ \begin{array}{c} u \\ v \\ w \end{array} \right\} = \left\{ \begin{array}{c} 0 \\ 0 \\ w^{mp}(x,y) \end{array} \right\} + z \cdot \left\{ \begin{array}{c} \theta_y \\ -\theta_x \\ 0 \end{array} \right\} \tag{C.5}$$

Variables θ_x and θ_y are rotations about x and y axes and w is the lateral deflection of the plate side. For small displacements and rotations the vector of strains due to the bending deformation:

$$\left\{ \begin{array}{c} \varepsilon_{xx} \\ \varepsilon_{yy} \\ \varepsilon_{zz} \\ \gamma_{xy} \\ \gamma_{xz} \\ \gamma_{yz} \end{array} \right\} = \left\{ \begin{array}{c} \frac{\partial u}{\partial x} \\ \frac{\partial v}{\partial y} \\ \frac{\partial w}{\partial z} \\ \frac{\partial u}{\partial y} + \frac{\partial v}{\partial x} \\ \frac{\partial u}{\partial z} + \frac{\partial w}{\partial x} \\ \frac{\partial v}{\partial z} + \frac{\partial w}{\partial y} \end{array} \right\} = \left\{ \begin{array}{c} 0 \\ 0 \\ f(\varepsilon_{xx}, \varepsilon_{yy}) \\ 0 \\ w,_x^{mp} + \theta_y \\ w,_y^{mp} - \theta_x \end{array} \right\} + z \cdot \left\{ \begin{array}{c} \theta_{y,x} \\ -\theta_{x,y} \\ 0 \\ \theta_{y,y} - \theta_{x,x} \\ 0 \\ 0 \end{array} \right\} \tag{C.6}$$

Combining Equations (C.2) and (C.6) one obtains the complete vector of strains for a plate deformed in bending and tension:

$$\left\{ \begin{array}{c} \varepsilon_{xx} \\ \varepsilon_{yy} \\ \varepsilon_{zz} \\ \gamma_{xy} \\ \gamma_{xz} \\ \gamma_{yz} \end{array} \right\} = \left\{ \begin{array}{c} u,_x^{mp} \\ v,_y^{mp} \\ f(\varepsilon_{xx}, \varepsilon_{yy}) \\ u,_y^{mp} + v,_x^{mp} \\ w,_x^{mp} + \theta_y \\ w,_y^{mp} - \theta_x \end{array} \right\} + z \cdot \left\{ \begin{array}{c} \theta_{y,x} \\ -\theta_{x,y} \\ 0 \\ \theta_{y,y} - \theta_{x,x} \\ 0 \\ 0 \end{array} \right\} \tag{C.7}$$

The Kirchhoff plate bending theory states that the transverse shear strains must be equal to zero:

$$\left\{ \begin{array}{c} \gamma_{xz} \\ \gamma_{yz} \end{array} \right\} = \left\{ \begin{array}{c} w,_x^{mp} + \theta_y \\ w,_y^{mp} - \theta_x \end{array} \right\} = \left\{ \begin{array}{c} 0 \\ 0 \end{array} \right\} \Rightarrow \left\{ \begin{array}{c} \theta_y \\ \theta_x \end{array} \right\} = \left\{ \begin{array}{c} -w,_x^{mp} \\ w,_y^{mp} \end{array} \right\} \tag{C.8}$$

Taking into account the Kirchhoff constraints (C.8), the complete vector of strains becomes:

$$\left\{ \begin{array}{c} \varepsilon_{xx} \\ \varepsilon_{yy} \\ \varepsilon_{zz} \\ \gamma_{xy} \\ \gamma_{xz} \\ \gamma_{yz} \end{array} \right\} = \left\{ \begin{array}{c} u,_x^{mp} \\ v,_y^{mp} \\ f(\varepsilon_{xx}, \varepsilon_{yy}) \\ u,_y^{mp} + v,_x^{mp} \\ 0 \\ 0 \end{array} \right\} - z \cdot \left\{ \begin{array}{c} w,_{xx}^{mp} \\ w,_{yy}^{mp} \\ 0 \\ 2w,_{xy}^{mp} \\ 0 \\ 0 \end{array} \right\} \tag{C.9}$$

This equation can be abbreviated as:

$$\{\boldsymbol{\varepsilon}\} = \{\boldsymbol{\eta}\} - z \cdot \{\boldsymbol{\kappa}\} \tag{C.10}$$

APPENDIX

D

RESIDUAL STRESS DISTRIBUTION

To derive the equation that defines the residual stress distribution, the plane strain bending problem, described in Section 2.2.1, is considered. For simplicity of explanation, an elastic, perfectly plastic material is chosen. When the material is deformed in pure bending, the distribution of the total circumferential strain can be found from Equation (2.8):

$$\varepsilon_\theta = \frac{z}{\rho} \tag{D.1}$$

where z is the through-thickness coordinate and ρ is the bending radius. Equations (2.10) and (2.11) can be used to find the stress distribution in the regions of elastic and plastic deformation:

$$\sigma_\theta^e = \frac{E}{1-\nu^2}\frac{z}{\rho}, \qquad \sigma_\theta^p = S_0 \tag{D.2}$$

where $S_0 = 2/\sqrt{3}\sigma_{\mathrm{f}(0)}$ is the initial plane strain flow stress and $\sigma_{\mathrm{f}(0)}$ is the initial uniaxial yield stress.

Equation (2.29) can be used to find the bending moment per unit width of a sheet material during the deformation. For the specific case, shown in Figure D.1(a), there is no elastic zone in the stress profile and the bending moment becomes:

$$M = \frac{S_0 t^2}{4} \tag{D.3}$$

During an elastic unloading the circumferential stress decreases in value. This causes the change of the bending moment which, from Equation (2.34), is equal to:

$$\Delta M = \frac{t^3}{12}\frac{\Delta\sigma_\theta}{z} \tag{D.4}$$

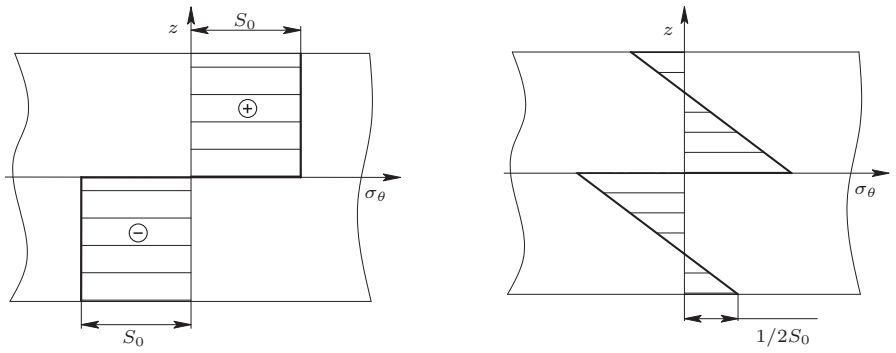

(a) bending (b) elastic unloading

Figure D.1: Through-thickness stress profiles for rigid, perfectly plastic material after bending and elastic unloading.

The change of the circumferential stress becomes:

$$\Delta\sigma_\theta = -\frac{12z}{t^3}M = -3S_0\frac{z}{t} \tag{D.5}$$

Let σ_A and σ_B be values of the circumferential stress during the loading and the elastic unloading. Then, the stress in a through-thickness point after the unloading can be found as follows:

$$\sigma_B = \sigma_A + \Delta\sigma_\theta = \sigma_A - 3S_0\frac{z}{t} = S_0 - 3S_0\frac{z}{t} \tag{D.6}$$

The through-thickness stress profile after the elastic unloading is shown in Figure D.1(b). The line $c-d$ (see Figure 4.8) can be described by means of Equation (D.6) and for $z=0$ this line intersects the neutral axis at the yield stress point.

Based on similar considerations it is possible to define the point of intersection of the lines $a-b$ and $c-d$ for a material with linear hardening. Figure D.2 shows a typical through-thickness stress distribution which can be found in the material which is bent and unbent without tension. Due to the symmetry, only the upper part of the cross-section is shown. Again, from Equations (2.10) and (2.11) the stresses in the elastic and plastic regions can be written as follows:

$$\sigma_\theta^e = E'\frac{z}{\rho}, \qquad \sigma_\theta^p = S_0 + E_t\Big(\frac{z}{\rho} - \frac{S_0}{E'}\Big) \tag{D.7}$$

In the latter equation E_t is the slope of the stress-strain curve in the region of plastic deformation and $E' = E/(1-\nu^2)$. The point of intersection of the line $a-b$ with the neutral line can be found by substituting $z=0$ into the last equation:

$$\sigma_\theta^p = S_0\Big(1 - \frac{E_t}{E'}\Big) \tag{D.8}$$

Using Equation (D.5) the line $c-d$ of the stress profile can be defined by:

$$\sigma_B = \sigma_A + \Delta\sigma_\theta = S_0 + E_t\Big(\frac{z}{\rho} - \frac{S_0}{E'}\Big) - \frac{12z}{t^3}M \tag{D.9}$$

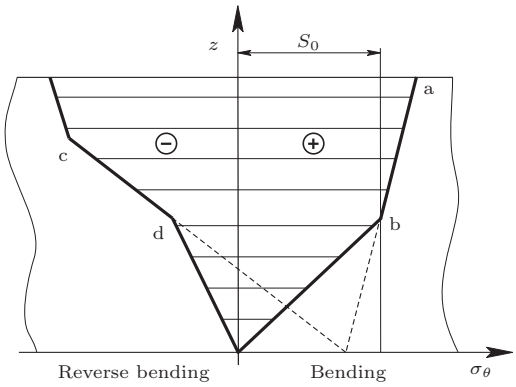

Figure D.2: Stress distribution after bending and reverse bending without tension.

This equation shows that if $z = 0$ the lines $a - b$ and $c - d$ intersect the neutral line at the same point, namely at the point where the stress is equal to $S_0\left(1 - E_t/E'\right)$.

APPENDIX

E

FORMULAE FOR INTEGRATION WITH UNEQUALLY SPACED POINTS

In this appendix formulae for Simpson's and spline integration with unequally distributed sampling points are defined. Initially, it is assumed that $I = \int_a^b f(x)\,dx$ is an integral to evaluate and $x_0, x_1, \ldots, x_n$ for $n \geq 1$ is a set of abscissas unequally spaced on the interval $[a, b]$. These integration points break the complete interval into n subintervals. $f(x_0), f(x_1), \ldots, f(x_n)$ are the integrand's values at the corresponding integration points.

E.1 Simpson's integration

Simpson's rule uses the second order polynomial for the approximation of the integrand $f(x)$. Therefore at least 3 integration points must be available on the interval $[a, b]$ which means that $n \geq 2$ and even. Lagrange formula for interpolating polynomial (4.5) can be used to define a quadratic function $P_j(x)$ that approximates the integrand $f(x)$ at three consecutive integration points $x_{2j-2}, x_{2j-1}, x_{2j}$ for $j = 1, 2, \ldots, n/2$:

$$\begin{aligned} P_j(x) &= \frac{(x - x_{2j-1})(x - x_{2j})}{(x_{2j-2} - x_{2j-1})(x_{2j-2} - x_{2j})} f(x_{2j-2}) + \\ &+ \frac{(x - x_{2j-2})(x - x_{2j})}{(x_{2j-1} - x_{2j-2})(x_{2j-1} - x_{2j})} f(x_{2j-1}) + \\ &+ \frac{(x - x_{2j-2})(x - x_{2j-1})}{(x_{2j} - x_{2j-2})(x_{2j} - x_{2j-1})} f(x_{2j}) \end{aligned} \tag{E.1}$$

Carrying out transformations this equation can be written in the following simple form:

$$P_j(x) = k_j x^2 + l_j x + m_j \tag{E.2}$$

where k_j, l_j, m_j are coefficients of the polynomial:

$$\begin{aligned} k_j &= \frac{f(x_{2j-2})}{(x_{2j-2}-x_{2j-1})(x_{2j-2}-x_{2j})} + \frac{f(x_{2j-1})}{(x_{2j-2}-x_{2j-1})(x_{2j}-x_{2j-1})} + \\ &+ \frac{f(x_{2j})}{(x_{2j-2}-x_{2j})(x_{2j-1}-x_{2j})} \end{aligned} \tag{E.3}$$

$$\begin{aligned} l_j &= -\frac{(x_{2j-1}+x_{2j})f(x_{2j-2})}{(x_{2j-2}-x_{2j-1})(x_{2j-2}-x_{2j})} - \frac{(x_{2j-2}+x_{2j})f(x_{2j-1})}{(x_{2j-2}-x_{2j-1})(x_{2j}-x_{2j-1})} - \\ &- \frac{(x_{2j-2}+x_{2j-1})f(x_{2j})}{(x_{2j-2}-x_{2j})(x_{2j-1}-x_{2j})} \end{aligned} \tag{E.4}$$

$$\begin{aligned} m_j &= \frac{x_{2j-1}\,x_{2j}\,f(x_{2j-2})}{(x_{2j-2}-x_{2j-1})(x_{2j-2}-x_{2j})} + \frac{x_{2j-2}\,x_{2j}\,f(x_{2j-1})}{(x_{2j-2}-x_{2j-1})(x_{2j+2}-x_{2j-1})} + \\ &+ \frac{x_{2j-2}\,x_{2j-1}\,f(x_{2j})}{(x_{2j-2}-x_{2j})(x_{2j-1}-x_{2j})} \end{aligned} \tag{E.5}$$

The formula for Simpson's integration with unequally spaced points can then be derived by adding the integrals of all approximating functions $P_j(x)$:

$$\begin{aligned} I_n(f) &= \sum_{j=1}^{n/2} \int_{x_{2j-2}}^{x_{2j}} P_j(x)\,dx = \sum_{j=1}^{n/2} \int_{x_{2j-2}}^{x_{2j}} (k_j x^2 + l_j x + m_j)\,dx = \\ &= \sum_{j=1}^{n/2} \Big(\frac{k_j x^3}{3}\Big|_{x_{2j-2}}^{x_{2j}} + \frac{l_j x^2}{2}\Big|_{x_{2j-2}}^{x_{2j}} + m_j x\Big|_{x_{2j-2}}^{x_{2j}} \Big) = \\ &= \sum_{j=1}^{n/2} \Big(\frac{k_j}{3}(x_{2j}^3 - x_{2j-2}^3) + \frac{l_j}{2}(x_{2j}^2 - x_{2j-2}^2) + m_j(x_{2j} - x_{2j-2}) \Big) \\ &\qquad\qquad \text{for} \quad j = 1, 2, ..., n/2 \end{aligned} \tag{E.6}$$

Equations that can be used to update the weights of integration points are defined below. For simplicity of explanation let $a = x_0, x_1, x_2, x_3$ and $x_4 = b$ be a set of unequally spaced abscissas with $f(x_0), f(x_1), f(x_2), f(x_3)$ and $f(x_4)$ their corresponding functional values. To calculate numerically the integral $I = \int_a^b f(x)dx$ its integrand $f(x)$ is approximated by two quadratic polynomials $P_1(x)$ and $P_2(x)$ which are defined at the integration points x_0, x_1, x_2 and x_2, x_3, x_4. The integral I can then be approximated by a sum of two integrals:

$$I_n(f) = \int_{x_0}^{x_2} P_1(x)dx + \int_{x_2}^{x_4} P_2(x)dx \tag{E.7}$$

Using the Lagrange formula for interpolating polynomial:

$$\begin{aligned} P_1(x) &= \frac{(x-x_1)(x-x_2)}{(x_0-x_1)(x_0-x_2)}f(x_0) + \frac{(x-x_0)(x-x_2)}{(x_1-x_0)(x_1-x_2)}f(x_1) + \\ &+ \frac{(x-x_0)(x-x_1)}{(x_2-x_0)(x_2-x_1)}f(x_2) \\ P_2(x) &= \frac{(x-x_3)(x-x_4)}{(x_2-x_3)(x_2-x_4)}f(x_2) + \frac{(x-x_2)(x-x_4)}{(x_3-x_2)(x_3-x_4)}f(x_3) + \\ &+ \frac{(x-x_2)(x-x_3)}{(x_4-x_2)(x_4-x_3)}f(x_4) \end{aligned} \tag{E.8}$$

Therefore the integral I_n becomes:

$$\begin{aligned} I_n &= \int_{x_0}^{x_2} \frac{(x-x_1)(x-x_2)}{(x_0-x_1)(x_0-x_2)}f(x_0)\,dx + \int_{x_0}^{x_2} \frac{(x-x_0)(x-x_2)}{(x_1-x_0)(x_1-x_2)}f(x_1)\,dx + \\ &+ \int_{x_0}^{x_2} \frac{(x-x_0)(x-x_1)}{(x_2-x_0)(x_2-x_1)}f(x_2)\,dx + \int_{x_2}^{x_4} \frac{(x-x_3)(x-x_4)}{(x_2-x_3)(x_2-x_4)}f(x_2)\,dx + \\ &+ \int_{x_2}^{x_4} \frac{(x-x_2)(x-x_4)}{(x_3-x_2)(x_3-x_4)}f(x_3)\,dx + \int_{x_2}^{x_4} \frac{(x-x_2)(x-x_3)}{(x_4-x_2)(x_4-x_3)}f(x_4)\,dx = \\ &= w_0 f(x_0) + w_1 f(x_1) + w_2 f(x_2) + w_3 f(x_3) + w_4 f(x_4) \end{aligned} \tag{E.9}$$

where w_j for $j = 0, 4$ are the required weights. From the foregoing equation the weights can be found as follows:

$$\begin{aligned} w_0 &= \int_{x_0}^{x_2} \frac{(x-x_1)(x-x_2)}{(x_0-x_1)(x_0-x_2)}\,dx; \;\; w_1 = \int_{x_0}^{x_2} \frac{(x-x_0)(x-x_2)}{(x_1-x_0)(x_1-x_2)}\,dx; \\ w_2 &= \int_{x_0}^{x_2} \frac{(x-x_0)(x-x_1)}{(x_2-x_0)(x_2-x_1)}\,dx + \int_{x_2}^{x_4} \frac{(x-x_3)(x-x_4)}{(x_2-x_3)(x_2-x_4)}\,dx; \\ w_3 &= \int_{x_2}^{x_4} \frac{(x-x_2)(x-x_4)}{(x_3-x_2)(x_3-x_4)}\,dx; \;\; w_4 = \int_{x_2}^{x_4} \frac{(x-x_2)(x-x_3)}{(x_4-x_2)(x_4-x_3)}\,dx \end{aligned} \tag{E.10}$$

Solving these integrals one can find the expressions for the weights of the integration points. For example, the expression for w_0 becomes:

$$\begin{aligned} w_0 &= \frac{1}{(x_0-x_1)(x_0-x_2)}\Big(\frac{x^3}{3}\Big|_{x_0}^{x_2} - (x_1+x_2)\frac{x^2}{2}\Big|_{x_0}^{x_2} + x_1x_2x\Big|_{x_0}^{x_2}\Big) = \\ &= \frac{1}{(x_0-x_1)(x_0-x_2)} \times \Big(\frac{x_2^3-x_0^3}{3} - \frac{(x_1+x_2)(x_2^2-x_0^2)}{2} + x_1x_2(x_2-x_0)\Big) \end{aligned} \tag{E.11}$$

In general case, the weights of unequally spaced integration points for Simpson's rule

can be found as follows:

$$
\begin{aligned}
w_{2j-2} &= w_{2j-2} + \frac{1}{(x_{2j-2}-x_{2j-1})(x_{2j-2}-x_{2j})} \times \\
&\times \left(\frac{x_{2j}^3 - x_{2j-2}^3}{3} - (x_{2j-1}+x_{2j}) \frac{x_{2j}^2 - x_{2j-2}^2}{2} + x_{2j-1}\, x_{2j} (x_{2j} - x_{2j-2}) \right) \\
w_{2j-1} &= \frac{1}{(x_{2j-1}-x_{2j-2})(x_{2j-1}-x_{2j})} \times \\
&\times \left(\frac{x_{2j}^3 - x_{2j-2}^3}{3} - (x_{2j-2}+x_{2j}) \frac{x_{2j}^2 - x_{2j-2}^2}{2} + x_{2j-2}\, x_{2j} (x_{2j} - x_{2j-2}) \right) \\
w_{2j} &= \frac{1}{(x_{2j}-x_{2j-2})(x_{2j}-x_{2j-1})} \times \\
&\times \left(\frac{x_{2j}^3 - x_{2j-2}^3}{3} - (x_{2j-2}+x_{2j-1}) \frac{x_{2j}^2 - x_{2j-2}^2}{2} + \right. \\
&+ \left. x_{2j-2}\, x_{2j-1} (x_{2j} - x_{2j-2}) \right)
\end{aligned}
$$

$$\text{for} \quad j = 1, 2, ..., n/2 \tag{E.12}$$

E.2 Spline integration

A spline function can also be used for the approximation of the integrand $f(x)$ since it allows fitting a very smooth curve through a set of points. For $n+1$ integration points on the interval $[a, b]$ a function can be called a spline $S(x)$ of degree m if it satisfies the following conditions [138]:

- it coincides with a polynomial of degree m on each subinterval: $[x_{i-1}, x_i]$, $i = 0, 1, \ldots, n$;
- it is $m-1$ times continuously differentiable.

The general formula for integration using a natural cubic spline can be written as follows [138]:

$$
\begin{aligned}
\int_a^b S(x)\, dx &= \sum_{j=1}^{n} \frac{f(x_{j-1}) + f(x_j)}{2} h_j - \sum_{j=1}^{n} \frac{M_{j-1} + M_j}{24} h_j^3 \\
&\text{for} \quad j = 0, 1, ..., n
\end{aligned} \tag{E.13}
$$

where M_{j-1} and M_j are the second order derivatives of the spline function in the corresponding integration points and h_j is the length of the subinterval $[x_{i-1}, x_i]$. The method for calculating parameters M_{j-1} and M_j can be found in literature, see for example [120, 138].

NOMENCLATURE

Abbreviations

AIS1	adaptive integration scheme
CAD	computer aided design
GAIS	generally applicable adaptive integration scheme
NAME	normalised average moment error
POD	point of discontinuity
RME	relative moment error
YS	initial yield stress

Greek symbols

$\bar{\sigma}$	equivalent stress
$\bar{\varepsilon}^p$	equivalent plastic strain
γ	shear strain
μ	coefficient of friction
ν	Poisson's ratio
ϕ	yield condition
ρ	radius of curvature
σ_θ	circumferential stress
σ_f	uniaxial flow stress

θ	angle of bending
ε_0	pre-strain in the Nadai hardening relation
ε_θ	circumferential strain
ε_b	bending part of the circumferential strain
ε_m	circumferential strain in the mid-plane
ξ	scalar which depends on the material anisotropy parameters
ζ	natural coordinate
$\{\boldsymbol{\epsilon}\}$	error vector
$\{\boldsymbol{\eta}\}$	strain contribution of the membrane part of a deformation
$\{\boldsymbol{\kappa}\}$	strain contribution of the bending part of a deformation
$\{\boldsymbol{\sigma}\}$	stress vector
$\{\boldsymbol{\theta}\}$	nodal rotations
$\{\boldsymbol{\varepsilon}\}$	vector of total strain
q	scaling factor

Mathematical symbols

$[.]$	rectangular matrix
$[.]^T$	matrix transpose
Δ	increment
$\lvert . \rvert$	absolute value
$\{.\}$	column vector
$\lVert . \rVert_2$	Euclidean norm
$\lVert . \rVert_\infty$	∞-norm

Roman symbols

$[\boldsymbol{B}]$	strain-displacement matrix
$[\boldsymbol{D}]$	matrix of material constants
$[\boldsymbol{K}]$	tangent stiffness matrix

$[\boldsymbol{P}]$	matrix with material anisotropy parameters
$\bar{a}$	normalised shift of neutral line
$\{\boldsymbol{A}\}$	stress contribution of the membrane part of a deformation
$\{\boldsymbol{a}\}$	vector with interpolating coefficients
$\{\boldsymbol{B}\}$	stress contribution of the bending part of a deformation
$\{\boldsymbol{d}\}$	vector of nodal displacements
$\{\boldsymbol{f}^{ext}\}$	vector of external forces
$\{\boldsymbol{f}^{int}\}$	vector of internal forces
$\{\boldsymbol{M}\}$	vector of bending moments
$\{\boldsymbol{q}\}$	vector with hardening parameters
$\{\boldsymbol{r}\}$	vector of residual forces
A	element area
a	distance between the central and neutral lines
a, b	limits of integration
b, w	sheet width
b_1, b_2, m_1, m_2	through-thickness coordinates of the elastic-plastic transitions
C	material strength coefficient
E	Young's modulus
F, G, H, N	anisotropy parameters
k, l, m	coefficients of a quadratic polynomial
l	length of a line segment
M	resulting bending moment
n	number of panels, strain hardening exponent
R	ratio between width and thickness strain, tool radius
S	plane strain flow stress
T	resulting force
t	material thickness, time
u, v, w	displacements in $x, y, z-$ directions

V	element volume
w	weight factors
x, y, z	Cartesian coordinates

General subscripts and superscripts

$(.)^{e}$	elastic part
$(.)^{int}$	interpolated value
$(.)^{mp}$	mid-plane
$(.)^{p}$	plastic part
$(.)^{ref}$	reference value
$(.)^{wh}$	workhardening
$(.)^{y}$	yield
$(.)_{0}$	initial
$(.)_{1,2,3}$	principal values
$(.)_{col}$	columns of integration points
$(.)_{C}$	compression region
$(.)_{ip}$	integration points
$(.)_{it}$	iterations
$(.)_{k}$	iteration number
$(.)_{n}$	incremental step number
$(.)_{T}$	tension region
$(.)_{t}$	trial
$(.)_{y}$	yield, with respect to the y-axis

ACKNOWLEDGEMENTS

Now, when the thesis is almost finished, a very important remaining task is to acknowledge all those people who directly and indirectly contributed to my work.

This thesis is based on the results of almost four and a half years of research performed in the framework of the Strategic Research programme of the Netherlands Institute for Metals Research. I would like to thank all members of the NIMR head office for their help, understanding and organisation support. Many thanks to all industrial partners and to my former fellow researchers at the NIMR for the valuable discussions, important feedback and informal talks during the conferences and the cluster meetings.

The research was carried out at the University of Twente, section of Applied Mechanics. I would like to express the sincere gratitude to my promotor Prof. Han Huétink for his guidance, encouraging and enthusiastic support during all these years. I especially want to thank my daily supervisor, the assistant promotor and just a great person Timo Meinders. He has always been actively involved in my research and I am very grateful for his support, patience, motivation and numerous advices on various scientific and not matters.

Next I would like to express my gratitude to the people involved in the springback project for their interest, fruitful discussions, support and constructive criticism during our regular meetings: Eisso Atzema (Corus RD&T), Ewout Meijers (NIMR), Bert Rietman (INPRO), Albert Konter (NIMR), Hans Kappert (Polynorm), Marianna Avetisyan (NIMR), Roal Lingbeek (NIMR), Pascal Kömmelt (Corus RD&T) and Alpay Aydemir (NIMR).

It would have been an extremely difficult task to perform this research without the excellent working relations and a friendly atmosphere of the DiekA group. Many thanks to all permanent members of the group - Ton van den Boogaard, Bert Geijselaers, Harm Wisselink, Nico van Vliet and Herman van Corbach - for their time, valuable suggestions and interesting ideas. Special thanks to Tanja van Scherpenzeel-Gerrits and Debbie Vrieze-Zimmerman van Woesik for helping me with numerous administrative and other personal questions during my stay at the university. I also want to thank all present and past members of the section of Applied Mechanics for enriching my social life and in particular to Semih Perdahcioğlu,

Pawel Owczarek, Marieke Hannink, Didem Akçay Perdahcioğlu and Maarten van Riel for their wonderful friendship and invaluable support in difficult times. And of course, it would be a crime not to thank all my roommates: Martijn Bonte, Sophie Trichon, Wissam Assaad and Wouter Quak for informal chats, singing, organising scientific competitions and in general, for creating and supporting the great working atmosphere.

I am very grateful to all members of the reading committee - Timo Meinders, Han Huétink, Bert Geijselaers and Maarten van Riel - who carefully read the manuscript and helped me to significantly improve its contents. Additionally, I would like to thank Katrina Emmett who carried out the corrections of the English language and to Wouter Quak for the Dutch translation of the Summary.

Many personal thanks go to my family and to all my friends in Belarus for their believing in me, being proud of me and for the continuous encouragement throughout all these years. Finally, I want to thank my wife, Alla, for her understanding, patience and the indispensable support I received from her during my research career and especially during the last difficult months of writing the manuscript.

Igor Burchitz.
Rotterdam, April 2008.

ABOUT THE AUTHOR

Burchitz Igor Alexandrovich was born on 21st of November 1976 in Baranovichi, Republic of Belarus. In June 1994 he finished the secondary school Gimnasia #4 in the town of Baranovichi. From September 1994 till June 1999 he studied at the Belarussian State Polytechnical Academy, faculty of Mechanical Engineering. After the graduation he was given a qualification of Mechanical Engineer. From 1999 till 2001 he was a post-graduate student at the Machine Parts group of the Belarussian State Polytechnical Academy. In 2001 he joined the post-master program at the Institute of Advanced Industrial Design Engineering in Delft University of Technology and earned his Master of Technological Design degree in September 2003. In October 2003 he joined the Netherlands Institute for Metals Research and began his doctoral study at the University of Twente in the group of Prof. J. Huétink under the daily supervision of Dr. T. Meinders. In April 2008 he prepared the manuscript concerning the research on improvement of numerical prediction of springback in sheet metal forming. From April 2008 he works as an application and support engineer at AutoForm Engineering B.V. in Krimpen aan den IJssel, the Netherlands.

Bibliography

[1] M.F. Ashby. *Materials selection in mechanical design*. Butterworth-Heinemann, 2nd edition, 1999.

[2] R. Pearce. *Sheet metal forming*. Adam Hilger, 1991.

[3] Schuler GmbH. *Metal forming handbook*. Springer, 1st edition, 1998.

[4] L.M. Smith, F. Pourboghrat, J.W. Yoon, and T.B. Stoughton, editors. *Proceedings of the 6th international conference and workshop on numerical simulation of 3D sheet metal forming processes, NUMISHEET 2005*, Detroit, MI, U.S.A., 2005.

[5] C. Wang. An industrial outlook for springback predictability, measurement reliability and compensation technology. In D.-Y. Yang, S.I. Oh, H. Huh, and Y.H. Kim, editors, *Proceedings of the 5th International Conference and Workshop on Numerical Simulation of 3D Sheet Forming Processes, NUMISHEET 2002*, pages 597–604, Jeju Island, Korea, 2002.

[6] G. Liu, Z. Lin, W. Xu, and Y. Bao. Variable blankholder force in u-shaped part forming for eliminating springback error. *Journal of Materials Processing Technology*, 120(1-3):259–264, 2002.

[7] J. Cao. Consistent and minimal springback using a stepped binder force trajectory and neural network control. *Journal of Engineering Materials and Technology, Transactions of the ASME*, 122:113 – 118, 2000.

[8] L. Gunnarsson and E. Schedin. Improving the properties of exterior body panels in automobiles using variable blank holder force. *Journal of Materials Processing Technology*, 114(2):168–173, 2001.

[9] C. Du, J. Wu, M. Militisky, J. Principe, M. Garnett, and L. Zhang. Springback control with variable binder force experiments and fea simulation. In S. Ghosh, J.M. Castro, and J.K. Lee, editors, *Proceedings of NUMIFORM 2004. Materials Processing and Design: Modeling, Simulation and Applications*, pages 970 – 976, Columbus, Ohio, 2004.

[10] L.M. Kutt, J.A. Nardiello, P.L. Ogilvie, A.B. Pifko, and J.M. Papazian. Nonlinear finite element analysis of springback. *Communications in Numerical Methods in Engineering*, 15(1):33–42, 1999.

[11] R. Lingbeek, J. Huétink, S. Ohnimus, M. Petzoldt, and J. Weiher. The development of a finite elements based springback compensation tool for sheet metal products. *Journal of Materials Processing Technology*, 169(1):115, 2005.

[12] B.D. Carleer. *Finite element analysis of deep drawing*. PhD thesis, University of Twente, 1997.

[13] T. Meinders. *Developments in numerical simulations of the real-life deep drawing process*. PhD thesis, University of Twente, 2000.

[14] A.E. Tekkaya. State-of-the-art of simulation of sheet metal forming. *Journal of Materials Processing Technology*, 103(1):14–22, 2000.

[15] A. Makinouchi. Sheet metal forming simulation in industry. *Journal of Materials Processing Technology*, 60(1-4):19–26, 1996.

[16] M. Rohleder and K. Roll. Numerical prediction of springback on a complex car part. In D.-Y. Yang, S.I. Oh, H. Huh, and Y.H. Kim, editors, *The 5th International Conference and Workshop on Numerical Simulation of 3D Sheet Forming Processes, NUMISHEET 2002*, pages 367 – 372, Jeju Island, Korea, 2002.

[17] K.P. Li, W.P. Carden, and R.H. Wagoner. Simulation of springback. *International Journal of Mechanical Sciences*, 44(1):103–122, 2002.

[18] A. Andersson. Numerical and experimental evaluation of springback in a front side member. *Journal of Materials Processing Technology*, 169(3):352, 2005.

[19] C. Du, X.M. Chen, T. Lim, T. Chang, P. Xiao, and S.-D. Liu. Correlation of fea prediction and experiments on dual-phase steel automotive rails. In J.M.A. César de Sá and A.D. Santos, editors, *Proceedings of the 9th International Conference on Numerical Methods in Industrial Forming Processes, NUMIFORM 2007*, volume 908, Porto, Portugal, 2007. AIP Conference Proceedings.

[20] E.H. Atzema, H. Kappert, A.W.A. Konter, S.E. Meijers, and T. Meinders. *Sensitivity analysis component 2: Scaled down car roof.* Netherlands Institute for Metals Research, 2005.

[21] H. Livatyali and T. Altan. Prediction and elimination of springback in straight flanging using computer aided design methods: Part 1. experimental investigations. *Journal of Materials Processing Technology*, 117(1-2):262–268, 2001.

[22] D.-Y. Yang, S.I. Oh, H. Huh, and Y.H. Kim, editors. *Proceedings of the 5th international conference and workshop on numerical simulation of 3D sheet metal forming processes, NUMISHEET 2002*, Jeju Island, Korea, 2002.

[23] H. Pijlman. *Sheet material characterisation by multi-axial experiments.* PhD thesis, University of Twente, 2001.

[24] W.D. Carden, L.M. Geng, D.K. Matlock, and R.H. Wagoner. Measurement of springback. *International Journal of Mechanical Sciences*, 44(1):79–101, 2002.

[25] R.M. Cleveland and A.K. Ghosh. Inelastic effects on springback in metals. *International Journal of Plasticity*, 18(5-6):769–785, 2002.

[26] C. Teodosiu. Some basic aspect of the constitutive modelling in sheet metal forming. In D.Banabic, editor, *Proceedings of the 8th ESAFORM conference on material forming*, volume 1, pages 239–243, Cluj-Napoca, Romania, 2005.

[27] D.-K. Leu. A simplified approach for evaluating bendability and springback in plastic bending of anisotropic sheet metals. *Journal of Materials Processing Technology*, 66(1-3):9–17, 1997.

[28] F. Pourboghrat and E. Chu. Springback in plane strain stretch/draw sheet forming. *International Journal of Mechanical Sciences*, 37(3):327, 1995.

[29] P. Xue, T.X. Yu, and E. Chu. Theoretical prediction of the springback of metal sheets after a double-curvature forming operation. *Journal of Materials Processing Technology*, 89-90:65–71, 1999.

[30] T. Meinders, A.W.A. Konter, S.E. Meijers, E.H. Atzema, and H. Kappert. A sensitivity analysis on the springback behaviour of the unconstrained bending problem. *International Journal of Forming Processes*, 9(3):365–402, 2006.

[31] D.-W. Park and S.-I. Oh. A four-node shell element with enhanced bending performance for springback analysis. *Computer Methods in Applied Mechanics and Engineering*, 193(23-26):2105–2138, 2004.

[32] I.A. Burchitz, T. Meinders, and J. Huétink. Influence of numerical parameters on springback prediction in sheet metal forming. In *Proceedings of the 9th International Conference on Material Forming, ESAFORM 2006*, pages 407–410, 2006.

[33] I.N. Chou and C. Hung. Finite element analysis and optimization on springback reduction. *International Journal of Machine Tools & Manufacture*, 39(3):517–536, 1999.

[34] S.S. Han and K.C. Park. An investigation of the factors influencing springback by empirical and simulative techniques. In *Proceedings of the 4th International Conference and Workshop on Numerical Simulation of 3D Sheet Forming Processes, NUMISHEET 1999*, pages 53–58, Besancon, France, 1999.

[35] Z. Tekiner. An experimental study on the examination of springback of sheet metals with several thicknesses and properties in bending dies. *Journal of Materials Processing Technology*, 145(1):109–117, 2004.

[36] L.C. Zhang, G. Lu, and S.C. Leong. V-shaped sheet forming by deformable punches. *Journal of Materials Processing Technology*, 63(1-3):134–139, 1997.

[37] H. Livatyali, H.C. Wu, and T. Altan. Prediction and elimination of springback in straight flanging using computer-aided design methods: Part 2: Fem predictions and tool design. *Journal of Materials Processing Technology*, 120(1-3):348–354, 2002.

[38] T. Kuwabara, Y. Asano, S. Ikeda, and H. Hayashi. An evaluation method for springback characteristics of sheet metals based on a stretch bending test. In Kergen R., Kebler L., Langerak N., Lenze F.-J., Janssen E., and Steinbeck G., editors, *Proceedings of IDDRG 2004. Forming the Future. Global Trends in Sheet Metal Forming*, pages 55 – 64, Sindelfingen, Germany, 2004.

[39] J.-T. Gau and G.L. Kinzel. An experimental investigation of the influence of the bauschinger effect on springback predictions. *Journal of Materials Processing Technology*, 108(3):369–375, 2001.

[40] J.-T. Gau and G.L. Kinzel. A new model for springback prediction in which the bauschinger effect is considered. *International Journal of Mechanical Sciences*, 43(8):1813–1832, 2001.

[41] W.L. Xu, C.H. Ma, C.H. Li, and W.J. Feng. Sensitive factors in springback simulation for sheet metal forming. *Journal of Materials Processing Technology*, 151(1-3):217–222, 2004.

[42] E. Bayraktar and S. Altintas. Square cup deep drawing and 2d-draw bending analysis of hadfield steel. *Journal of Materials Processing Technology*, 60(1-4):183–190, 1996.

[43] R.H. Wagoner. Fundamental aspects of springback in sheet metal forming. In D.-Y. Yang, S.I. Oh, H. Huh, and Y.H. Kim, editors, *Proceedings of the 5th International Conference and Workshop on Numerical Simulation of 3D Sheet Forming Processes, NUMISHEET 2002*, pages 13 – 24, Jeju Island, Korea, 2002.

[44] K. Li, L. Geng, and R.H. Wagoner. Simulation of springback: Choice of element. In M. Geiger, editor, *Advanced Technology of Plasticity 1999*, volume 3, pages 2091 – 2099, Nuremberg, Germany, 1999. Springer-Verlag.

[45] J.F. Wang, R.H. Wagoner, W.D. Carden, D.K. Matlock, and F. Barlat. Creep and anelasticity in the springback of aluminum. *International Journal of Plasticity*, 20(12):2209–2232, 2004.

[46] W. Lems. *The change of Young's modulus after deformation at low temperature and its recovery.* PhD thesis, Delft University of Technology, 1963.

[47] F. Morestin and M. Boivin. On the necessity of taking into account the variation in the young modulus with plastic strain in elastic-plastic software. *Nuclear Engineering and Design*, 162(1):107–116, 1996.

[48] I. Iwata and M. Matsui. Numerical prediction of spring-back behavior of a stamped metal sheet by considering material non-linearity during unloading. In Ken ichiro Mori, editor, *Proceedings of NUMIFORM 2001*, pages 693–698, Toyohashi, Japan, 2001.

[49] S. Thibaud, N. Boudeau, and J-C. Gelin. On the influence of the young modulus evolution on the dynamic behaviour and springback of a sheet metal forming component. In D.-Y. Yang, S.I. Oh, H. Huh, and Y.H. Kim, editors, *Proceedings of the 5th International Conference and Workshop on Numerical Simulation of 3D Sheet Forming Processes, NUMISHEET 2002*, pages 149 – 153, Jeju Island, Korea, 2002.

[50] M. Yang, Y. Akiyama, and T. Sasaki. Evaluation of change in material properties due to plastic deformation. *Journal of Materials Processing Technology*, 151(1-3):232–236, 2004.

[51] F. Yoshida, T. Uemori, and K. Fujiwara. Elastic-plastic behavior of steel sheets under in-plane cyclic tension-compression at large strain. *International Journal of Plasticity*, 18(6):633–659, 2002.

[52] L. Luo and Ghosh A. K. Elastic and inelastic recovery after plastic deformation of dqsk steel sheet. *Journal of Engineering Materials and Technology, Transactions of the ASME*, 125(3):237–246, 2003.

[53] Z. Marciniak, J.L. Duncan, and S.J. Hu. *Mechanics of sheet metal forming*. Butterworth-Heinemann, London, 2nd edition, 2002.

[54] Z.T. Zhang and S.J. Hu. Stress and residual stress distributions in plane strain bending. *International Journal of Mechanical Sciences*, 40(6):533–543, 1998.

[55] L.C. Zhang and Z. Lin. Analytical solution to springback of sheet metals stamped by a rigid punch and an elastic die. *Journal of Materials Processing Technology*, 63(1-3):49–54, 1997.

[56] H. Livatyali, C.L. Kinzel, and T. Altan. Computer aided die design of straight flanging using approximate numerical analysis. *Journal of Materials Processing Technology*, 142(2):532–543, 2003.

[57] N. Asnafi. Springback and fracture in v-die air bending of thick stainless steel sheets. *Materials & Design*, 21(3):217–236, 2000.

[58] N. Asnafi. On springback of double-curved autobody panels. *International Journal of Mechanical Sciences*, 43(1):5–37, 2001.

[59] P. Xue, T.X. Yu, and E. Chu. An energy approach for predicting springback of metal sheets after double-curvature forming, part i: Axisymmetric stamping. *International Journal of Mechanical Sciences*, 43(8):1893–1914, 2001.

[60] P. Xue, T.X. Yu, and E. Chu. An energy approach for predicting springback of metal sheets after double-curvature forming, part ii: Unequal double-curvature forming. *International Journal of Mechanical Sciences*, 43(8):1915–1924, 2001.

[61] D. Zhang, Z. Cui, X. Ruan, and Y. Li. An analytical model for predicting springback and side wall curl of sheet after u-bending. *Computational Materials Science*, 38(4):707–715, 2007.

[62] B.D. Carleer, T. Meinders, H.H. Pijlman, J. Huétink, and H. Vegter. A planar anisotropic yield function based on multi axial stress states in finite elements. In D.R.J. Owen, E. Oñate, and E. Hinton, editors, *Computational Plasticity, Fundamentals and Applications*, pages 913–920, 1997.

[63] H. Aretz. Applications of a new plane stress yield function to orthotropic steel and aluminium sheet metals. *Modelling and Simulation in Materials Science and Engineering*, 12(3):491–509, 2004.

[64] J.-W. Yoon, F. Barlat, R.E. Dick, K. Chung, and T.J. Kang. Plane stress yield function for aluminum alloy sheets - part ii: Fe formulation and its implementation. *International Journal of Plasticity*, 20(3):495–522, 2004.

[65] J.L. Alves, M.C. Oliveira, and L.F. Menezes. Springback evaluation with several phenomenological yield criteria. In *Proceedings of the 2nd International Materials Symposium*, volume 455-456 of *Materials Science Forum*, pages 732–736, Caparica, Portugal, 2004.

[66] O.-G. Lademo, O.S. Hopperstad, and M. Langseth. An evaluation of yield criteria and flow rules for aluminum alloys. *International Journal of Plasticity*, 15(2):191–208, 1999.

[67] K. Mattiasson and M. Sigvant. Material characterization and modeling for industrial sheet forming simulations. In S. Ghosh, J.M. Castro, and J.K. Lee, editors, *Proceedings of NUMIFORM 2004. Materials Processing and Design: Modeling, Simulation and Applications*, pages 875 – 880, Columbus, Ohio, 2004.

[68] H. Berg, P. Hora, and J. Reissner. Simulation of sheet metal forming processes using different anisotropic constitutive models. In J. Huétink and F.P.T. Baaijens, editors, *Proceedings of NUMIFORM 1998. Simulation of Material Processing: Theory, Methods and Applications*, pages 775 – 780, Enschede, The Netherlands, 1998.

[69] C. Gomes, O. Onipede, and M. Lovell. Investigation of springback in high strength anisotropic steels. *Journal of Materials Processing Technology*, 159(1):91–98, 2005.

[70] F. Barlat, D. Banabic, and O. Cazacu. Anisotropy in sheet metals. In D.-Y. Yang, S.I. Oh, H. Huh, and Y.H. Kim, editors, *Proceedings of the 5th International Conference and Workshop on Numerical Simulation of 3D Sheet Forming Processes, NUMISHEET 2002*, pages 515 – 524, Jeju Island, Korea, 2002.

[71] R.H. Wagoner and L. Geng. Role of plastic anisotropy and its evolution on springback. *International Journal of Mechanical Sciences*, 44(1):123–148, 2002.

[72] R. Hill. Constitutive modeling of orthotropic plasticity in sheet metals. *Journal of Mechanics and Physics of Solids*, 38:405–417, 1990.

[73] W.F. Hosford. A generalized isotropic yield criterion. *Journal of Applied Mechanics, Transactions of the ASME*, 39:607–609, 1972.

[74] F. Barlat, Y. Maeda, K. Chung, M. Yanagawa, J.C. Brem, Y. Hayashida, D.J. Lege, K. Matsui, S.J. Murtha, S. Hattori, R.C. Becker, and S. Makosey. Yield function development for aluminum alloy sheets. *Journal of Mechanics and Physics of Solids*, (45):1727–1763, 1997.

[75] H. Vegter, P. Drent, and J. Huétink. A planar anisotropic yield criterion based on mechanical testing at multi-axial stress states. In P.R. Shen and S.-F. Dawson, editors, *Proceedings of NUMIFORM 1995. Simulation of Materials Processing: Theory, Methods and Applications*, pages 345–350, Rotterdam, The Netherlands, 1995. Balkema.

[76] H. Vegter, Y. An, H.H. Pijlman, B.D. Carleer, and J. Huétink. Advanced material models in simulation of sheet metal forming processes and prediction of forming limits. In *Proceedings of the 1st ESAFORM Conference on Material Forming*, pages 499–502, 1998.

[77] A. Krasowsky, T. Walde, W. Schmitt, F. Andrieux, and H. Riedel. Springback simulation in sheet metal forming using material formulation based on combined isotropic-kinematic hardening with elasto-plastic anisotropy. In R. Kergen, L. Kebler, N. Langerak, F.-J. Lenze, E. Janssen, and G. Steinbeck, editors, *Proceedings of IDDRG 2004. Forming the Future. Global trends in sheet metal forming*, pages 104 – 113, Sindelfingen, Germany, 2004.

[78] S. Hiwatashi, A. Van Bael, P. Van Houtte, and C. Teodosiu. Modelling of plastic anisotropy based on texture and dislocation structure. *Computational Materials Science*, 9(1-2):274–284, 1997.

[79] M. Van Riel and A.H. van den Boogaard. Stress and strain responses for continuous orthogonal strain path changes with increasing sharpness. *Scripta Materialia*, 57:381 – 384, 2007.

[80] F. Yoshida and T. Uemori. A model of large-strain cyclic plasticity and its application to springback simulation. *International Journal of Mechanical Sciences*, 45(10):1687–1702, 2003.

[81] Z. Mroz. On generalized kinematic hardening rule with memory of maximum prestress. *Journal of applied mechanics*, pages 241 – 259, 1981.

[82] R.D. Krieg. A practical two surface plasticity theory. *Journal of applied mechanics*, pages 641 – 646, 1975.

[83] Y. Jiang and P. Kurath. Characteristics of the armstrong-frederick type plasticity models. *International Journal of Plasticity*, 12(3):387–415, 1996.

[84] L. Geng, S. Yao, and R.H. Wagoner. Anisotropic hardening equations derived from reverse-bend testing. *International Journal of Plasticity*, 18(5):743–767, 2002.

[85] M. Ristinmaa. Cyclic plasticity model using one yield surface only. *International Journal of Plasticity*, 11(2):163–181, 1995.

[86] J.L. Chaboche. Time-independent constitutive theories for cyclic plasticity. *International Journal of Plasticity*, 2(2):149 – 188, 1986.

[87] B.K. Chun, J.T. Jinn, and J.K. Lee. Modeling the bauschinger effect for sheet metals, part i: theory. *International Journal of Plasticity*, 18(5-6):571–595, 2002.

[88] B.K. Chun, H.Y. Kim, and J.K. Lee. Modeling the bauschinger effect for sheet metals, part ii: applications. *International Journal of Plasticity*, 18(5-6):597–616, 2002.

[89] J. Huétink, A.H. Streppel, and P.T. Vreede. Development and experimental verification of constitutive equations for anisotropic sheet metal. In D.R.J. Owen, E. Oñate, and E. Hinton, editors, *Computational Plasticity, Fundamentals and Applications*, volume 2, pages 2271–2282, 1995.

[90] F. Yoshida and T. Uemori. A model of large-strain cyclic plasticity describing the bauschinger effect and workhardening stagnation. *International Journal of Plasticity*, 18(5):661–686, 2002.

[91] C. Teodosiu and Z. Hu. Evolution of the intergranular microstructure at moderate and large strains: modelling and computational significance. In P.R. Shen and S.-F. Dawson, editors, *Proceedings of NUMIFORM 1995. Simulation of Materials Processing: Theory, Methods and Applications*, pages 173–182, Rotterdam, The Netherlands, 1995. Balkema.

[92] H. Haddadi, S. Bouvier, M. Banu, C. Maier, and C. Teodosiu. Towards an accurate description of the anisotropic behaviour of sheet metals under large plastic deformations: Modelling, numerical analysis and identification. *International Journal of Plasticity*, 22(12):2226, 2006.

[93] E.H. Atzema. *Formability of sheet metal and sandwich laminates*. PhD thesis, University of Twente, 1994.

[94] G. Kloosterman. *Contact methods in finite element simulations*. PhD thesis, University of Twente, 2002.

[95] P.T. Vreede, B.D. Carleer, M.F.M. Louwes, and J. Huétink. Finite-element simulation of sheet-forming processes with the help of contact elements on small-scale workstations. *Journal of Materials Processing Technology*, 50(1-4):264–276, 1995.

[96] G.Y. Li, M.J. Tan, and K.M. Liew. Springback analysis for sheet forming processes by explicit finite element method in conjunction with the orthogonal regression analysis. *International Journal of Solids and Structures*, 36(30), 1999.

[97] ABAQUS, Inc. *ABAQUS Theory Manual, version 6.5*, 2007.

[98] A. Muthler, A. Dster, W. Volk, M. Wagner, and E. Rank. High order finite elements applied to the computation of elastic spring back in sheet metal forming. In S. Ghosh, J.M. Castro, and J.K. Lee, editors, *Proceedings of NUMIFORM 2004. Materials Processing and Design: Modeling, Simulation and Applications*, pages 946 – 951, Columbus, Ohio, 2004.

[99] J.L. Alves and L.F. Menezes. Application of tri-linear and tri-quadratic 3-d solid elements in sheet metal forming process simulations. In Ken ichiro Mori, editor, *Proceedings of NUMIFORM 2001*, pages 639 – 644, Toyohashi, Japan, 2001.

[100] L.F. Menezes and C. Teodosiu. Three-dimensional numerical simulation of the deep-drawing process using solid finite elements. *Journal of Materials Processing Technology*, 97(1-3):100–106, 2000.

[101] C.Z. Xia. A parametric study of springback behavior. In Ken ichiro Mori, editor, *Proceedings of NUMIFORM 2001*, pages 711–716, Toyohashi, Japan, 2001.

[102] A.H. van den Boogaard. *Thermally enhanced forming of aluminium sheet*. PhD thesis, University of Twente, 2002.

[103] Z.C. Xia, S.C. Tang, and J.C. Carnes. Accurate springback prediction with mixed solid/shell elements. In J. Huétink and F.P.T. Baaijens, editors, *Proceedings of NUMIFORM 1998. Simulation of Material Processing: Theory, Methods and Applications*, pages 813 – 818, Enschede, The Netherlands, 1998.

[104] H. Lu, K. Ito, K. Kazama, and S. Namura. Development of a new quadratic shell element considering the normal stress in the thickness direction for simulating sheet metal forming. 171(3):341, 2006.

[105] R.J. Alves de Sousa, J.W. Yoon, R.P.R. Cardoso, R.A. Fontes Valente, and J.J. Gracio. On the use of a reduced enhanced solid-shell (ress) element for sheet forming simulations. *International Journal of Plasticity*, 23(3):490, 2007.

[106] Y. Hu. Quasi static finite element algorithms for sheet metal stamping springback simulation. In J.C. Gelin and P. Picart, editors, *Proceedings of the 4th International Conference and Workshop on Numerical Simulation of 3D Sheet Forming Processes, NUMISHEET 1999*, pages 71 – 76, Besancon, France, 1999.

[107] A.P. Karafillis and M.C. Boyce. Tooling and binder design for sheet metal forming processes compensating springback error. *International Journal of Machine Tools & Manufacture*, 36(4):503–526, 1996.

[108] L. Papeleux and J.-P. Ponthot. Finite element simulation of springback in sheet metal forming. *Journal of Materials Processing Technology*, 125-126:785–791, 2002.

[109] D. Joannic and J.C. Gelin. Shape defects in sheet metal forming operations after springback. In J.C. Gelin and P. Picart, editors, *Proceedings of the 4th International Conference and Workshop on Numerical Simulation of 3D Sheet Forming Processes, NUMISHEET 1999*, pages 29 – 34, Besancon, France, 1999.

[110] D.Y. Yang, D.W. Jung, I.S. Song, D.J. Yoo, and J.H. Lee. Comparative investigation into implicit, explicit, and iterative implicit/explicit schemes for the simulation of sheet-metal forming processes. *Journal of Materials Processing Technology*, 50(1-4):39–53, 1995.

[111] A.H. van den Boogaard, T. Meinders, and J. Huétink. Efficient implicit finite element analysis of sheet forming processes. *International Journal for Numerical Methods in Engineering*, 56(8):1083–1107, 2003.

[112] T. Belytschko, W.K. Liu, and B. Moran. *Nonlinear Finite Elements for Continua and Structures*. John Wiley and Sons, Ltd., 2000.

[113] D.W. Jung. Static-explicit finite element method and its application to drawbead process with spring-back. *Journal of Materials Processing Technology*, 128(1-3):292–301, 2002.

[114] M.C. Oliveira, J.L. Alves, and L.F. Menezes. Springback evaluation using 3-d finite elements. In D.-Y. Yang, S.I. Oh, H. Huh, and Y.H. Kim, editors, *Proceedings of the 5th International Conference and Workshop on Numerical Simulation of 3D Sheet Forming Processes, NUMISHEET 2002*, pages 189 – 194, Jeju Island, Korea, 2002.

[115] M.J. Finn, P.C. Galbraith, L. Wu, J.O. Hallquist, L. Lum, and T.-L. Lin. Use of a coupled explicit–implicit solver for calculating spring-back in automotive body panels. *Journal of Materials Processing Technology*, 50(1-4):395–409, 1995.

[116] S.W. Lee and D.Y. Yang. An assessment of numerical parameters influencing springback in explicit finite element analysis of sheet metal forming process. *Journal of Materials Processing Technology*, 80-81:60–67, 1998.

[117] N. Narasimhan and M. Lovell. Predicting springback in sheet metal forming: An explicit to implicit sequential solution procedure. *Finite Elements in Analysis and Design*, 33(1):29–42, 1999.

[118] D.W. Jung and D.Y. Yang. Step-wise combined implicit-explicit finite-element simulation of autobody stamping processes. *Journal of Materials Processing Technology*, 83(1-3):245–260, 1998.

[119] L. Noels, L. Stainier, and J.-P. Ponthot. Combined implicit/explicit time-integration algorithms for the numerical simulation of sheet metal forming. *Journal of Computational and Applied Mathematics*, 168(1-2):331–339, 2004.

[120] K. E. Atkinson. *An introduction to numerical analysis*. John Wiley and Sons, Inc., 1989.

[121] R.D. Cook, D.S. Malkus, M.E. Plesha, and R.J. Witt. *Concepts and Applications of Finite Element Analysis*. John Wiley and Sons, Inc., 4th edition, 2002.

[122] O. Schenk and K. Gartner. Solving unsymmetric sparse systems of linear equations with pardiso. *Future Generation Computer Systems*, 20(3):475–487, 2004.

[123] T. Meinders, B.D. Carleer, H.J.M. Geijselaers, and J. Huétink. Implementation of an equivalent drawbead model in a finite-element code for sheet metal forming. *Journal of Materials Processing Technology*, 83(1-3):234, 1998.

[124] X. Li, Y. Yang, Y. Wang, J. Bao, and S. Li. Effect of the material-hardening mode on the springback simulation accuracy of v-free bending. *Journal of Materials Processing Technology*, 123(2):209–211, 2002.

[125] N. Montmayeur and C. Staub. Springback prediction with optris. In J.C. Gelin and P. Picart, editors, *Proceedings of the 4th International Conference and Workshop on Numerical Simulation of 3D Sheet Forming Processes, NUMISHEET 1999*, pages 41 – 46, Besancon, France, 1999.

[126] T. Meinders. *Plate and shell theory.* University of Twente, 2004.

[127] J.L. Batoz, K.J. Bathe, and L.W. Ho. A study of three-node triangular plate bending elements. *International Journal for Numerical Methods in Engineering*, 15:1771–1812, 1980.

[128] A. Makinouchi, E. Nakamachi, E. Oñate, and R.H. Wagoner, editors. *Proceedings of the 2th international conference and workshop on numerical simulation of 3D sheet metal forming processes, NUMISHEET 1993*, Isehara, Japan, 1993.

[129] H. Shim and E. Suh. Contact treatment algorithm for the trimmed nurbs surface. *Journal of Materials Processing Technology*, 104(3):200–206, 2000.

[130] A. Santos and A. Makinouchi. Contact strategies to deal with different tool descriptions in static explicit fem for 3-d sheet-metal forming simulation. *Journal of Materials Processing Technology*, 50(1-4):277–291, 1995.

[131] MSC Software Corporation. *MSC.Marc User's Guide*, 2007.

[132] T. Hama, C. Teodosiu, A. Makinouchi, H. Fujimoto, and H. Takuda. Springback simulation of high strength steel sheet using local interpolation for tool surfaces. In J.M.A. César de Sá and A.D. Santos, editors, *Proceedings of the 9th International Conference on Numerical Methods in Industrial Forming Processes, NUMIFORM 2007*, pages 805–810, Porto, Portugal, 2007.

[133] R.H. Wagoner and M. Li. Simulation of springback: Through-thickness integration. *International Journal of Plasticity*, 23(3):345–360, 2007.

[134] W.-R. Harn and T. Belytschko. Adaptive multi-point quadrature for elastic-plastic shell elements. *Finite Elements in Analysis and Design*, 30(4):253–278, 1998.

[135] S. Rajendran and K.M. Liew. Optimal stress sampling points of plane triangular elements for patch recovery of nodal stresses. *International Journal for Numerical Methods in Engineering*, 58(4):579–607, 2003.

[136] C.J. Burgoyne and M.A. Crisfield. Numerical integration strategy for plates and shells. *International Journal for Numerical Methods in Engineering*, 29(1):105–121, 1990.

[137] J.C. Simo and J.G. Kennedy. On a stress resultant geometrically exact shell model. part v. nonlinear plasticity: formulation and integration algorithms. *Computer Methods in Applied Mechanics and Engineering*, 96(2):133–171, 1992.

[138] P.J. Davis and P. Rabinowitz. *Methods of numerical integration*. Academic Press, Inc., 2nd edition, 1985.

[139] G.H. Golub and Welsch J.H. *Calculation of Gauss quadrature rules*, november 1967.

[140] G.H. Golub. *Some modified egenvalue problems*, august 1971.

[141] R.H. Wagoner and M. Li. Advances in springback. In L.M. Smith, F. Pourboghrat, J.W. Yoon, and T.B. Stoughton, editors, *Proceedings of the 6th international conference and workshop on numerical simulation of 3D sheet metal forming processes, NUMISHEET 2005*, volume Part A, pages 209–214, Detroit, MI, U.S.A., 2005.

[142] I.A. Burchitz, T. Meinders, and J. Huétink. Adaptive through-thickness integration strategy for shell elements. In J.M.A. César de Sá and A.D. Santos, editors, *Proceedings of the 9th International Conference on Numerical Methods in Industrial Forming Processes, NUMIFORM 2007*, pages 699–704, Porto, Portugal, 2007.

[143] I.A. Burchitz and T. Meinders. Adaptive through-thickness integration for accurate springback prediction. *International Journal for Numerical Methods in Engineering*, 2007. DOI: 10.1002/nme.2260.

[144] R.J. Rice. A metalgorithm for adaptive quadrature. *Journal of the ACM (JACM)*, 22(1):61–82, 1975.

[145] W. Gander and W. Gautschi. Adaptive quadrature - revisited. *BIT Numerical Mathematics*, 40(1):84–101, 2000.

[146] T.O. Espelid. Doubly adaptive quadrature routines based on newton-cotes rules. *BIT Numerical Mathematics*, 43(2):319–337, 2003.

[147] H. Armen, A. Pifko, and H.S. Levine. Finite element analysis of structures in the plastic range. Report NASA CR-1649, Grumman Aerospace Corporation, 1971.

[148] M. Avetisyan. *Numerical Trimming Operation with Respect to Springback*. Netherlands Institute for Metals Research, 2004.

[149] M. Ortiz and J.J. Quigley. Adaptive mesh refinement in strain localization problems. *Computer Methods in Applied Mechanics and Engineering*, 90(1-3):781, 1991.

[150] T. Sheppard and J.M. Roberts. Stress/strain relationships for strip-shape correction process. *Journal of the institute of metals*, 99:223 – 228, 1971.

[151] J.M. Roberts and T. Sheppard. On the mechanics of the tension-levelling process. *Journal of the institute of metals*, 99:293 – 301, 1971.

[152] R. de Borst and P.H. Feenstra. Studies in anisotropic plasticity with reference to the hill criterion. *International Journal for Numerical Methods in Engineering*, 29:315 – 336, 1990.

[153] W.H. Press, S.A. Teukolsky, W.T. Vetterling, and B.P. Flannery. *Numerical Recipes in Fortran 90*. Press Syndicate of the University of Cambridge, 2nd edition, 1996.

[154] J.L. Batoz and Lardeur P. A discrete shear triangular nine d.o.f. element for the analysis of thick to very thin plates. *International Journal for Numerical Methods in Engineering*, 28:533–560, 1989.